

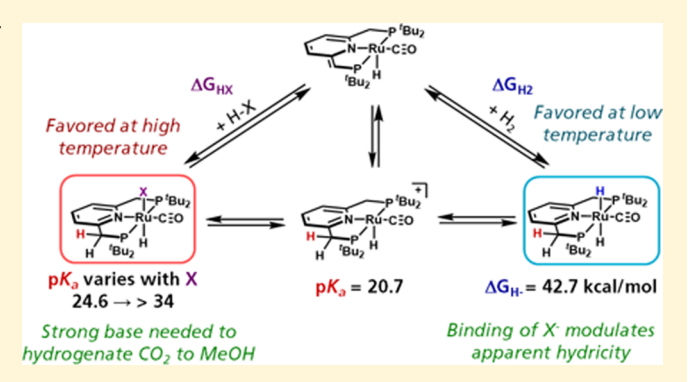
Thermodynamic Analysis of Metal—Ligand Cooperativity of PNP Ru Complexes: Implications for CO₂ Hydrogenation to Methanol and **Catalyst Inhibition**

Cheryl L. Mathis, Jackson Geary, Yotam Ardon, Maxwell S. Reese, Mallory A. Philliber, Ryan T. VanderLinden, and Caroline T. Saouma*

Department of Chemistry, University of Utah, 315 S. 1400 E., Salt Lake City, Utah 84112, United States

Supporting Information

ABSTRACT: The hydrogenation of CO₂ in the presence of amines to formate, formamides, and methanol (MeOH) is a promising approach to streamlining carbon capture and recycling. To achieve this, understanding how catalyst design impacts selectivity and performance is critical. Herein we describe a thorough thermochemical analysis of the (de)hydrogenation catalyst, (PNP)Ru-Cl (PNP = 2,6-bis(di-tertbutylphosphinomethyl)pyridine; Ru = Ru(CO)(H) and correlate our findings to catalyst performance. Although this catalyst is known to hydrogenate CO2 to formate with a mild base, we show that MeOH is produced when using a strong base. Consistent with pK_a measurements, the requirement for a strong base suggests that the deprotonation of a six-



coordinate Ru species is integral to the catalytic cycle that produces MeOH. Our studies also indicate that the concentration of MeOH produced is independent of catalyst concentration, consistent with a deactivation pathway that is dependent on methanol concentration, not equivalency. Our temperature-dependent equilibrium studies of the dearomatized congener, (*PNP)Ru, with various H-X species (to give (PNP)Ru-X; X = H, OH, OMe, OCHO, OC(O)NMe₂) reveal that formic acid equilibrium is approximately temperature-independent; relative to H₂, it is more favored at elevated temperatures. We also measure the hydricity of (PNP)Ru-H in THF and show how subsequent coordination of the substrate can impact the apparent hydricity. The implications of this work are broadly applicable to hydrogenation and dehydrogenation catalysis and, in particular, to those that can undergo metal-ligand cooperativity (MLC) at the catalyst. These results serve to benchmark future studies by allowing comparisons to be made among catalysts and will positively impact rational catalyst design.

INTRODUCTION

Rising atmospheric carbon dioxide levels present a significant incentive to develop new catalysts that are active for the transformation of CO2 into renewable fuels. Catalysts that engage in metal-ligand cooperativity (MLC)¹ are particularly attractive because of their proven ability to hydrogenate CO2 to formate; 2-4 in the presence of amines, formamides 5,6 and MeOH are also produced. 7,8 Formic acid and MeOH are both attractive to probe as hydrogen storage mediums. 9 However, existing studies often employ high pressures/temperatures, strong bases, and precious metals to promote reactivity. A thermochemical understanding of existing systems will help guide the rational design of next-generation catalysts; factors such as the p K_a of the ligand, K_{eq} with substrates, and ΔG_{H^-} can modulate catalyst performance.

The strategy of MLC is illustrated in Figure 1, which considers the hydrogenation of CO₂ to formate with Milstein's PNN-ligated Ru catalyst. ^{2a} In this mechanism, H₂ is heterolytically cleaved with ligand protonation concomitant to hydride installation on Ru. Although this mechanism has been proposed by Sanford, 2a the direct pathway is suggested by Pidko in the analogous PNP-ligated Ru system (Figure 1, right pathway).2c Their calculations suggest that deprotonation of the bound H2 in a cationic Ru-H2 species occurs with the added base and an outer-sphere formate. Their analysis moreover suggests that the species with formate bound to the Ru is an off-cycle species, contrary to the MLC pathway. These cycles illustrate how hydricity, pK_a , and the propensity to react with H2 over other H-X species must be balanced. Related computational studies suggest that the direct pathway may be more favorable than those that undergo MLC with both Ru and Ir catalysts, ^{2c,10} but the calculations do not always take into account the reaction conditions. These discrepancies reinforce the need to experimentally establish the thermodynamic parameters of such systems to determine their impact on catalysis.

Received: June 26, 2019 Published: August 8, 2019 Journal of the American Chemical Society

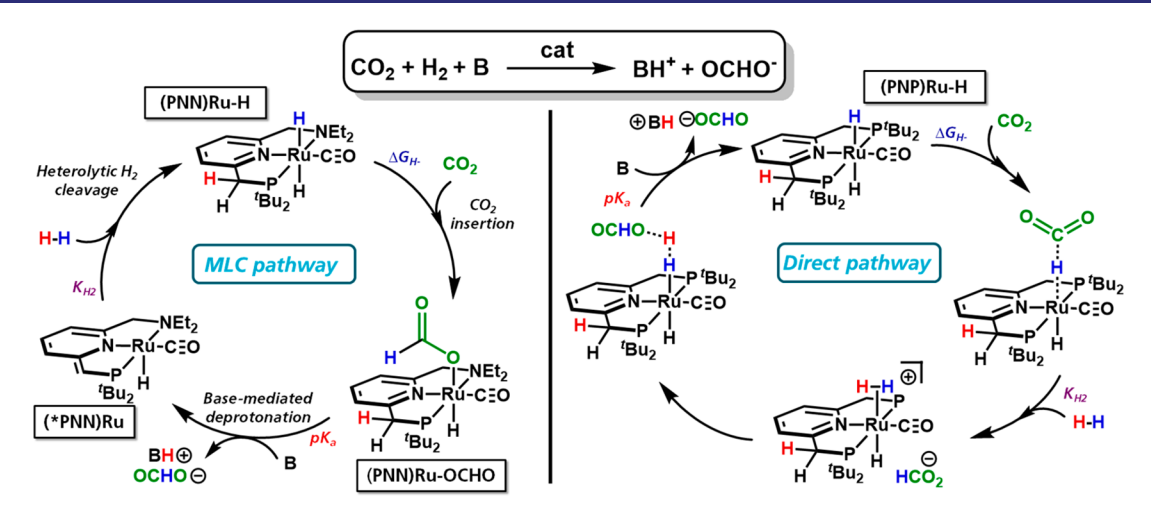


Figure 1. Mechanistic proposals for the hydrogenation of CO₂ to formate. All Ru species are L₄X₂ and 18e⁻. Pertinent thermochemical parameters are given outside the reaction arrows. (Left) MLC mechanism whereby H2 addition occurs to the dearomatized (*PNN)Ru. (Right) The direct pathway does not undergo ligand deprotonation.

For the successful hydrogenation of CO₂ to MeOH, ¹¹ only catalysts that can or are speculated to undergo MLC facilitate this transformation in the presence of amines.^{7,8} This is pertinent to carbon capture and recycling schemes because current technologies rely on amines to capture CO2, giving carbamates and carbonates. 12 However, these systems are limited by the energy demands required for CO₂ release.¹³ Thus, the hydrogenation of CO₂ in the presence of amines would streamline carbon capture and recycling.

The hydrogenation of carbamates ("captured CO₂") is thought to occur via thermal release of CO_2 , which is first hydrogenated to formate (Scheme 1, (i)). 7b,14 Condensation

Scheme 1. Hydrogenation of (DMA-H)(DMC) to MeOH Mediated by Aliphatic (PhPHNP)Ru-(HBH3) That Can Undergo MLC'

^aHydrogenation is thought to proceed via the species shown, with the hydrogenation steps labelled (i) and (ii).

with an amine then provides formamide, which is further hydrogenated to MeOH (Scheme 1, (ii)). Not all catalysts that hydrogenate CO2 to formate can hydrogenate formic acid to MeOH (in the presence of amines), ^{7d} and generally harsher conditions are required for the latter. ^{5,8b} Sometimes, the CO₂ must first be removed, and hence the overall transformation is necessarily sequential. 8b For Ru, it is speculated that only the hydrogenation of formamide to MeOH occurs via MLC (Scheme 1, (ii)), 14 whereas with Mn both steps are thought to proceed via MLC.8b Establishing the mechanism for both hydrogenations as well as the thermodynamic parameters of catalysts that can and cannot bring about this transformation is warranted to advance catalyst development.

Toward advancing catalysts that transfer net H2, several systems that undergo MLC have been developed. 1c Comparisons of catalyst performance often are based on turnover numbers (TON), turnover frequencies (TOF), and/or reaction times. 1c With no further mechanistic studies, these parameters do not reveal the underlying reason(s) as to why the catalysts perform differently, nor do they correlate these effects with thermochemical parameters, limiting rational catalyst design.

Recently, Prakash and co-workers investigated the role of the ligand and amine additive for the hydrogenation of CO2 to MeOH.¹⁴ They found a correlation between how electrondonating the pincer ligand is to the catalyst performance and through elegant mechanistic studies established that this is due to the relative stability of an off-cycle species.

Because the catalyst is implicated in each step of the mechanism, it is important to know the thermodynamic parameters associated with the catalyst. Hydricity, basicity, and ease of cleaving an H-X bond (Figure 1) are likely sensitive to modification of the catalyst. This approach has been applied to electrocatalytic H₂ evolution¹⁵ and CO₂ reduction.¹⁶ Expanding this knowledge to hydrogenations, 17 particularly those that undergo MLC, will help develop catalysts whereby each step is approximately energetically thermoneutral, avoiding highly exothermic and subsequent endothermic steps. It will also shed light on potential inhibition pathways, which may clarify the correlation of catalyst loading and TON. The results will be broadly applicable to systems that transfer H₂.

Herein we provide a thorough thermochemical analysis of the Ru PNP system. This catalyst is chosen for these studies because it can perform several dehydrogenations 18 and hydrogenations 19 including that of CO₂ to formate, 2c,d,20 and in the presence of amines, MeOH (vide infra). The analysis presented provides the first hydricity measurements in THF and the first hydricity measurements for complexes that react via MLC.²¹ This work also considers how the coordination of a sixth ligand impacts the apparent hydricity and pK_a of the catalyst and participation in likely thermodynamic bottlenecks during catalysis. Finally, the thermodynamic values are correlated to the catalytic results. Overall, this study benchmarks the thermodynamic parameters for (de)hydrogenation catalysts that operate via MLC. This allows for future

comparisons to be made, impacting our understanding of catalyst limitations.

RESULTS

Overview of the System Considered. The (PNP)Ru species pertinent to this study are shown in Figure 2 (PNP =

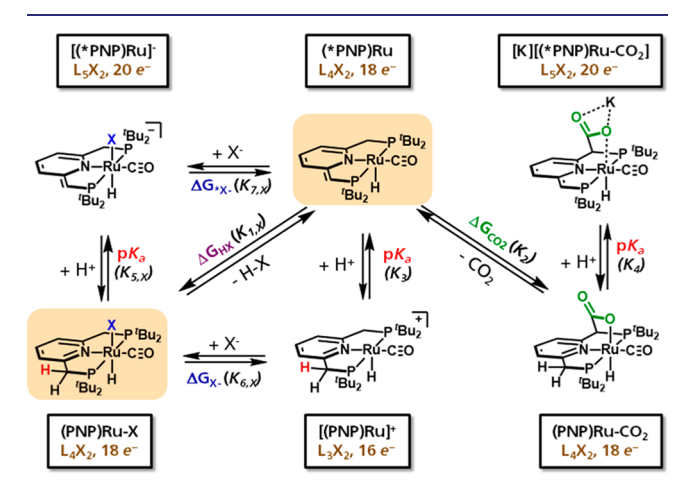


Figure 2. Thermodynamic parameters considered in this study. Species in gold boxes are proposed to be pertinent to catalysis via MLC (Figure 1). Equilibrium constants are shown above the arrow that corresponds to the direction of *K*. For clarity, only balanced equations are shown for the reverse equilibria. Because all of the congeners feature a hydride and a CO ligand that remain unchanged, we do not include these ligands in the shorthand nomenclature (boxed) and simply give the identity of the X-type ligand that occupies the sixth coordination site. Deprotonation of the PNP ligand at one of the methylene positions gives the dearomatized species (indicated by *), whereby the pyridine L-type donor becomes an anionic LX-type donor. The formal ligand type and electron count are provided in the boxes for clarity.

2,6-bis(di-tert-butylphosphinomethyl)pyridine). Central to all equilibria is the five-coordinate dearomatized species, (*PNP)Ru (Figure 2, middle top). This species reacts with Brønsted acid H–X species to give (PNP)Ru–X ($K_{1,X}$); in this reaction, proton transfer to the ligand is coupled to the nucleophilic attack of X^- on Ru (Figure 2, bottom left). These equilibria are pertinent because they are competitive with the addition of H_2 or other species to (*PNP)Ru in the catalytic cycle (Figure 1).

The cationic L_3X_2 16-electron species, $[(PNP)Ru]^+$, 22 is the protonated congener of (*PNP)Ru and is related to (PNP)Ru-X by the loss of the anionic X-type ligand (Figure 2, bottom). Thus, it is the product of hydride transfer to a substrate. These three congeners are readily accessible synthetically, and when X = H, together they are used to establish the hydricity of (PNP)Ru-H (Figure 2, bottom left).

Deprotonation of (PNP)Ru–X gives $[(*PNP)Ru-X]^-$, a formally L_5X_2 20-electron species. With a few exceptions, ^{2a,22,23} species of the type $[(*PNP)Ru-X]^-$ are not stable and lose X^- , ^{1c} yielding (*PNP)Ru. For example, the treatment of (PNP)Ru-Cl with 1 equiv of ^tBuOK gives dearomatized (*PNP)Ru.

Dearomatized (*PNP)Ru also reacts with Lewis acids²³ such as CO₂ to give (PNP)Ru-CO₂,²⁴ whereby the basic site on the ligand attacks the Lewis acid carbon of CO₂ (Figure 2, bottom right). This species is speculated to be detrimental to

the hydrogenation of CO_2 .^{2a,d} The adduct can also be deprotonated to give $[K][(*PNP)Ru-CO_2]$ (vide infra).

Synthesis and Characterization of Complexes. Toward measuring the equilibria shown in Figure 2, several pertinent congeners needed to be prepared. The addition of H_2 , Brønsted acid H-X, or Lewis acid CO_2 to (*PNP)Ru readily gives (PNP)Ru-X (Figure 2), as described in the literature (X = H, OMe, OCHO, OH). 2d,5,24 It should be noted that in the presence of Lewis or Brønsted acids, (*PNP)Ru is in equilibrium with (PNP)Ru-X, where the equilibrium constant depends on the identity of H-X and, in some instances, the concentration (vide infra). Thus, the various proton sources that may be produced during catalysis are in competition with H_2 to coordinate the metal (i.e., competing $K_{1,X}$) during catalysis.

To probe the initial Ru species formed in the catalytic hydrogenation of amine "captured" CO₂, 5,7,14,25 we sought to prepare a carbamate species. The addition of excess of dimethylammonium dimethylcarbamate, (DMA–H)(DMC), to dearomatized (*PNP)Ru cleanly generates (PNP)Ru–DMC. This carbamate was chosen because (DMA–H)(DMC) has been shown to be hydrogenated to MeOH using (PhPHNP)Ru–(HBH₃) as a catalyst (Scheme 1). The identity of (PNP)Ru–DMC as a six-coordinate aromatized species was confirmed by NMR spectroscopy and XRD (Figure 3). Similar to other carboxylate bound species such

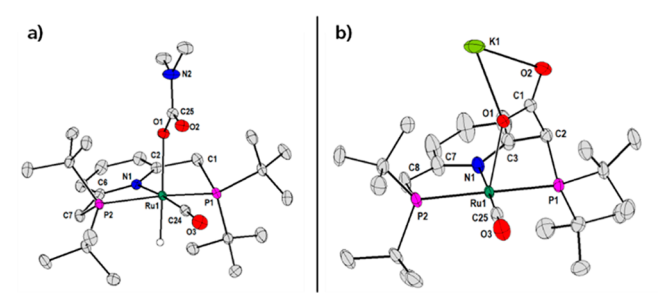


Figure 3. Solid-state structures (50% displacement ellipsoids) of (a) (PNP)Ru-DMC and (b) [K][(*PNP)Ru-CO₂]. All calculated hydrogen atoms and minor components of disorder are omitted for clarity. Only one-half of the dimeric unit of [K][(*PNP)Ru-CO₂] is shown. Select bond distances (Å) for (PNP)Ru-DMC: Ru1-N1, 2.145(1); Ru1-O1, 2.205(1); C1-C2, 1.503(2); C6-C7, 1.495(2). Select bond distances (Å) for [K][(*PNP)Ru-CO₂]: Ru1-N1, 2.119(3); Ru1-O1, 2.331(3); C1-O1, 1.269(5); C1-O2, 1.244(5); C1-C2, 1.552(6); C2-C3, 1.510(6); C7-C8, 1.374(6). Analogous bonds in the other half of the dimer have similar bond distances.

as (PNP)Ru–OCHO^{2d} and (PNP)Ru–CO₂, ²⁴ the hydride resonance appears as a triplet centered at $\delta = -16.74$ ppm ($J_{PH} = 19$ Hz) in the ¹H NMR spectrum (d_8 -THF). Though the carbamate species (PNP)Ru–DMC is in equilibrium with (*PNP)Ru (vide infra), it is stable to vacuum. This is also true for the other carboxylate species, (PNP)Ru–OCHO and (PNP)Ru–CO₂, but contrasts with the instability of (PNP)-Ru–H, (PNP)Ru–OH, and (PNP)Ru–OMe, all of which revert to dearomatized (*PNP)Ru upon concentration in vacuo at ambient temperature; ²⁶ this instability limits our ability to readily isolate these species in the absence of H–X in solution.

To gain insight into the true pK_a of six-coordinate (PNP)Ru-X, we sought to deprotonate (PNP)Ru-CO₂, the rationale being that the Ru-O bond will be weakened or if

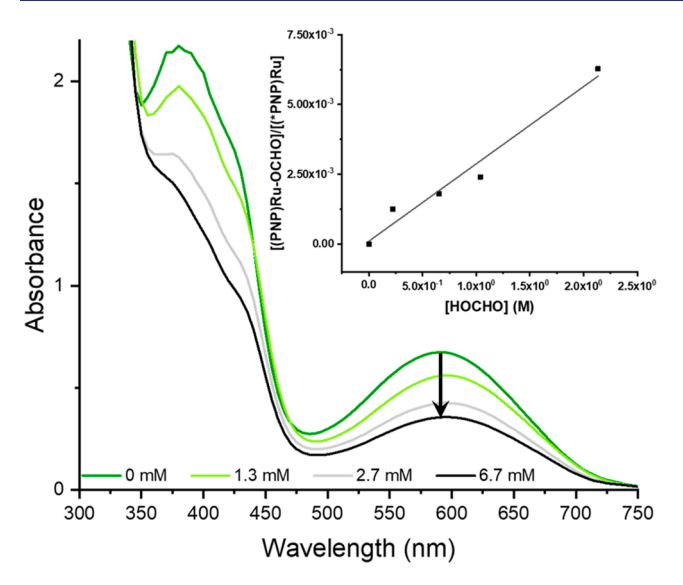


Figure 4. Stacked UV-vis spectra for the equilibria of (*PNP)Ru (0.60 mM) and formic acid in THF. Concentrations of formic acid given in the legend are those at equilibrium. (Inset) Plot of $\frac{[(PNP)Ru-OCHO]}{[(PNP)Ru-OCHO]}$ vs [H-OCHO]. The slope gives $K_{1,OCHO}$ (eq 1).

cleaved will remain formally associated with the Ru (Figure 2). 2a This is in contrast to the other (PNP)Ru-X species which lose X⁻ and therefore have a ΔG_{*X} - contribution (Figure 2, top left to top middle). Indeed, the reaction of a d_8 -THF solution of (PNP)Ru-CO2 with 1 equiv of KHMDS (KHMDS = potassium hexamethyldisilazide) cleanly gives [K][(*PNP)Ru-CO₂]. The NMR spectral parameters for this species are similar to that of [(*PNN)Ru-CO₂]⁻, which was characterized by Sanford and co-workers.^{2a} (See Figure 1 for PNN structure and SI for NMR characterization.)

To determine if the CO₂ oxygen remained bound to Ru, crystals of [K][(*PNP)Ru-CO₂] were grown by vapor diffusion of diethyl ether into THF, and the solid-state structure is shown in Figure 3. In the solid state, [K][(*PNP)-Ru-CO₂ is a dimeric species bridged by a K₂O₂ diamond core (SI). The loss of aromaticity is evident from the C7-C8 bond distance of 1.374(6) Å. By contrast, C2-C3 is 1.510(6) Å, which is similar to that found in the neutral analogue (1.507(2) Å).²⁴ Upon deprotonation, the N1-Ru1 bond distance remains unchanged (Figure 3 caption). This contrasts with deprotonation of the related aliphatic PNP ligands (Scheme 1), whereby the amide-Ru bond distance is noticeably shorter (~0.18 Å) than the amine-Ru bond ⁷ Notably, CO₂ still coordinates to Ru with a distance.2 Ru1-O1 bond distance of 2.331(3) Å. This represents an ~0.05 Å elongation from neutral (PNP)Ru- CO_2^{24} and an ~0.07-0.1 Å elongation from other structurally characterized carboxylate and carbonate derivatives.2d The observed elongation is consistent with the Ru center now being formally 20-electron.

Equilibria with H-X Species. Dearomatized (*PNP)Ru readily reacts with Brønsted and Lewis acids to give (PNP)Ru-X (Figure 2, $K_{1,X}$ and K_2 , respectively). However, given the importance of its reaction with H2 for hydrogenation reactions and the potential inhibitory effect of this reaction with other species that may be present during catalysis, we sought to establish the equilibrium constants with H₂, H-X $(K_{1,X})$, and CO_2 (K_2) . Our interest in the hydrogenation of CO₂ prompted an analysis of the following H-X species that

may be present during catalysis: MeOH, H2O, HC(O)OH, DMF, diethylamine, and [DMA-H][DMC]. Neither DMF nor diethylamine reacts with (*PNP)Ru to an observable extent (Figures S39 and S35, respectively); all other species react with (*PNP)Ru to give (PNP)Ru-X. The equilibrium is readily monitored by UV-vis spectroscopy by observing the absorbance at 595 nm, which corresponds to dearomatized (*PNP)Ru (Figure 4). Briefly, the addition of various concentrations of H-X to a THF solution of (*PNP)Ru allows for the equilibrium constant (eq 1) to be established.

$$(K_{1,X}) = \frac{[(\mathbf{PNP})\mathbf{Ru} - \mathbf{X}]}{[(^*\mathbf{PNP})\mathbf{Ru}][\mathbf{H} - \mathbf{X}]}$$
(1)

Equation 1 represents the binding of H-X to Ru, and the stoichiometry suggests that there should be a concentration dependence for the equilibrium constant. This is confirmed by diluting equilibrium samples and noting the shift in the ratio of the two Ru species (see SI). Apart from (DMA-H)(DMC) (eqs 2 and 3), this concentration dependence was observed for all H-X species.

$$K_{\text{I,DMC}} = \frac{[(\mathbf{PNP})\mathbf{Ru} - \mathbf{DMC}][\mathbf{DMA}]}{[(^*\mathbf{PNP})\mathbf{Ru}][(\mathbf{DMA} - \mathbf{H})(\mathbf{DMC})]}$$
(3)

The lack of concentration dependence for the equilibrium with (DMA-H)(DMC) is rationalized on the basis that 1 equiv of DMA is formed and the (DMA-H)(DMC) substrate is strongly ion paired in solution.

Similarly, the equilibrium constant for the binding of H₂ and CO₂ is measured analogously (eqs 4 and 5, respectively), with the gas pressures given in atm. These measurements necessitate a knowledge of the equilibrium partial pressure due to the gas and hence require a large headspace such that minimal changes occur during equilibration. (See the SI for details.) At pressures that we can accurately measure, no (*PNP)Ru is observed at room temperature for the equilibria with H₂ or CO₂; the equilibrium constants are therefore extrapolated from higher-temperature data (vide infra).

$$(K_{1,H}) = \frac{[(\mathbf{PNP})\mathbf{Ru} - \mathbf{H}]}{[(\mathbf{PNP})\mathbf{Ru}]p\mathbf{H}_2}$$
(4)

$$(K_2) = \frac{[(\mathbf{PNP})\mathbf{Ru} - \mathbf{CO}_2]}{[(^*\mathbf{PNP})\mathbf{Ru}]pCO_2}$$
(5)

From the equilibrium constants, the free-energy changes can be obtained. The equilibria that are concentration-dependent will also have a concentration-dependent free energy (eqs 6; standard conditions are 1 M and 1 atm).

$$\Delta G_{1,X} = -RT \ln \left(\frac{[(\mathbf{PNP})\mathbf{Ru} - \mathbf{X}]}{[(^*\mathbf{PNP})\mathbf{Ru}][\mathbf{H} - \mathbf{X}]^o} [\mathbf{H} - \mathbf{X}] \right)$$
$$= \Delta G_{1,X}^o - RT \ln([\mathbf{H} - \mathbf{X}])$$
(6a)

Table 1. Equilibrium Constants and Free-Energy Change Associated with the Coordination of H-X and CO2 to (*PNP)Ru

					$K_{1,X}$	
H-X	$\Delta G_{1,X}^{\mathrm{o}} \left(\mathrm{kcal \cdot mol}^{-1} \right)$	$\Delta H_{1,X}^{o}$ (kcal·mol ⁻¹)	$\Delta S_{1,X}^{o} (cal \cdot mol^{-1} \cdot K^{-1})$	293 K (1 atm, 1 M)	428 K (1 atm, 1 M)	428 K (50 bar, 1 mM)
Н–Н	-4.1 ± 0.2^{h}	-17.4 ± 0.2	-45 ± 0.5	$1100 \pm 1.4^{a,d,g}$	$0.13^{a,d}$	$6.6^{a,d}$
(DMA-H)(DMC)	$-0.03 \pm 2^{f,h}$	-12.6 ± 1.5^f	-42 ± 5^{f}	1.3 ± 0.2	N.A. ^e	N.A. ^e
Н-ОСНО	-3.5 ± 0.2^{h}	0.06 ± 0.15	12 ± 0.5	355 ± 38^{b}	$370^{b,d}$	$0.37^{b,d}$
H-OMe	-2.0 ± 1.9^{h}	-3.5 ± 1.3	-5.2 ± 4.6	25 ± 5^{b}	$4.6^{b,d}$	$4.6 \times 10^{-3b,d}$
H-OH	-2.0 ± 0.6^{h}	-0.6 ± 0.4	8.7 ± 1.4	5.4 ± 0.5^{b}	$41^{b,d}$	$4.1 \times 10^{-2b,d}$
CO ₂ ^c	$-3.8 \pm 0.8^{c,h}$	-13.5 ± 0.6^{c}	-33 ± 2^{c}	$633 \pm 4^{a,c,d,g}$	$0.55^{a,c,d}$	$27.6^{a,c,d}$

"atm⁻¹. $^bM^{-1}$. c Equilibrium with CO₂ corresponds to K_2 . d Extrapolated from temperature-dependent data. e Not applicable because of the limited stability of DMC–H and (DMA–H)(DMC) at elevated temperatures. See the text for details. f Energies obtained from a limited temperature range (20–50 °C). g Error from propagation of the error of ΔG° , $\sigma_K = \exp(\sigma_{\Delta G}/RT)$. h Error from propagation of the error of ΔH° and ΔS° , $\sigma_{\Delta G} = \sqrt{(\sigma_{\Delta H})^2 + (|T|\sigma_{\Delta S})^2}$. Errors in the entropy and enthalpy are from errors in the intercept and slope, respectively.

$$\Delta G_{1,H} = -RT \ln \left(\frac{[(\mathbf{PNP})\mathbf{Ru} - \mathbf{H}]}{[(*\mathbf{PNP})\mathbf{Ru}]p^{\circ}\mathbf{H}_{2}} p\mathbf{H}_{2} \right)$$

$$= \Delta G_{1,H}^{\circ} - RT \ln(p\mathbf{H}_{2})$$
(6b)

The free energy for the equilibrium with CO_2 is analogous to that for H_2 given in eq 6b. Thus, under nonstandard states, the equilibrium constant is given by eq 7.

$$K_{1,X} = [H - X] \exp\left(\frac{-\Delta G_{1,X}^{\circ}}{RT}\right)$$
(7)

From eqs 6 and 7, increasing the concentration of H-X at equilibrium will favor the formation of (PNP)Ru-X. Equilibrium constants and equilibrium energies are given in Table 1.

The data in Table 1 indicate that under standard conditions the reaction of (*PNP)Ru with H₂ is most favorable, followed by that with CO₂ and formic acid; those with (DMA–H)(DMC) and H₂O are least favored. These findings are consistent with the notion that if (PNP)Ru–CO₂ is an off-cycle species, it can form competitively. Upon dilution, the equilibrium constants decrease accordingly for all H–X, with the exception of (DMA–H)(DMC). To our knowledge, only one other report considers equilibria with a dearomatized Ru species. The study considered the reaction of various Lewis acids in the related PNN system, all of which bind akin to CO₂. Although different equilibrium constants were obtained, the concentration dependence is not provided.

The free energy associated with the addition of H_2 is similar to that observed by others, whereby H_2 adds to give a metal dihydride.²⁹ It is smaller by \sim 2 kcal/mol than that found for a series of $(P_2N_2)Ni$ species,³⁰ whereby H_2 is heterolytically cleaved, protonating the ligand with hydride attack at the Ni.

Given that catalysis ensues at elevated temperatures, the temperature dependence of the equilibria was also determined. An overlay of the van't Hoff plots is shown in Figure 5, and the enthalpy and entropy are given in Table 1. During these studies, we found that (PNP)Ru-OMe and (PNP)Ru-OH are not stable at elevated temperatures, and hence a shifted temperature range was employed (Figures S30 and S31).

We also note that upon heating (PNP)Ru-DMC in the absence of DMA or (DMA-H)(DMC), some (PNP)Ru-CO₂ forms that remains present upon cooling (Figures S44 and S45). This indicates that free (DMC-H) is prone to release CO₂, complicating equilibrium measurements at elevated temperatures (SI). Indeed, the van't Hoff plot shown in Figure 5 shows a digression from linearity at 60

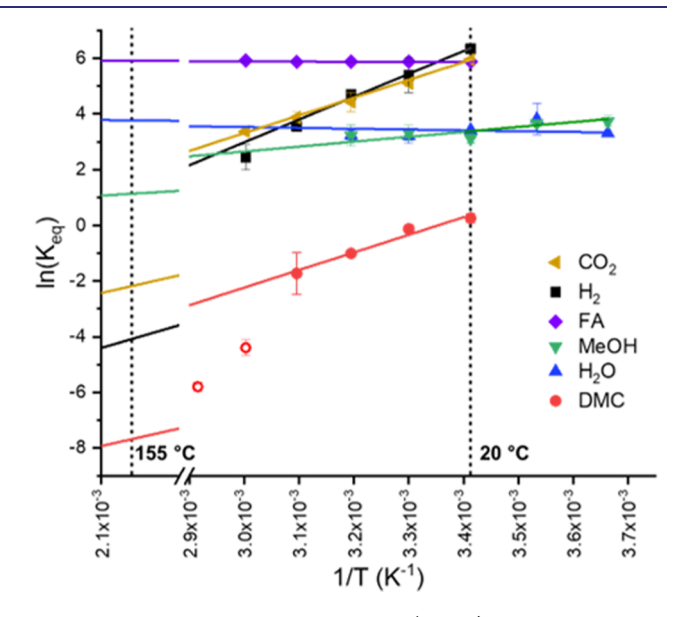


Figure 5. Overlay of van't Hoff plots for (*PNP)Ru + H-X or CO₂ in THF. Extrapolation shows the relative $K_{1,X}$ and K_2 at catalytic temperatures. $K_{\rm eq}$ has units of M $^{-1}$ for formic acid, water, and MeOH; atm $^{-1}$ for H₂ and CO₂; and is unitless for (DMA-H)(DMC). For the equilibrium with (DMA-H)(DMC), the two points that are not filled are not included in the fit.

 $^{\circ}$ C, which coincides with the temperature at which (DMA–H)(DMC) decomposes to DMA and CO₂. ³¹ We thus limit our analysis of the plot to temperatures of less than 60 $^{\circ}$ C to extrapolate the enthalpy and entropy.

Figure 5 indicates that the relative equilibrium constants vary with temperature. At the temperature of catalysis, 155 °C, the equilibria with H₂ is least favored, followed by that with CO₂. This is notable because these are the most pertinent to catalysis. We note that through extrapolation, the formation of (PNP)Ru-DMC is also expected to be unfavored at catalytic temperatures, though this equilibrium may not be pertinent at elevated temperatures (vide supra). Rather, the formation of (PNP)Ru-OCHO, (PNP)Ru-OH, and (PNP)Ru-OMe is favored. These represent equilibria with product species.

To favor the binding of H_2 to give (PNP)Ru-H at elevated temperatures, higher pressures of H_2 can be used. Increasing the pressure to 50 bar (as in catalysis, vide infra) results in a factor of \sim 50 change in the equilibrium constant (Table 1). Nonstandard conditions, whereby the concentration of H-X is less than 1 M, give lower equilibrium constants. This suggests

that catalyst inhibition will indeed increase as product concentrations rise, regardless of the catalyst loading.

The equilibrium enthalpies appear to fall into two categories. For (PNP)Ru-CO₂, (PNP)Ru-H, and (PNP)Ru-DMC, the enthalpies are significant (<-12 kcal/mol), while for all others, they are modest (>-4 kcal/mol). In all instances, proton transfer to the ligand ensues, so the difference in enthalpies must be attributed to the formation of strong Ru-X bonds and the breaking of (relatively) weak bonds (vide infra). The three species that have the least-negative enthalpies, (PNP)Ru-OH, (PNP)Ru-OCHO, and (PNP)Ru-OMe, are all produced from the reaction with Brønsted acids. Ion pairing and hydrogen bonding may lead to dissolution enthalpy and hence the larger (less negative) enthalpies. Although (PNP)Ru-DMC should fall into this category as well, the discrepancy may be attributed to the concomitant formation of DMA.

The large and negative entropy for (PNP)Ru-CO₂ and (PNP)Ru-H is consistent with adding rigidity to the linear gas molecules. The entropy associated with (PNP)Ru-DMC of -42 cal·mol⁻¹·K⁻¹ suggests significant ordering upon its formation. Because these equilibria take two molecules to one, we anticipate large negative entropies. However, this is not the case for formic acid, MeOH, and H2O, which may indicate significant solvent ordering in the free H-X or homoconjugation.³² Formic acid, MeOH, and H₂O can all hydrogen bond, and these interactions may in part increase the entropic contributions in THF.

 pK_a Measurements. In reactions that transfer net H_2 to or from a substrate, the H₂ is delivered as a hydride and a proton. This prompted us to investigate the pK_a of $(PNP)Ru^+$, (Figure 2, K_3) which is produced upon hydride transfer from (PNP)Ru-H to a substrate. Subsequent proton transfer then closes the catalytic cycle to give (*PNP)Ru. Moreover, knowledge of this pK_a , combined with the equilibrium with H₂, allows the hydricity of (PNP)Ru-H to be determined.²¹

Initial attempts to probe the pK_a of $(PNP)Ru^+$ were hampered by the coordination of the base to the Ru. The cationic 16-electron species has a vacant coordination site and allows for this. For instance, the addition of TBMP (TBMP = 2,6-di-tert-butyl-4-methylpyridine) instead led to coordination of the base. This is evident by NMR spectroscopy, whereby the ¹H and ³¹P resonances for the (PNP)Ru⁺ shift and no resonances ascribed to (*PNP)Ru are observed (Figure S28). In some instances, treatment with the base gave (*PNP)Ru as the kinetic product, but over the course of hours, it was partially converted to the base-coordinated thermodynamic product. This is the case with (Li)(NMe₂), which converts to (*PNP)Ru prior to further reacting to give a species that is consistent with (PNP)Ru-NMe₂ (Figure S30).

To circumvent this, we turned to the non-nucleophilic phosphazene bases and their conjugate acids. Upon titration of $(BTPPH)(BF_4)$ $(pK_3 = 20.2 \text{ in THF};^{33} BTPP = tert$ butylimino-tri(pyrrolidino)phosphorane) to a THF solution of (*PNP)Ru, (PNP)Ru⁺ is cleanly generated, as confirmed by NMR and UV-vis spectroscopies. Monitoring the titrations by UV-vis spectroscopy allows for the pK, of 20.7 \pm 0.2 to be determined (Figure 2, K_3). By contrast, the p K_a of the ligand, PNP, was found to be 28.6 ± 0.1 (SI), similar to that estimated by others.³⁴ Thus, the ability of the anionic nitrogen to interact strongly with a metal renders the ligand more acidic by about 8 pK_a units.

We are also interested in establishing the effect that coordinating a sixth ligand has on the pK_a . This would allow for a suitable base to be used to bias the system and leads to a more favorably release of X⁻ during catalysis. The ability to isolate both $[K][(*PNP)Ru-CO_1]$ and $(PNP)Ru-CO_2$ allows for such a comparison to be made (Figure 2, K_4). The titration of $[K][(*PNP)Ru-CO_2]$ with $(P_2EtH)(BF_4)$ gives a pK₂ of 24.6 \pm 0.4 (P₂Et = tetramethyl(tris(dimethylamino)phosphoranylidene)phosphorictriamide-Et-imin; $pK_a =$ 25.3 in THF³³). Coordination of a sixth ligand increases the ligand basicity by ~ 4 pK_a units. Together, these pK_a measurements indicate that the Ru center can greatly modulate the acidity of the ligand.

The titration of other (PNP)Ru-X (X = Cl, DMC, OCHO) species with a suitable base cleanly generates (*PNP)Ru (eq 8,

 K_{8x}). This equilibrium is formally a proton transfer followed by ligand loss and thus cannot give a true pK_a (Scheme 2). However, knowledge of the p K_a for the added base (K_{BH^+}) and an estimation of K_{7x} allows for a lower limit to the pK_a of (PNP)Ru-X to be obtained.

Scheme 2. Relationship between the Equilibrium of Equation 8 and the pK_a of (PNP)Ru-X

$$(PNP)Ru-X \rightleftharpoons [(*PNP)Ru-X]^- + H^+ \qquad K_{5x}$$

$$[(*PNP)Ru-X]^- \rightleftharpoons (*PNP)Ru + X^- \qquad K_{7x}$$

$$B + H^+ \rightleftharpoons BH^+ \qquad (K_{BH+})^{-1}$$

$$(PNP)Ru-X + B \rightleftharpoons (*PNP)Ru + BH^+ + X^- \qquad K_{8x}$$

Ligand loss from $[(*PNP)Ru-X]^-$ to (*PNP)Ru (K_{7x}) is expected to be favorable as the electron count drops from 20 to 18 (Figure 2). To probe this, 1-10 equiv of (${}^{n}Bu_{4}N$)(X) (X = Cl or OCHO) was added to a 8.4 mM d_8 -THF solution of (*PNP)Ru. No immediate change was observed by NMR spectroscopy (Figure S40), but for the chloride sample, (PNP)Ru-Cl is produced over the course of hours. This transformation necessitates a proton and likely occurs from Hofmann degradation³⁵ of the tetrabutylammonium cation, facilitating binding of the chloride. The addition of 10 equiv of (Li)(DMC) to (*PNP)Ru gave no reaction (Figure S43). Because dimethylcarbamate is more basic than formate or chloride and hence should bind most favorably to the Ru, we assume that there is no appreciable reaction of the X⁻ species binding to (*PNP)Ru. Given the limits of what we can observe, we assign a lower limit of 100 to K_{7x} . The equilibrium constant is likely to be much larger, the extent of which will vary with the identity of X⁻ (vide infra).

This analysis provides lower limits of 25 and 32 for the respective pK_a of (PNP)Ru-OCHO and (PNP)Ru-DMC. Shifting from a carboxylate to a chloride, (PNP)Ru-Cl further increases the basicity of the ligand, with a lower limit of the pK_a now being 34 (Table 2).

Hydricity and Binding Constants. The hydricity of (PNP)Ru-H can be determined from the equilibria shown in Scheme 3.

Table 2. Summary of pK_a 's and Thermodynamic Parameters Pertinent to X Release from (PNP)Ru-X

species	pK_a^a	$K_{6,X}(M)^a$	$\Delta G_{6,X}^0$ (kcal·mol ⁻¹)
(PNP)	28.6 ± 0.1		
(PNP)Ru ⁺	20.7 ± 0.2		
(PNP)Ru-CO ₂	24.6 ± 0.4		
(PNP)Ru-OCHO	>25	2×10^{-3}	3.7 ± 0.7
(PNP)Ru-DMC	>32	9.6×10^{-11}	13.7 ± 0.7
(PNP)Ru-Cl	>34	6.3×10^{-12}	15.3 ± 0.5
(PNP)Ru-H		5.0×10^{-32}	42.7 ± 0.6

^aMeasurements were made at 20 °C. We assume that the equilibrium at 25 °C is approximately that at 20 °C.

Scheme 3. Equilibria Employed to Determine the Hydricity of (PNP)Ru-H

(PNP)Ru-H = (*PNP)Ru + H2

$$(K_{1,H})^{-1}$$

 (*PNP)Ru + H+ = (PNP)Ru+
 K_3
 $H_2 = H^+ + H^ K_{H2-}$

 (PNP)Ru-H = (PNP)Ru+ H-
 $K_{6,H}$

The hydricity is obtained by combining the pK_a of (PNP)Ru+, the free energy of hydride transfer from H₂, and the free energy of H2 loss from (PNP)Ru-H. The thermochemical cycle gives a hydricity of 42.7 \pm 0.6 kcal/mol $(44.6 \pm 0.6 \text{ kcal/mol using the value of } K_{\text{H}_3}$ given in ref 37) It is difficult to draw comparisons to the hydricity of other metal complexes because this is the first reported hydricity in THF. As noted by others, hydricity values for metal complexes are solvent-dependent, 38 with no qualitative trends that convert hydricity among solvents. This is also the first hydricity value reported for a metal complex that undergoes MLC; others have measured hydricities for P₂N₂-ligated metal hydrides, ^{29,30a} whereby protonation also occurs at the ligand but subsequent proton transfer does not impact the nature of the metal-ligand bonds.

The hydricity allows for the evaluation of whether hydride transfer to a substrate, for example, CO₂, is favorable. For that to be the case, the hydricity of (PNP)Ru-H must be less than that of formate. Although it may be tempting to approximate that the hydricity of formate in THF must be greater than 42.7 kcal/mol, this is not valid in this system because the resulting formate binds to the Ru and this energy needs to be accounted for (Scheme 4). This binding may give an apparent increase in hydricity for (PNP)Ru-H, which can differ on the basis of subsequent binding of the hydride-transferred product (Scheme 4, left).

The free energy associated with the release of formate from the Ru (Scheme 4, left) can be determined from one of the two thermochemical cycles, which are described in Scheme 5.

From this analysis, the free energy for formate release is 3.7 \pm 0.7 kcal/mol (Table 2). This is appreciably less than the energy associated with DMC or chloride release, 13.7 and 15.3 kcal/mol, respectively.

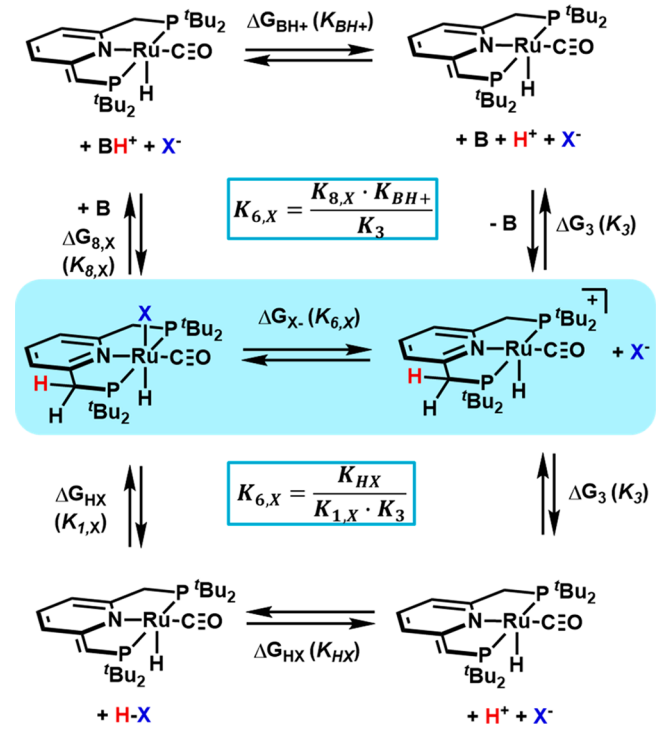
The binding of these species modifies the apparent hydricity. Formate binding gives an apparent hydricity of 39.0 kcal/mol (40.9 kcal/mol using the value of $K_{\rm H_2}^-$ given in ref 37). Given that other X⁻ species bind more tightly, it is conceivable that the apparent hydricity can be further reduced. From this and a lower limit of 520 atm⁻¹ for K_9 (Scheme 4 and Figure S24), we determine that the lower limit for the hydricity of formate in

Scheme 4. Relationship between Hydricity and the Binding of Formate to [(PNP)Ru]+a

$$K_{9} = \frac{K_{6,H}}{K_{H-(OCHO)} \cdot K_{6,OCHO}}$$

$$K_{1} = \frac{K_{1} \cdot K_{1} \cdot K_$$

Scheme 5. Thermochemical Cycles That Can Be Employed to Determine $K_{6,X}^{a}$



^aHighlighted in blue.

THF is 42.7 kcal/mol (44.7 kcal/mol when using the values of ref 37). For comparison, $\Delta G_{\rm H-(OCHO)}$ is estimated to be 44 kcal/mol in MeCN and 24.1 kcal/mol in water.²¹

The thermochemical cycles of Scheme 5 allow for the evaluation of the pK_a 's of H-OCHO and H-DMC in THF. Values of 20.8 \pm 0.6 and 30.6 \pm 0.6 are obtained, respectively. The value obtained for formic acid is similar to that of acetic acid in THF (22.5),39 further validating our equilibration studies.

Catalytic Hydrogenation of CO₂. The hydrogenation of (DMA-H)(DMC) by (PNP)Ru-Cl was probed (Table 3). The use of dimethylammonium dimethylcarbamate as a CO₂

Table 3. Hydrogenation of (DMA-H)(DMC) by (PNP)Ru-Cl^a

entry	[catalyst] (mM) (mol %)	substrate	base	TON MeOH $(mM)^b$	TON Formate (mM) ^c	TON DMF $(mM)^b$
1	0.05 (1%)	$(DMA-H)(DMC)^h$	^t BuOK	$3.9 \pm 0.3(0.20)$	$3.3 \pm 0.2(0.17)$	$19.8 \pm 5.4(4.1)$
2	0.5 (1%)	$(DMA-H)(DMC)^h$	^t BuOK	$4.0 \pm 0.2(2.1)$	$5.3 \pm 0.2(2.6)$	$57.2 \pm 15.8 (140)$
3	1.5 (1%)	$(DMA-H)(DMC)^h$	^t BuOK	$1.2 \pm 0.2(1.7)$	$0.6 \pm 0.1(0.90)$	$0.5 \pm 0.3(57)$
4	3.3 (1%)	$(DMA-H)(DMC)^h$	^t BuOK	$0.5 \pm 0.1(1.7)$	$0.3 \pm 0.1(0.98)$	n.d. ^f
5	5.3 (1%)	$(DMA-H)(DMC)^h$	^t BuOK	$0.4 \pm 0.1(2.0)$	$0.8 \pm 0.1(4.5)$	$0.3 \pm 0.3 \; (0.016)$
6^d	0.05 (1%)	$(DMA-H)(DMC)^h$	none	$2.0 \pm 0.7(0.065)$	$0.7 \pm 0.4(0.046)$	n.d. ^f
7	0.05 (1%)	$(DMA-H)(DMC)^h$	K_3PO_4	$2.6 \pm 0.5(0.14)$	$1.6 \pm 0.7(0.23)$	$10.9 \pm 7.7(4.1)$
8	0.05 (1%)	$(DMA-H)(DMC)^h$	(Li)(DMC) ^e	$39.4 \pm 0.4(2.0)$	$6.3 \pm 5.7(0.32)$	$0.5 \pm 0.4 \; (0.00095)$
9	0.05 (1%)	$(DMA-H)(DMC)^h$	$(Li)(Me_2N)$	$1.6 \pm 0.3(0.078)$	$0.7 \pm 0.4(0.035)$	$1.0 \pm 1.0 \ (0.001)$
10	0.05 (1%)	(Li)(DMC)	none	$7.5 \pm 4.9(0.38)$	$1.3 \pm 0.5(0.065)$	n.d. ^f
11	0.05 (1%)	НСООН	^t BuOK	$1.2 \pm 0.6(0.062)$	g	n.d. ^f
12	0.05 (1%)	DMF	^t BuOK	$59.2 \pm 2.3(2.9)$	$0.7 \pm 0.3(3.6 \times 10^{-5})$	g

"All reactions are run in 10 mL of THF. "Quantified by GC. The error is from duplicate catalytic runs." Quantified by IC. The error is from duplicate catalytic runs. "(*PNP)Ru was used as the catalyst." 100 equiv of base was employed. In.d. = not detected. Not quantified. 102 equiv of substrate was employed.

surrogate for hydrogenation to MeOH was first shown by Sanford by the use of a related Ru catalyst. To draw comparisons, similar conditions were employed in terms of substrate and base equivalents, temperature, and solvent. We first examined the effect of catalyst concentration on conversion to MeOH, formate, and DMF while maintaining a constant loading of 1 mol % (entries 1-5). As the catalyst concentration is increased from 0.05 to 5.3 mM, the TON of MeOH decreases. When the amount of MeOH produced is viewed instead as the concentration of MeOH, we see that except for 0.05 mM catalyst the final concentration of MeOH is essentially constant (~2 mM). This suggests to us that there might be a deactivation mechanism that is dependent on the concentration of MeOH and/or H2O. Indeed, during our equilibrium studies of (*PNP)Ru and MeOH/H₂O, we saw irreversible decomposition at elevated temperatures to intractable Ru species (SI).

We then consider the effect of the base strength (entries 1 and 6–9). Going from K_3PO_4 to 'BuOK gives an increase in MeOH production. Although the pK_a 's of K_3PO_4 and 'BuOK are not known in THF, we note that the former is not capable of converting (PNP)Ru–Cl to (*PNP)Ru at room temperature whereas the latter can, suggesting that 'BuOK is more basic. When we use (Li)(DMC) as the base, we see an order of magnitude increase in TON to 39.4. Now, we reach our limiting concentration of MeOH produced with 0.05 mM catalyst loading. However, with (Li)(Me₂N) the TON drops to 1.6. We attribute this decrease to competitive amine binding which may occur at elevated temperatures. With ($^{Ph}P^HNP$)-Ru–(HBH₃), which is known to hydrogenate carbamates to MeOH, ^{7a,b} we see no effect on varying the base ('BuOK vs K_3PO_4) on MeOH yield (SI).

Given that the produced H₂O may quench 1 equiv of base, we also investigated using equimolar substrate and base. When we use equimolar ^tBuOK and (DMA–H)(DMC), we see a slight decrease in TON compared to when we use 1:2 base/substrate (Table S4). A decrease is also observed when we use 1:4 base/substrate. We interpret these results as suggesting an intricate balance between the requirement of the base and the

impact of adding base to the equilibrium of (DMA-H)(DMC) and $DMA + CO_2$ (with base favoring the formation of DMC salts).

To determine if there is a substrate which is limiting TON, we compared the substrate (entries 1 and 10-12). Going from (DMA-H)(DMC) to (Li)(DMC), we see a doubling of the MeOH TON. This may be due to lower concentrations of amine (DMA-H $^+$ versus Li $^+$) or discrepancies in how readily CO $_2$ is released from DMC. Formic acid is poorly hydrogenated, which may be due to the now acidic nature of the reaction medium because only 50 equiv of base was added. When DMF is employed as a substrate, we see MeOH produced with a TON of 59.2, again giving a similar limiting final concentration.

DISCUSSION

Ramifications of H-X Equilibria on Catalysis. Given the concentration (or pressure) dependence for the equilibria of (*PNP)Ru and H-X or CO₂, it is imperative to understand how different catalyst loadings impact TON. Regardless of the catalyst concentration, only the H-X concentration will determine the equilibrium position. This is illustrated when considering the TON of MeOH produced. Although varying the catalyst loading impacts the TON for MeOH, at the four highest loadings considered it did not impact the overall concentration of MeOH produced, ~2 mM. This same concentration can be obtained at lower catalyst loading when using (Li)(DMC) as the base. Strikingly, when DMF is instead used as a substrate, the same concentration of MeOH is produced. This suggests that competitive equilibria may limit the overall MeOH production. Indeed, at elevated temperatures, the equilibrium to give (PNP)Ru-OMe is favored over that of (PNP)Ru-H. In this system, further complication likely arises from the instability of (*PNP)Ru to excess MeOH at elevated temperatures; the turnover ability of the catalyst suggests that this deactivating equilibrium is less favorable than that which gives productive turnover.

A threshold MeOH concentration is not unique to our system. Both Sanford and Prakash have used (PhPHNP)Ru-Cl

and (PhPHNP)Ru-(HBH3) to hydrogenate CO2 to MeOH in the presence of a variety of amines. Under their conditions, Sanford reports a maximum MeOH concentration of about 1 M.^{7b} In three separate reports, Prakash reports maximum MeOH concentrations of 1.3¹⁴ and 2.1 M.^{7a,40} That the same catalyst, run under different conditions, in different solvents, amines, and base additives, gives a similar maximum MeOH concentration suggests that a concentration-dependent equilibrium between MeOH and the catalyst contributes to catalyst performance. Related Ru catalysts that undergo MLC via dearomatization give ~1 M limiting MeOH concentrations in other types of hydrogenations. 7c,26b The discrepancy between the catalysts likely has contributions from differences in equilibrium constants, and in the latter systems, different H-X species are present and hence there are different competing equilibria. However, these similarities suggest that a better parameter for evaluating catalysis is product concentration, not TON.

Knowing both the concentration dependence and temperature dependence of these equilibria $(K_{1,X})$ allows for a better understanding of how to optimize reaction conditions. In general, the equilibrium constant toward (PNP)Ru-X decreases with temperature, and the substrates fall into two classes that differ by the magnitude of this effect. Our study shows that the decrease is not uniform across all substrates. Thus, the equilibrium with formic acid is more or less temperature-independent, while that with H₂ shows a strong decrease with increasing temperature. If the formation of (PNP)Ru-OCHO does indeed represent a thermodynamic bottleneck or the most favorable equilibrium, then increasing the temperature would not favor the formation of (PNP)Ru-H; only raising the pressure or lowering the temperature would do so. Varying the temperature and concentrations can likewise impact the thermodynamic bottlenecks, the extent of which would not be known without studies such as this.

These findings are not unique to the hydrogenation of carbamates to MeOH. For example, using (PhPHNP)Ru-(HBH₃), the optimal temperature for CO₂ hydrogenation to DMF (in the presence of DMA) is found to be 95 °C, ^{7b} well below the 155 °C used to hydrogenate the produced DMF to MeOH. This is consistent with the idea of the relative equilibria shifting with temperature. Also, a recent study on the dehydrogenative coupling of ethylenediamine and MeOH to give ethylene urea and H₂ showed that increasing the headspace volume, effectively decreasing the [H₂], enhances this Ru-catalyzed reaction. ⁴¹ These studies on related Ru catalysts that undergo MLC reinforce the need to understand the thermodynamic parameters associated with the catalyst; this allows for optimization of the catalytic conditions.

Knowledge of the temperature and pressure dependence for the H₂ equilibrium versus that with CO₂ is also pertinent to CO₂ hydrogenation. With regard to hydrogenation to formate, Pidko has suggested that (PNP)Ru-CO₂ is an inhibitive offcycle species, ^{2c} and Sanford suggests that the related (PNN)Ru-CO₂ may be able to function as a catalyst, albeit at a slower rate; ^{2a} this species should therefore be minimized under catalytic conditions. Our studies indicate that at all elevated temperatures, the equilibrium with CO₂ is favored over that of H₂ and thus pressure differences must be employed. Although this is usually achieved by changing the partial pressures of the two gases, it can also be achieved by using "captured CO₂" in the form of carbamates and carbamic acid. These are in equilibria with free CO₂ (eq 9).

$$CO_2 + R_2NH \rightleftharpoons R_2N^+(H)(COO^-) \rightleftharpoons R_2N-COOH$$

$$\stackrel{R'_2NH}{\Longleftrightarrow} [R_2N-COO][R'_2NH_2]$$
(9)

Moreover, it has been shown that by changing the amine identity or using mixtures of amines, the pressure and temperature requirements for releasing CO_2 can be greatly modified. This relative equilibrium is particularly pertinent to carbon capture and recycling schemes because CO_2 release is energy-intensive. Coupling release to catalysis will streamline the process, and by a judicious choice of amine, it will allow for tailoring $\mathrm{H}_2/\mathrm{CO}_2$ to optimize catalysis.

Rationalization of the Need for a Strong Base during Catalysis. It is established that using (PNP)Ru-Cl with DBU as a cosubstrate base allows for CO2 hydrogenation to formate.^{2d,20} Although DBU, having a pK_a of 16.1 in THF,³⁹ is not sufficiently basic enough to deprotonate (PNP)Ru-OCHO at room temperature, the precipitation of (DBU-H)(OCHO) is not accounted for nor are subsequent equilibria with the product (*PNP)Ru, both of which could drive the reaction. It is thus conceivable that under reaction conditions, which include elevated temperatures, this deprotonation readily occurs. Indeed, treatment of (PNP)Ru-Cl with K₃PO₄ at room temperature gives no reaction, but upon warming to 120 °C, the formation of (*PNP)Ru ensues, as evident by the characteristic color change from yellow to green. Cooling the sample causes it to revert back to (PNP)Ru-Cl. There is thus a temperature dependence on the pK_{2} , but deconvoluting the contribution of the inorganic base and the Ru species is not trivial.

Our results suggest that using a stronger base allows for and increases MeOH production when (PNP)Ru-Cl is used as a catalyst for the hydrogenation of (DMA-H)(DMC). Given the amount of base added, we cannot conclude whether it is a coreagent or a cocatalyst. Others have noted that in related hydrogenations the addition of a base enhances catalysis, though the base is added in substoichiometric amounts. The late is speculated that the base enhances the MLC mechanism, and thus the base strength may alter the mechanism.

As noted by others, K_3PO_4 is sufficient for MeOH production when ($^{Ph}P^HNP$)Ru(HBH₃) is used as the catalyst for the hydrogenation of (DMA–H)(DMC). Ta Changing the base to K^tBuOK does not improve MeOH production. By contrast, with (PNP)Ru–X a stronger base is required. This suggests that the base is used to deprotonate the catalyst. The alternative deprotonation of an organic intermediate would show the same base dependence, regardless of the catalyst.

This can be rationalized by considering our pK_a measurements, which indicate that six-coordinate (PNP)Ru-X species are at least 5 pK_a units more basic than five-coordinate (PNP)Ru⁺. Thus, the addition of a strong base can bias the system to regenerate (*PNP)Ru. It should be noted that of the six-coordinate (PNP)Ru-X species whose pK_a we could estimate, (PNP)Ru-OCHO, gave the lowest value, consistent with a relatively weak base (DBU) facilitating this hydrogenation. Additionally, our equilibrium studies indicate that (PNP)Ru-OCHO does not readily dissociate formic acid, even at elevated temperatures. This suggests that the only way to turn over the catalyst is to use a base. Our best results for MeOH production used (Li)(DMC) as the base. From our thermochemical cycles, the pK_a of DMC-H, dimethylcarbamic acid, is 30.6, significantly higher than the DBU that is needed

for formate. It therefore may serve to deprotonate a (PNP)Ru-X species that is pertinent to DMF hydrogenation.

Hydricity is Modified by the Binding of a Substrate. Miller and co-workers recently disclosed how the hydricity of Ru and Ir hydrides varies in H₂O with added buffers that can coordinate to the metal.⁴³ In their work, they found that the binding of H₂O versus Cl⁻ can alter the apparent hydricity by about 3–5 kcal/mol. Although their studies focused on buffers, here we extend this idea to how the coordination of the product of hydride transfer impacts the apparent hydricity.

Our analysis gives a hydricity of 42.7 kcal/mol for (PNP)Ru-H in THF. This is the value to consider if the substrate does not coordinate to the Ru as part of the catalytic cycle. However, our thermodynamic studies indicate that substrate binding is favorable, giving (PNP)Ru-X. This binding is favorable by ~4-15 kcal/mol and hence can greatly impact the apparent hydricity. If hydrogenation does occur via coordination of the product of hydride transfer, for example, formate, then the catalyst hydricity does not need to be greater than that of formate. Rather, the catalyst hydricity and binding affinity for the product must be larger than that of formate. Because of the inability to isolate (PNP)Ru-OMe, we are unable to determine the methoxide binding affinity. However, Table 2 suggests that it may differ from that of formate and require hydricity parameters different from those of the catalyst.

CONCLUSIONS

We presented a thorough thermochemical analysis of the Ru PNP hydrogenation catalyst. The temperature-dependent equilibrium studies suggest what may be thermodynamic bottlenecks and how they vary with temperature. At elevated temperatures, (PNP)Ru-OCHO formation is favored over (PNP)Ru-H by 4 orders of magnitude in $K_{1,X}$. This explains why formic acid is not readily released but rather a base is required to convert (PNP)Ru-OCHO to (*PNP)Ru. A stronger base is required in this system to drive the hydrogenation of (DMA-H)(DMC) to MeOH, whereas this is not a requirement in related systems. We find that the pK_a of (PNP)Ru-X varies greatly with the identity of the X-ligand and hence suggests that the stronger base is required to deprotonate a six-coordinate Ru species that is bound by an intermediate en route to MeOH production. Our hydrogenation studies indicate that there is a limiting methanol concentration that is reached with this system. Although there are likely many factors to this, the equilibria studies are consistent with this observation and likely contribute to performance. We also give a lower estimate for the hydricity of formate in THF and indicate how substrate binding can impact the apparent hydricity of a catalyst by several kcal/mol. This work mirrors that done in the electrochemical field, whereby such findings have allowed for better H2 evolution catalysts to be developed and have helped ascertain catalyst requirements for electrocatalytic CO₂ reduction. 15,16 Although this work benchmarks several thermochemical properties pertinent to CO₂ hydrogenation catalysts, we envision that our findings will be broadly applicable to a variety of other catalytic reactions performed by this and related catalysts that require cooperation between the metal and bifunctional ligand.

ASSOCIATED CONTENT

S Supporting Information

The Supporting Information is available free of charge on the ACS Publications website at DOI: 10.1021/jacs.9b06760.

Experimental details, including syntheses, NMR and UV-vis data, and equilibrium plots (PDF) Crystallographic data (CIF)

AUTHOR INFORMATION

Corresponding Author

*caroline.saouma@utah.edu

ORCID ®

Cheryl L. Mathis: 0000-0003-4738-3240 Jackson Geary: 0000-0003-3489-2716 Yotam Ardon: 0000-0002-7720-2634 Maxwell S. Reese: 0000-0002-7891-3542 Mallory A. Philliber: 0000-0002-6758-7876 Ryan T. VanderLinden: 0000-0002-0128-1284 Caroline T. Saouma: 0000-0003-1170-6175

Notes

The authors declare no competing financial interest.

ACKNOWLEDGMENTS

The authors gratefully acknowledge start-up funding from the University of Utah and USTAR, ACS PRF (57058-DNI3), and NSF REU (1659579).

REFERENCES

- (1) (a) Khusnutdinova, J. R.; Milstein, D. Metal-Ligand Cooperation. *Angew. Chem., Int. Ed.* **2015**, *54*, 12236. (b) Alig, L.; Fritz, M.; Schneider, S. First-Row Transition Metal (De)Hydrogenation Catalysis Based On Functional Pincer Ligands. *Chem. Rev.* **2019**, *119*, 2681. (c) Gunanathan, C.; Milstein, D. Bond Activation and Catalysis by Ruthenium Pincer Complexes. *Chem. Rev.* **2014**, *114*, 12024.
- (2) Examples with Ru: (a) Huff, C. A.; Sanford, M. S. Catalytic CO₂ Hydrogenation to Formate by a Ruthenium Pincer Complex. ACS Catal. 2013, 3, 2412. (b) Filonenko, G. A.; Smykowski, D.; Szyja, B. M.; Li, G.; Szczygieł, J.; Hensen, E. J. M.; Pidko, E. A. Catalytic Hydrogenation of CO₂ to Formates by a Lutidine-Derived Ru-CNC Pincer Complex: Theoretical Insight into the Unrealized Potential. ACS Catal. 2015, 5, 1145. (c) Filonenko, G. A.; Hensen, E. J. M.; Pidko, E. A. Mechanism of CO₂ hydrogenation to formates by homogeneous Ru-PNP pincer catalyst: from a theoretical description to performance optimization. Catal. Sci. Technol. 2014, 4, 3474. (d) Filonenko, G. A.; Conley, M. P.; Copéret, C.; Lutz, M.; Hensen, E. J. M.; Pidko, E. A. The impact of Metal-Ligand Cooperation in Hydrogenation of Carbon Dioxide Catalyzed by Ruthenium PNP Pincer. ACS Catal. 2013, 3, 2522.
- (3) Examples with Ir: (a) Tanaka, R.; Yamashita, M.; Nozaki, K. Catalytic Hydrogenation of Carbon Dioxide Using Ir(III)-Pincer Complexes. J. Am. Chem. Soc. 2009, 131, 14168. (b) Schmeier, T. J.; Dobereiner, G. E.; Crabtree, R. H.; Hazari, N. Secondary Coordination Sphere Interactions Facilitate the Insertion Step in an Iridium(III) CO₂ Reduction Catalyst. J. Am. Chem. Soc. 2011, 133, 9274.
- (4) Examples with first row transition metals: (a) Langer, R.; Diskin-Posner, Y.; Leitus, G.; Shimon, L. J. W.; Ben-David, Y.; Milstein, D. Low-Pressure Hydrogenation of Carbon Dioxide Catalyzed by an Iron Pincer Complex Exhibiting Noble Metal Activity. *Angew. Chem., Int. Ed.* 2011, 50, 9948. (b) Bernskoetter, W. H.; Hazari, N. Reversible Hydrogenation of Carbon Dioxide to Formic Acid and Methanol: Lewis Acid Enhancement of Base Metal Catalysts. *Acc. Chem. Res.* 2017, 50, 1049. (c) Bielinski, E. A.; Lagaditis, P. O.; Zhang, Y.;

- Mercado, B. Q.; Würtele, C.; Bernskoetter, W. H.; Hazari, N.; Schneider, S. Lewis Acid-Assisted Formic Acid Dehydrogenation Using a Pincer-Supported Iron Catalyst. *J. Am. Chem. Soc.* **2014**, *136*, 10234. (d) Bertini, F.; Glatz, M.; Gorgas, N.; Stöger, B.; Peruzzini, M.; Veiros, L. F.; Kirchner, K.; Gonsalvi, L. Carbon dioxide hydrogenation catalysed by well-defined Mn(I) PNP pincer hydride complexes. *Chem. Sci.* **2017**, *8*, 5024.
- (5) Examples with Ru: Zhang, L.; Han, Z.; Zhao, X.; Wang, Z.; Ding, K. Highly Efficient Ruthenium-Catalyzed N-Formylation of Amines with H₂ and CO₂. Angew. Chem., Int. Ed. **2015**, 54, 6186.
- (6) Examples with first row transition metals: (a) Jayarathne, U.; Hazari, N.; Bernskoetter, W. H. Selective Iron-Catalyzed N-Formylation of Amines using Dihydrogen and Carbon Dioxide. ACS Catal. 2018, 8, 1338. (b) Daw, P.; Chakraborty, S.; Leitus, G.; Diskin-Posner, Y.; Ben-David, Y.; Milstein, D. Selective N-Formylation of Amines with H₂ and CO₂ Catalyzed by Cobalt Pincer Complexes. ACS Catal. 2017, 7, 2500.
- (7) Examples with Ru: (a) Kothandaraman, J.; Goeppert, A.; Czaun, M.; Olah, G. A.; Prakash, G. K. S. Conversion of CO₂ from Air into Methanol Using a Polyamine and a Homogeneous Ruthenium Catalyst. J. Am. Chem. Soc. 2016, 138, 778. (b) Rezayee, N. M.; Huff, C. A.; Sanford, M. S. Tandem Amine and Ruthenium-Catalyzed Hydrogenation of CO₂ to Methanol. J. Am. Chem. Soc. 2015, 137, 1028. (c) Khusnutdinova, J. R.; Garg, J. A.; Milstein, D. Combining Low-Pressure CO₂ Capture and Hydrogenation To Form Methanol. ACS Catal. 2015, 5, 2416. (d) Everett, M.; Wass, D. F. Highly productive CO₂ hydrogenation to methanol a tandem catalytic approach via amide intermediates. Chem. Commun. 2017, 53, 9502.
- (8) Examples with first row transition metals: (a) Ribeiro, A. P. C.; Martins, L. M. D. R. S.; Pombeiro, A. J. L. Carbon dioxide-to-methanol single-pot conversion using a C-scorpionate iron(II) catalyst. *Green Chem.* **2017**, *19*, 4811. (b) Kar, S.; Goeppert, A.; Kothandaraman, J.; Prakash, G. K. S. Manganese-Catalyzed Sequential Hydrogenation of CO₂ to Methanol via Formamide. *ACS Catal.* **2017**, 7, 6347.
- (9) Wang, W.-H.; Himeda, Y.; Muckerman, J. T.; Manbeck, G. F.; Fujita, E. CO₂ Hydrogenation to Formate and Methanol as an Alternative to Photo- and Electrochemical CO₂ Reduction. *Chem. Rev.* **2015**, *115*, 12936.
- (10) Yang, X. Hydrogenation of Carbon Dioxide Catalyzed by PNP Pincer Iridium, Iron, and Cobalt Complexes: A Computational Design of Base Metal Catalysts. ACS Catal. 2011, 1, 849.
- (11) (a) Schneidewind, J.; Adam, R.; Baumann, W.; Jackstell, R.; Beller, M. Low-Temperature Hydrogenation of Carbon Dioxide to Methanol with a Homogeneous Cobalt Catalyst. *Angew. Chem., Int. Ed.* **2017**, *56*, 1890. (b) Wesselbaum, S.; Moha, V.; Meuresch, M.; Brosinski, S.; Thenert, K. M.; Kothe, J.; Stein, T. v.; Englert, U.; Hölscher, M.; Klankermayer, J.; Leitner, W. Hydrogenation of carbon dioxide to methanol using a homogeneous ruthenium-Triphos catalyst: from mechanistic investigations to multiphase catalysis. *Chem. Sci.* **2015**, *6*, 693. (c) Wesselbaum, S.; Stein, T. V.; Klankermayer, J.; Leitner, W. Hydrogenation of Carbon Dioxide to Methanol by Using a Homogeneous Ruthenium-Phosphine Catalyst. *Angew. Chem., Int. Ed.* **2012**, *51*, 7499. (d) Huff, C. A.; Sanford, M. S. Cascade Catalysis for the Homogeneous Hydrogenation of CO₂ to Methanol. *J. Am. Chem. Soc.* **2011**, *133*, 18122.
- (12) Vitillo, J. G.; Smit, B.; Gagliardi, L. Introduction: Carbon Capture and Separation. *Chem. Rev.* **2017**, *117*, 9521.
- (13) Heldebrant, D. J.; Koech, P. K.; Glezakou, V.-A.; Rousseau, R.; Malhotra, D.; Cantu, D. C. Water-Lean Solvents for Post-Combustion CO₂ Capture: Fundamentals, Uncertainties, Opportunities, and Outlook. *Chem. Rev.* **2017**, *117*, 9594.
- (14) Kar, S.; Sen, R.; Kothandaraman, J.; Goeppert, A.; Chowdhury, R.; Munoz, S. B.; Haiges, R.; Prakash, G. K. S. Mechanistic Insights into Ruthenium-Pincer-Catalyzed Amine-Assisted Homogeneous Hydrogenation of CO₂ to Methanol. *J. Am. Chem. Soc.* **2019**, *141*, 3160.
- (15) (a) DuBois, D. L. Development of Molecular Electrocatalysts for Energy Storage. *Inorg. Chem.* **2014**, *53*, 3935. (b) Helm, M. L.;

- Stewart, M. P.; Bullock, R. M.; DuBois, M. R.; DuBois, D. L. A Synthetic Nickel Electrocatalyst with a Turnover Frequency Above $100,000~\rm s^{-1}$ for $\rm H_2$ Production. *Science* **2011**, 333, 863. (c) Sherbow, T. J.; Fettinger, J. C.; Berben, L. A. Control of Ligand p $\rm K_a$ Values Tunes the Electrocatalytic Dihydrogen Evolution Mechanism in a Redox-Active Aluminum(III) Complex. *Inorg. Chem.* **2017**, 56, 8651. (d) Rountree, E. S.; Martin, D. J.; McCarthy, B. D.; Dempsey, J. L. Linear Free Energy Relationships in the Hydrogen Evolution Reaction: Kinetic Analysis of a Cobaloxime Catalyst. *ACS Catal.* **2016**, *6*, 3326.
- (16) (a) Taheri, A.; Thompson, E. J.; Fettinger, J. C.; Berben, L. A. An Iron Electrocatalyst for Selective Reduction of CO₂ to Formate in Water: Including Thermochemical Insights. *ACS Catal.* **2015**, *5*, 7140. (b) Waldie, K. M.; Ostericher, A. L.; Reineke, M. H.; Sasayama, A. F.; Kubiak, C. P. Hydricity of Transition-Metal Hydrides: Thermodynamic Considerations for CO₂ Reduction. *ACS Catal.* **2018**, *8*, 1313. (17) Jeletic, M. S.; Hulley, E. B.; Helm, M. L.; Mock, M. T.; Appel,
- (17) Jeletic, M. S.; Hulley, E. B.; Helm, M. L.; Mock, M. T.; Appel, A. M.; Wiedner, E. S.; Linehan, J. C. Understanding the Relationship Between Kinetics and Thermodynamics in CO₂ Hydrogenation Catalysis. *ACS Catal.* **2017**, *7*, 6008.
- (18) (a) Gnanaprakasam, B.; Zhang, J.; Milstein, D. Direct Synthesis of Imines from Alcohols and Amines with Liberation of H₂. Angew. Chem., Int. Ed. **2010**, 49, 1468. (b) Gnanaprakasam, B.; Balaraman, E.; Ben-David, Y.; Milstein, D. Synthesis of Peptides and Pyrazines from β-Amino Alcohols through Extrusion of H₂ Catalyzed by Ruthenium Pincer Complexes: Ligand-Controlled Selectivity. Angew. Chem., Int. Ed. **2011**, 50, 12240. (c) Xie, Y.; Ben-David, Y.; Shimon, L. J. W.; Milstein, D. Highly Efficient Process for Production of Biofuel from Ethanol Catalyzed by Ruthenium Pincer Complexes. J. Am. Chem. Soc. **2016**, 138, 9077.
- (19) (a) Zeng, R.; Feller, M.; Ben-David, Y.; Milstein, D. Hydrogenation and Hydrosilylation of Nitrous Oxide Homogeneously Catalyzed by a Metal Complex. *J. Am. Chem. Soc.* **2017**, *139*, 5720. (b) Mukherjee, A.; Srimani, D.; Ben-David, Y.; Milstein, D. Low-Pressure Hydrogenation of Nitriles to Primary Amines Catalyzed by Ruthenium Pincer Complexes. Scope and mechanism. *Chem-CatChem* **2017**, *9*, 559.
- (20) Li, Z.; Rayder, T. M.; Luo, L.; Byers, J. A.; Tsung, C.-K. Aperture-Opening Encapsulation of a Transition Metal Catalyst in a Metal-Organic Framework for ${\rm CO_2}$ Hydrogenation. *J. Am. Chem. Soc.* **2018**, *140*, 8082.
- (21) Wiedner, E. S.; Chambers, M. B.; Pitman, C. L.; Bullock, R. M.; Miller, A. J. M.; Appel, A. M. Thermodynamic Hydricity of Transition Metal Hydrides. *Chem. Rev.* **2016**, *116*, 8655.
- (22) Bauer, J. O.; Leitus, G.; Ben-David, Y.; Milstein, D. Direct Synthesis of Symmetrical Azines from Alcohols and Hydrazine Catalyzed by a Ruthenium Pincer Complex: Effect of Hydrogen Bonding. ACS Catal. 2016, 6, 8415.
- (23) Montag, M.; Zhang, J.; Milstein, D. Aldehyde Binding through Reversible C-C Coupling with the Pincer Ligand upon Alcohol Dehydrogenation by a PNP-Ruthenium Catalyst. *J. Am. Chem. Soc.* **2012**, *134*, 10325.
- (24) Vogt, M.; Gargir, M.; Iron, M. A.; Diskin-Posner, Y.; Ben-David, Y.; Milstein, D. A New Mode of Activation of CO₂ by Metal-Ligand Cooperation with Reversible C-C and M-O Bond Formation at Ambient Temperature. *Chem. Eur. J.* **2012**, *18*, 9194.
- (25) Kothandaraman, J.; Goeppert, A.; Czaun, M.; Olah, G. A.; Surya Prakash, G. K. CO₂ capture by amines in aqueous media and its subsequent conversion to formate with reusable ruthenium and iron catalysts. *Green Chem.* **2016**, *18*, 5831.
- (26) For the instability of related species with the PNN ligand, see (a) Kohl, S. W.; Weiner, L.; Schwartsburd, L.; Konstantinovski, L.; Shimon, L. J. W.; Ben-David, Y.; Iron, M. A.; Milstein, D. Consecutive Thermal H₂ and Light-Induced O₂ Evolution from Water Promoted by a Metal Complex. *Science* 2009, 324, 74. (b) Balaraman, E.; Gunanathan, C.; Zhang, J.; Shimon, L. J. W.; Milstein, D. Efficient hydrogenation of organic carbonates, carbamates and formates indicates alternative routes to methanol based on CO2 and CO. *Nat. Chem.* 2011, 3, 609.

- (27) Zhang, L.; Nguyen, D. H.; Raffa, G.; Trivelli, X.; Capet, F.; Desset, S.; Paul, S.; Dumeignil, F.; Gauvin, R. M. Catalytic Conversion of Alcohols into Carboxylic Acid Salts in Water: Scope, Recycling, and Mechanistic Insights. *ChemSusChem* **2016**, *9*, 1413.
- (28) Huff, C. A.; Kampf, J. W.; Sanford, M. S. Reversible carbon-carbon bond formation between carbonyl compounds and a ruthenium pincer complex. *Chem. Commun.* **2013**, *49*, 7147.
- (29) Lilio, A. M.; Reineke, M. H.; Moore, C. E.; Rheingold, A. L.; Takase, M. K.; Kubiak, C. P. Incorporation of Pendant Bases into Rh(diphosphine)₂ Complexes: Synthesis, Thermodynamic Studies, and Catalytic CO₂ Hydrogenation Activity of [Rh(P₂N₂)₂]⁺ Complexes. J. Am. Chem. Soc. 2015, 137, 8251.
- (30) (a) Lense, S.; Ho, M.-H.; Chen, S.; Jain, A.; Raugei, S.; Linehan, J. C.; Roberts, J. A. S.; Appel, A. M.; Shaw, W. Incorporating Amino Acid Esters into Catalysts for Hydrogen Oxidation: Steric and Electronic Effects and the Role of Water as a Base. *Organometallics* **2012**, *31*, 6719. (b) Wilson, A. D.; Newell, R. H.; McNevin, M. J.; Muckerman, J. T.; DuBois, M. R.; DuBois, D. L. Hydrogen Oxidation and Production Using Nickel-Based Molecular Catalysts with Positioned Proton Relays. *J. Am. Chem. Soc.* **2006**, *128*, 358.
- (31) Chen, L.; Guo, S.-X.; Li, F.; Bentley, C.; Horne, M.; Bond, A. M.; Zhang, J. Electrochemical Reduction of CO₂ at Metal Electrodes in a Distillable Ionic Liquid. *ChemSusChem* **2016**, *9*, 1271.
- (32) McCarthy, B. D.; Martin, D. J.; Rountree, E. S.; Ullman, A. C.; Dempsey, J. L. Electrochemical Reduction of Brønsted Acids by Glassy Carbon in Acetonitrile—Implications for Electrocatalytic Hydrogen Evolution. *Inorg. Chem.* **2014**, *53*, 8350.
- (33) Kaljurand, I.; Saame, J.; Rodima, T.; Koppel, I.; Koppel, I. A.; Kögel, J. F.; Sundermeyer, J.; Köhn, U.; Coles, M. P.; Leito, I. Experimental Basicities of Phosphazene, Guanidinophosphazene, and Proton Sponge Superbases in the Gas Phase and Solution. *J. Phys. Chem. A* **2016**, *120*, 2591.
- (34) Simler, T.; Karmazin, L.; Bailly, C.; Braunstein, P.; Danopoulos, A. A. Potassium and Lithium Complexes with Monodeprotonated, Dearomatized PNP and PNC^{NHC} Pincer-Type Ligands. *Organometallics* **2016**, 35, 903.
- (35) Francke, R.; Schille, B.; Roemelt, M. Homogeneously Catalyzed Electroreduction of Carbon Dioxide—Methods, Mechanisms, and Catalysts. *Chem. Rev.* **2018**, *118*, 4631.
- (36) (a) Buncel, E.; Menon, B. Carbanion Mechanisms. 6. Metalation of Arylmethanes by Potassium Hydride/18-Crown-6 Ether in Tetrahydrofuran and the Acidity of Hydrogen. *J. Am. Chem. Soc.* 1977, 99, 4457. (b) Morris, R. H. Brønsted-Lowry Acid Strength of Metal Hydride and Dihydrogen Complexes. *Chem. Rev.* 2016, 116, 8588.
- (37) Brereton, K.; Jadrich, C.; Stratakes, B.; Miller, A. J. M. Organometallics 2019, DOI: 10.1021/acs.organomet.9b00278.
- (38) Tsay, C.; Livesay, B. N.; Ruelas, S.; Yang, J. Y. Solvation Effects on Transition Metal Hydricity. J. Am. Chem. Soc. 2015, 137, 14114.
- (39) Kütt, A.; Selberg, S.; Kaljurand, I.; Tshepelevitsh, S.; Heering, A.; Darnell, A.; Kaupmees, K.; Piirsalu, M.; Leito, I. pK_a values in organic chemistry Making maximum use of the available data. *Tetrahedron Lett.* **2018**, *59*, 3738.
- (40) Kar, S.; Sen, R.; Goeppert, A.; Prakash, G. K. S. Integrative CO₂ Capture and Hydrogenation to Methanol with Reusable Catalyst and Amine: Toward a Carbon Neutral Methanol Economy. *J. Am. Chem. Soc.* **2018**, *140*, 1580.
- (41) Xie, Y.; Hu, P.; Ben-David, Y.; Milstein, D. A Reversible Liquid Organic Hydrogen Carrier System Based on Methanol-Ethylenediamine and Ethylene Urea. *Angew. Chem.* **2019**, *131*, 5159.
- (42) (a) Kortunov, P. V.; Baugh, L. S.; Siskin, M.; Calabro, D. C. In Situ Nuclear Magnetic Resonance Mechanistic Studies of Carbon Dioxide Reactions with Liquid Amines in Mixed Base Systems: The Interplay of Lewis and Brønsted Basicities. *Energy Fuels* **2015**, *29*, 5967. (b) Kortunov, P. V.; Siskin, M.; Baugh, L. S.; Calabro, D. C. In Situ Nuclear Magnetic Resonance Mechanistic Studies of Carbon Dioxide Reactions with Liquid Amines in Non-aqueous Systems: Evidence for the Formation of Carbamic Acids and Zwitterionic Species. *Energy Fuels* **2015**, *29*, 5940.

(43) Pitman, C. L.; Brereton, K. R.; Miller, A. J. M. Aqueous Hydricity of Late Metal Catalysts as a Continuum Tuned by Ligands and the Medium. *J. Am. Chem. Soc.* **2016**, *138*, 2252.

Thermodynamic Analysis of Metal-Ligand Cooperativity of PNP Ru Complexes: Implications for CO₂ Hydrogenation to Methanol and Catalyst Inhibition

Authors: Cheryl L. Mathis, Jackson Geary, Yotam Ardon, Maxwell S. Reese, Mallory A. Philliber, Ryan T. VanderLinden and Caroline T. Saouma*

Affiliation: Department of Chemistry, University of Utah, 315 S. 1400 E., Salt Lake City, Utah 84112, U.S.A.

Section 1: General Considerations	2
Section 2: Preparation & Characterization of Compounds	4
Section 3: pK _a Determinations	13
Section 4: Equilibria with H-X and CO ₂	20
Section 5: Hydrogenations	32
Section 6: NMR Reactions	36
Section 7: References	52

Section 1: General Considerations

Unless noted, all experiments were performed in a nitrogen-filled glovebox or using standard Schlenk techniques. Glassware was oven-dried for 24 hours prior to use. Molecular sieves were activated at 280 °C under vacuum for 48 hours and stored in the glovebox. All non-deuterated solvents were sparged and stored under nitrogen then collected from a Pure Process Technology solvent purification system to remove oxygen and water, stored over activated 3 Å molecular sieves in a glovebox, and tested with ketyl radical before use. NMR solvents were obtained from Cambridge Isotope Labs, subjected to 3 freeze-pump-thaw cycles, and stored under nitrogen in the glovebox over sieves.

Starting materials and reagents: (PNP)Ru-Cl,1 (PNP)Ru+,2 (*PNP)Ru,1 (PNP)Ru-CO₂,³ (PNP)Ru-H,⁴ and RuHCl(PPh₃)₃(CO),⁵ were prepared according to literature procedures. Bone dry CO₂ (99.9%; 10 ppm H₂O) and ultrahigh purity (UHP) H₂ (99.999%; 1 ppm O₂, 1 ppm H₂O, 0.5 ppm THC, 1 ppm CO, 1 ppm CO₂, 5 ppm N₂) gases were purchased from Airgas. Experiments monitoring the reaction of any metal complex outside of the glovebox was conducted using Teflon glassware including sealed cuvettes, J. Young valved NMR tubes for ambient pressure, and PTFE heavy wall precision pressure NMR tubes for pressurized samples. All other reagents were purchased from Sigma Aldrich and used without further purification. The base Ph₃P=CH(CH₃)₂ was prepared according to literature procedures. 6 Conjugate acids of bases were prepared following similar protocol to the literature. Anhydrous formic acid was prepared in the glovebox with vacuum dried sodium formate and stoichiometric HBF₄·Et₂O in diethyl ether, filtered, concentrated in vacuo, and stored over sieves. Initially, the method outlined in the Purification of Laboratory Chemicals,8 gave formic acid with residual water observed by ¹H NMR. Lithium dimethylcarbamate was prepared from a THF solution of Lithium dimethylamide (Sigma Aldrich), freeze-pump-thawed three times, and back filled with 1 atm CO₂. The solution yielded a white viscous solution which was concentrated in vacuo to give a white powder.

Instrumentation: UV-vis measurements were carried out on an Agilent Cary 60 spectrophotometer. Variable temperature and equilibria data were collected using a Q6 sample changer with stirring from Quantum Northwest and a Koolance 440 circulator temperature controller, accurate within 0.1 °C. ¹H NMR spectra were recorded at 400 (Varian/ Agilent Directdrive Inova 400) or 500 MHz (Varian/ Agilent Directdrive VXR-500) and referenced to their respective deuterated solvents. ³¹P spectra were recorded at 122 MHz using a Varian/ Agilent Directdrive Unity 300 or 162 MHz on Inova 400, or 202 MHz on VXR-500 and referenced against H₃PO₄. All NMR analysis is done using Mestrenova. IR spectra were recorded using an Agilent Cary 630 FTIR using KBr pellets. THF solution cell measurements were made using a Bruker Vertex 80v FTIR equipped with a DLaTGS detector. Gas additions were done using a Schlenk line and pressure noted with a mercury monometer or Digivac model 276. In some instances, the pressure was controlled with a JKem Infinity II variable pressure-vacuum controller, which allows us to add pressures of 1 atmosphere in Salt Lake City (elevation: 4,226 feet). Elemental

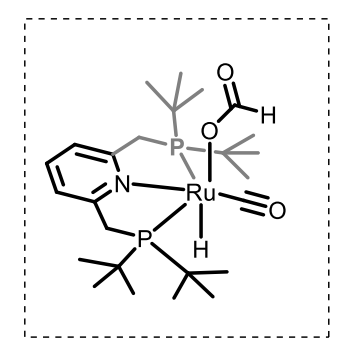
analysis services are provided by Midwest Microlabs, using air-free methods. All plots were created using OriginPro, and instrumental weighing was used for linear fits.

<u>Crystal Structure Determination:</u> Single-crystal X-ray diffraction data was collected on a Nonius KappaCCD diffractometer equipped with Mo Kα radiation (λ = 0.71073 Å) and a BRUKER APEXII CCD. The APEX3 software suite (Ver. 2017.3-0; Bruker AXS, Inc) was used to manage data collection, integration, absorption correction by the Multi-scan method (SADABS)⁹, structure determination via direct methods (SHLEXT)¹⁰ and model refinement (SHELXL).¹¹ Crystals were cooled to 103(2) K throughout data collection. All non-hydrogen atoms were refined anisotropically with all hydrogen atoms ideally constrained to their carriers with the exception of a Ru-H hydride, which was located on the difference map. Platon Squeeze¹² was used to account electron density in regions associated with heavily disordered solvent that could not be modeled. Further details on refinement and disorder can be found in the corresponding .cif file.

Section 2: Preparation & Characterization of Compounds

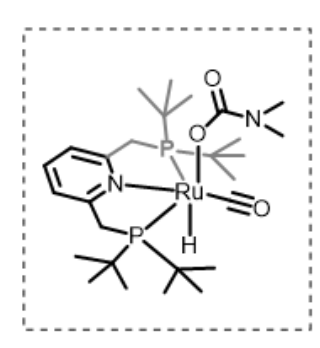
Note: Color identities/changes are indicated throughout with colored spheres in each scheme.

<u>Synthesis of (PNP)Ru-OCHO.</u> We observed that treatment of (*PNP)Ru with anhydrous formic acid gave spectral impurities by NMR spectroscopy and the clean removal of all formic acid was paramount to reliably determine the pK_a for this species. Therefore, in all applications in which (PNP)Ru-OCHO is used for further transformations, it is prepared via sequential gas addition to minimize side products, as described below.



Preparation of (PNP)Ru-OCHO. To an oven dried J. Young valved NMR tube was added (*PNP)Ru (0.008 mmol) and 0.5 mL THF-*d*₈. The tube was treated with one freeze-pump-thaw cycle and refilled with 1 atm of H₂. The reaction was allowed to proceed for 15 minutes while mixing on a rocking platform at 10 rpm, at which time ¹H NMR spectroscopy confirmed complete conversion to (PNP)Ru-H. The NMR tube was subsequently treated with one freeze-pump-thaw cycle to remove unreacted H₂, and was refilled with 1 atm CO₂. The reaction was allowed to

proceed for 15 minutes while mixing on a rocking platform at 10 rpm, at which time ¹H NMR spectroscopy confirmed clean conversion to **(PNP)Ru-CO₂**. The tube was rinsed with diethyl ether (2 x 1 mL) to maximize transfer, and volatiles removed. The residue was solubilized in a minimum of THF, and crystallized via vapor diffusion with pentanes as a counter solvent at -20 °C. The yellow crystals formed were analyzed by ¹H and ³¹P NMR spectroscopy and found to be consistent with previous literature reports. ¹³



Synthesis of (PNP)Ru-DMC. In a glovebox, an oven dried Schlenk tube equipped with a magnetic stir bar was charged with (*PNP)Ru (0.0095 mmol, 5 mg) in 0.5 mL THF and finally dimethylammonium dimethylcarbamate (0.0157 mmol, 1.3 mg). The sample immediately turned yellow, and was concentrated *in vacuo*. The yellow residue remaining was washed with pentanes, filtered over celite, resolubilized in THF, and concentrated *in vacuo* to yield a yellow-orange powder. Yield: 5.2 mg, 0.0085 mmol, 89%. Crystals suitable for X-ray diffraction were grown from

THF and vapor diffusion of pentanes at -20 °C. ^{31}P (THF- d_8 , 500 MHz, ppm): 91.92 (s). ^{1}H (THF- d_8 , 500 MHz, ppm): -16.70 (1H, t, J_{HP} = 19.4 Hz, Ru-H), 1.25 (18H, t, J_{HP} = 6.2 Hz, -C(C H_3)₃), 1.34 (18H, t, J_{HP} = 6.4 Hz, -C(C H_3)₃), 2.60 (6H, s, Ru-OC(O)N(C H_3)₂), 3.45 (2H, dt, J_{HH} = 16.2 Hz, J_{HP} = 3.7 Hz, -CH H_7), 4.03 (2H, dt, J_{HH} = 16.2 Hz, J_{HP} = 3.3 Hz, -C H_7), 7.25 (2H, d, J_{HH} = 7.7 Hz, Py, 7.54 (1H, t, J_{HH} = 7.7 Hz, Py). ^{13}C (THF- d_8 , 500 MHz, ppm): 209.76, 165.03, 163.37, 137.72, 120.12, 38.16, 37.57, 37.07, 35.60, 30.01, 26.37. IR (THF solution): 1913 cm⁻¹(V_{CO}), 1591 cm⁻¹ (V_{OCO}). IR (KBr): 2067 cm⁻¹ (V_{RuH}),

1911 cm⁻¹(v_{CO}), 1587 cm⁻¹ (v_{COO}). **UV-vis (THF)** λ_{max} , nm (ϵ , M⁻¹ cm⁻¹): 595 (6), 330 (640), 275 (1400, sh), 255 (1725). **Anal Calcd for (C**₂₇**H**₅₀**N**₂**O**₃**P**₂**Ru**): C, 52.8; H, 8.2; N, 4.6. Found: C, 52.7; H, 8.5; N, 3.8.

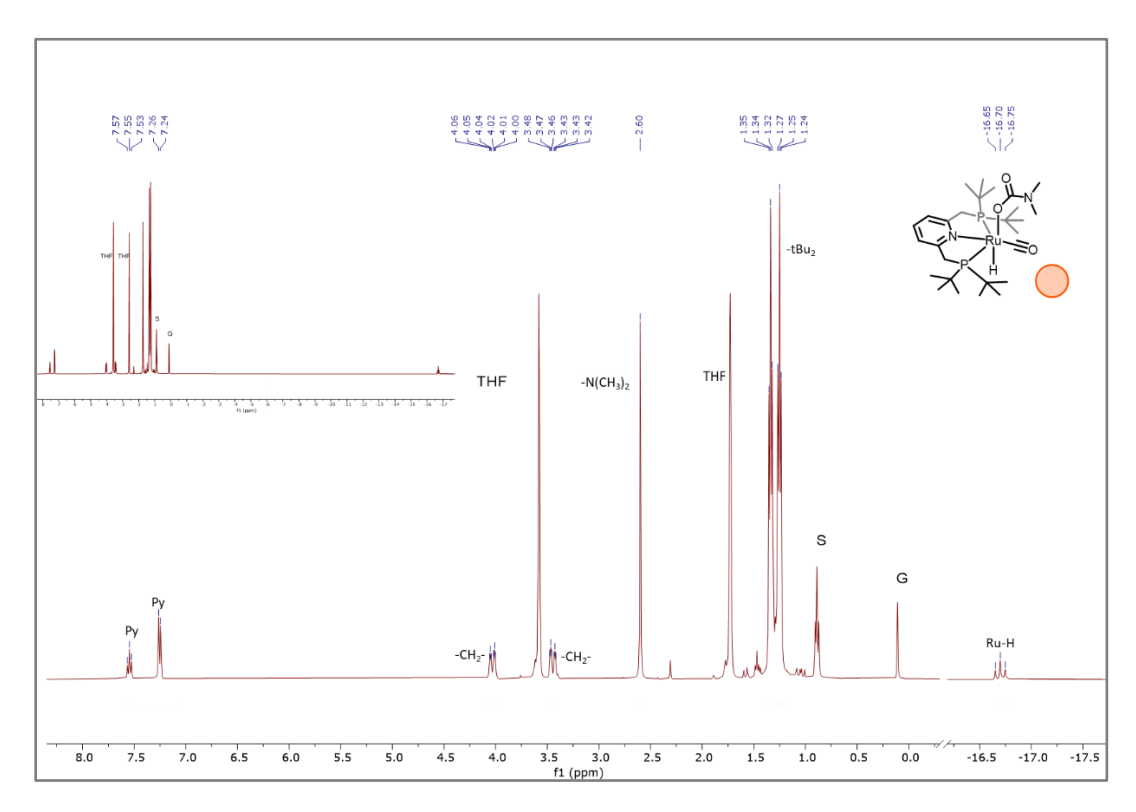


Figure S1: ¹H NMR (400 MHz, 293 K, THF-*d*₈) spectrum of **(PNP)Ru-DMC.** G represents grease. Solvent impurities 'S' are from pentanes. **Insert:** Full spectrum showing no other hydride peaks.

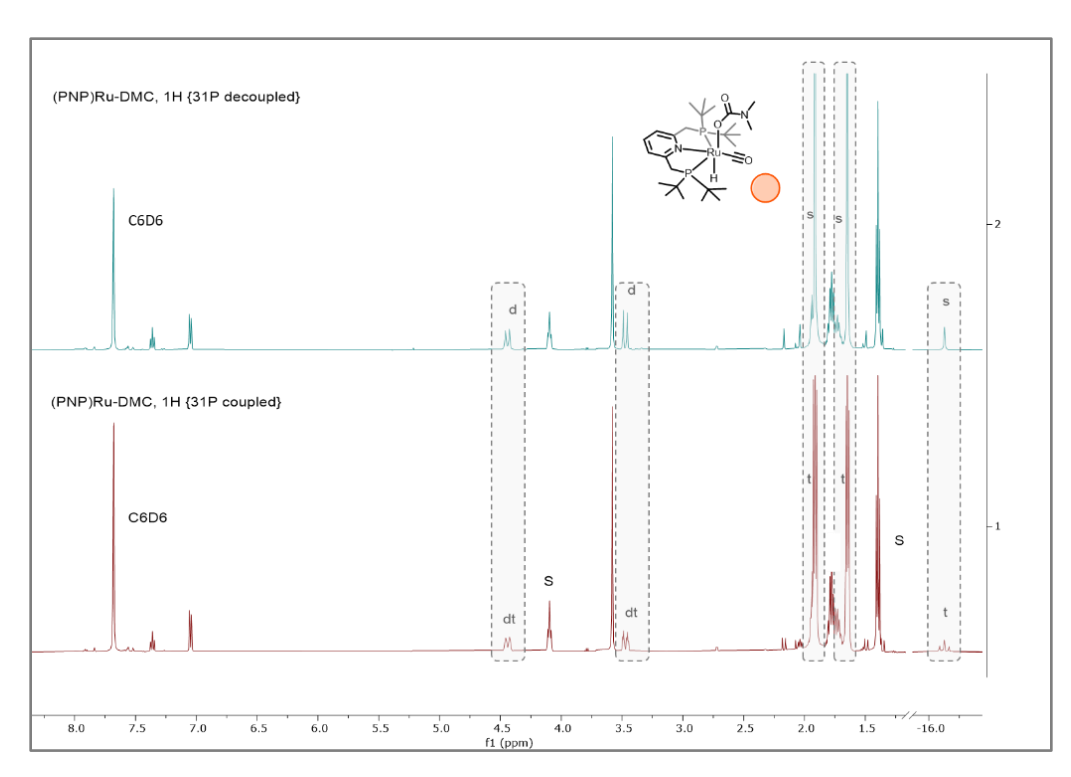


Figure S2: (top): $^{1}H\{^{31}P\}$ and **(bottom):** ^{1}H NMR spectrum of **(PNP)Ru-DMC** (500 MHz, 293 K, C₆D₆). Resonances with changes are noted by splitting notation. Solvent impurities 'S' are from pentanes and THF.

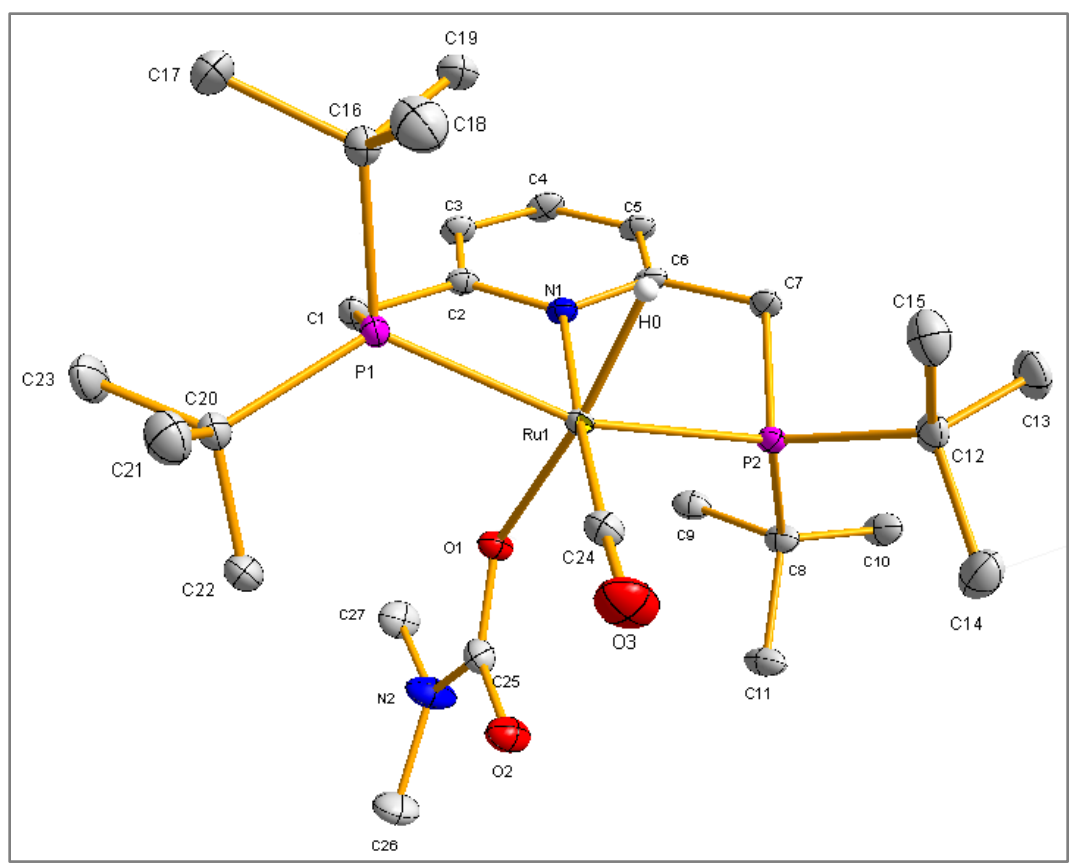


Figure S3: Thermal ellipsoid (50%) rendition of (PNP)Ru-DMC.

Table S1: Select bond distances and angles for (PNP)Ru-DMC.

A ₁ -A ₂	Bond Length (Å)	A ₁ -A ₂ -A ₃	Bond Angle (°)
Ru ₁ -P ₁	2.3383(5)	N ₁ -Ru ₁ -C ₂₄	174.21(6)
Ru ₁ -P ₂	2.3462(5)	N ₁ -Ru ₁ -P ₁	80.39(3)
Ru ₁ -N ₁	2.145(1)	N ₁ -Ru ₁ -P ₂	81.05(3)
Ru ₁ -O ₁	2.205(1)	N ₁ -Ru ₁ -O ₁	83.20(4)
Ru ₁ -C ₂₄	1.835(2)		

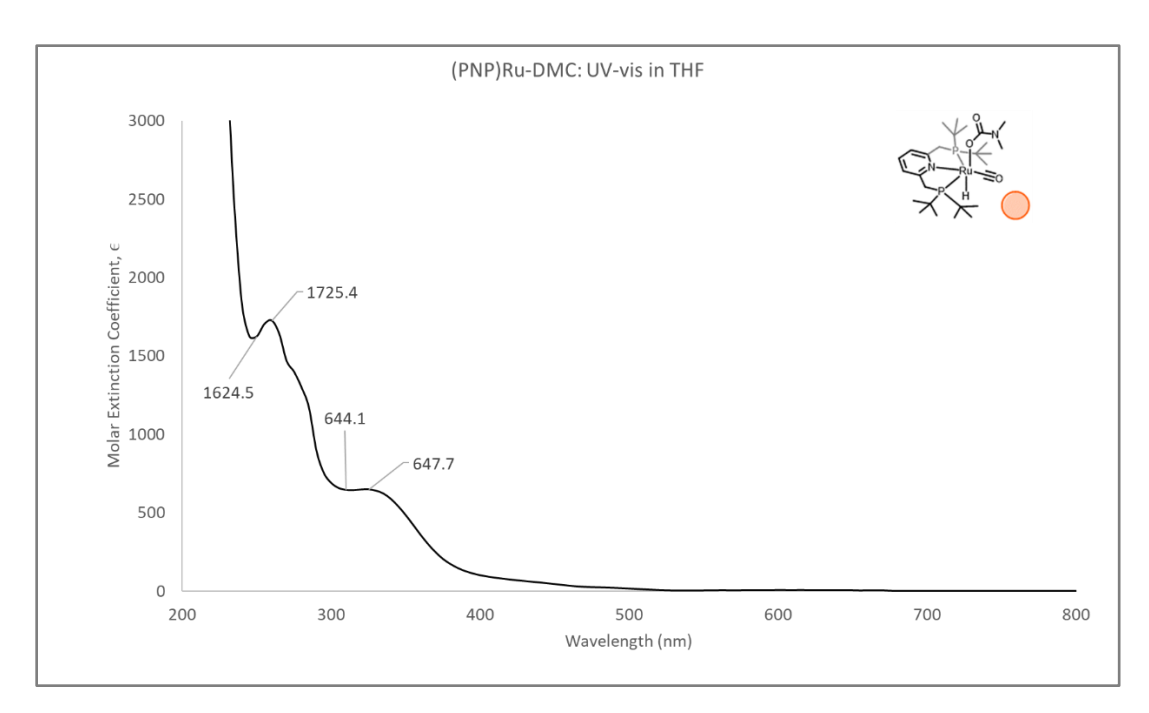
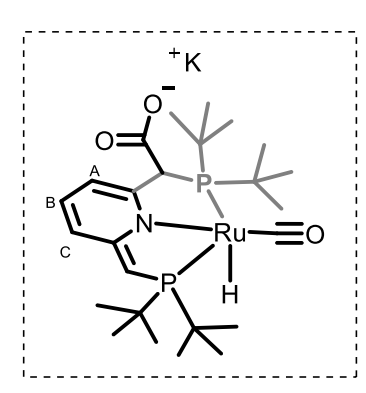


Figure S4: UV-vis spectrum of (PNP)Ru-DMC in THF, 200-800 nm.



Synthesis of [K][(*PNP)Ru-CO2]. To an oven dried Teflon Schlenk tube equipped with a magnetic stir bar was added **(*PNP)Ru** (0.056 mmol, 30 mg) in 1 mL THF (0.05 M). The tube was transferred to the Schlenk line and was charged with 1 atm CO2. The stirring solution turned pale yellow from dark green and was subjected to two freeze-pump-thaw cycles to remove excess CO2 from the headspace and solution. The flask was then filled with nitrogen and returned to the glovebox. At this time, an aliquot containing 0.008 mmol was removed for use in another application. A solution of KHMDS (0.05 mmol, 9.2 mg)

in 1 mL THF (0.05 M) was added to the remaining solution and the solution became orange. Crystals were successfully grown via vapor diffusion with diethyl ether as a counter solvent at -20 °C, yielding 25 mg of the desired product (0.041 mmol, 85%). The orange crystals formed were analyzed by 1 H and 31 P NMR spectroscopy; this compound was found to be moderately stable when exposed to vacuum but unstable when in THF solution for prolonged periods at room temperature. This instability is solvent dependent, as benzene confers superior stability at room temperature; NMR data for both THF- d_8 and C₆D₆ have been included for reference. 31 P (1 HF- 1

d, J_{HP} = 12.4 Hz, $-C(CH_3)_3$), 1.43 (18H, t, J_{HP} = 11.6 Hz, $-C(CH_3)_3$), 1.57 (9H, d, J_{HP} = 12.9 Hz, $-C(CH_3)_3$), 3.73 (1H, s, =CH-), 3.96 (1H, d, J_{HH} = 6.6 Hz, -CH-), 5.46 (1H, d, J_{HH} = 6.2 Hz, Py_A), 6.12 (1H, d, J_{HH} = 8.9 Hz, Py_B), 6.38 (1H, t, J_{HH} = 7.6 Hz, Py_C). ¹³C (C₆D₆, 500 MHz, ppm): 211.30, 180.41, 168.09, 157.91, 131.49, 112.14, 95.39, 68.58, 68.20, 67.85, 62.24, 38.30, 36.37, 36.05, 35.81, 25.83, 16.23. IR (THF solution): 2067 cm⁻¹ (V_{CRUH}), 1886 cm⁻¹(V_{CO}), 1600 cm⁻¹ (V_{COO}). UV-vis (THF) λ_{max} , nm (ε , M_{C} cm⁻¹): 595 (202), 515 (488, sh), 480 (816, sh), 445 (985). The limited stability of this species precludes our ability to obtain satisfactory elemental analysis.

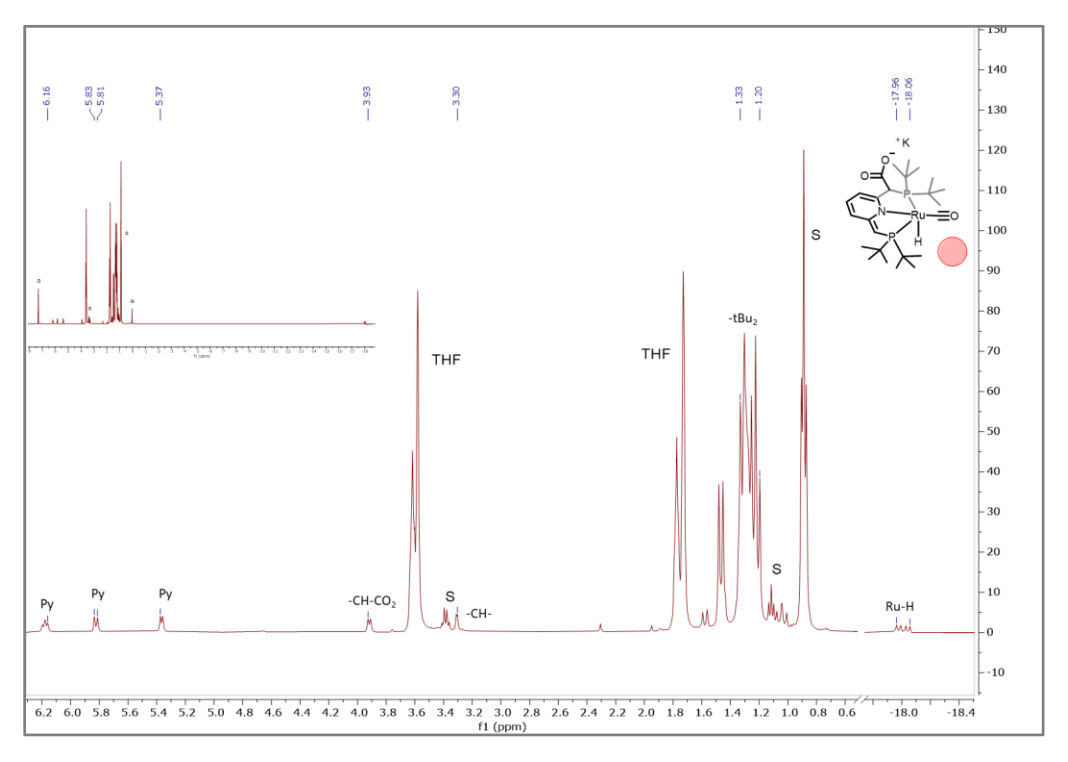


Figure S5: ¹H NMR spectrum (400 MHz, 293 K, THF-*d*₈) of **[K][(*PNP)Ru-CO₂]**. Solvent impurities 'S' are from pentanes and diethyl ether. **Inset**: Full spectrum.

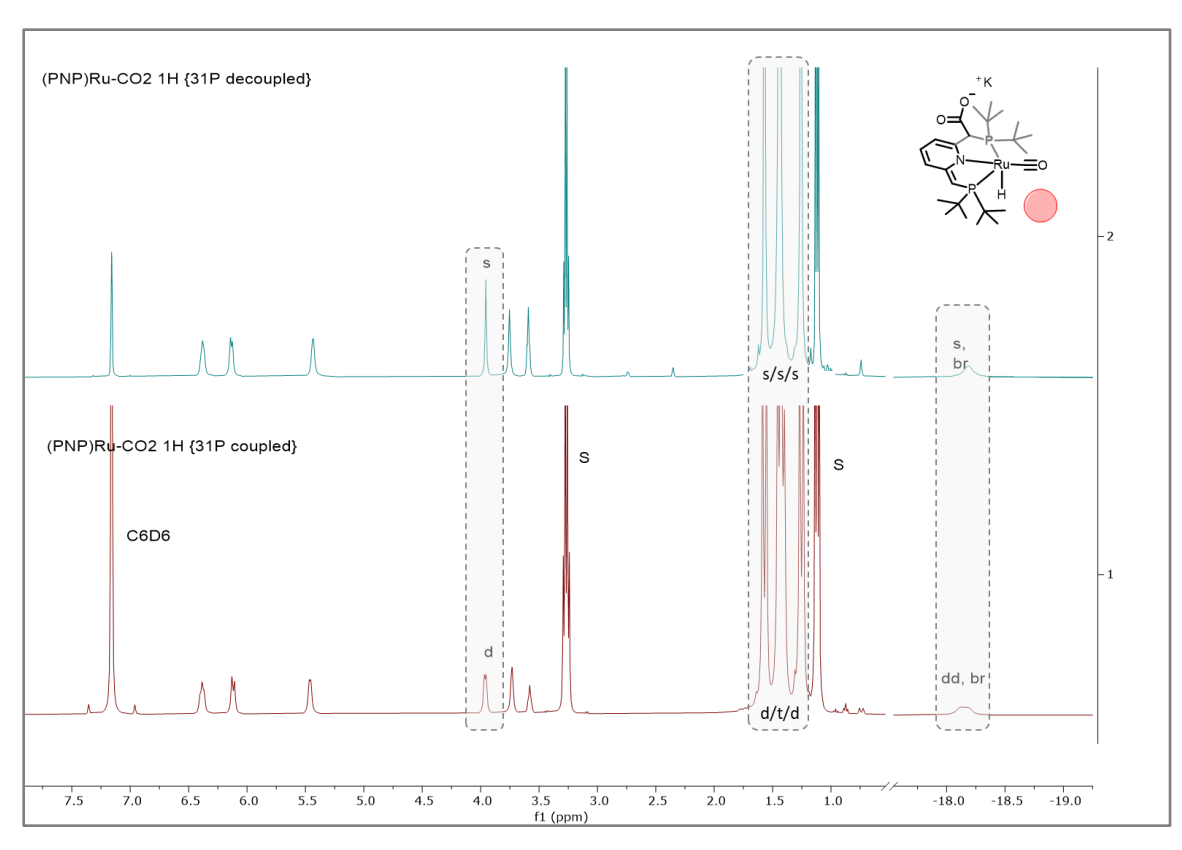


Figure S6: (top): 1 H{ 31 P} and **(bottom):** 1 H NMR spectrum of **[K][(*PNP)Ru-CO_2]** (500 MHz, 293 K, C₆D₆). Resonances with changes are noted by splitting notation. Solvent impurities 'S' are from pentanes and THF.

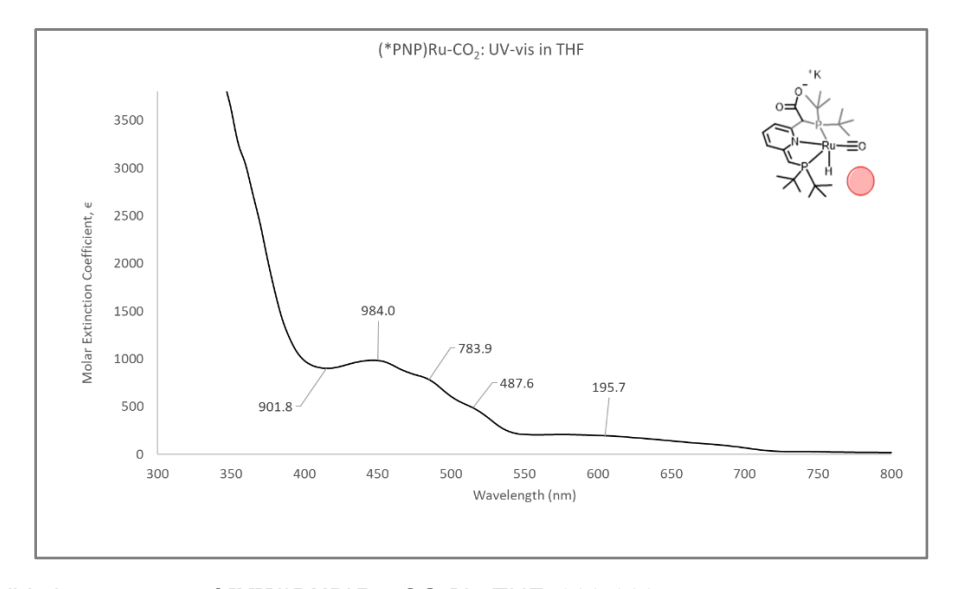


Figure S7: UV-vis spectrum of [K][(*PNP)Ru-CO₂] in THF, 300-800 nm.

Table S2: Select bond distances and angles for [K][(*PNP)Ru-CO₂].

A ₁ -A ₂	Bond Length (Å)	A ₁ -A ₂ -A ₃	Bond Angle (°)
Ru Coordinating:			
Ru ₂ -P ₃	2.336(1)	N ₂ -Ru ₂ -C ₅₀	175.9(2)
Ru ₂ -P ₄	2.344(1)	N ₂ -Ru ₂ -P ₃	80.63(12)
Ru ₂ -N ₂	2.118(4)	N ₂ -Ru ₂ -P ₄	80.44(12)
Ru ₂ -O ₅	2.302(3)	N ₂ -Ru ₂ -O ₅	76.58(15)
Ru ₂ -C ₅₀	1.847(5)		
Ligand:			
P ₃ -C ₃₃	1.766(6)		
C ₃₃ -C ₃₂	1.374(7)		
P4-C27	1.858(5)		
C ₂₇ -C ₂₈	1.508(8)		
Carboxylate:			
C ₂₇ -C ₂₆	1.555(7)	O ₄ -C ₂₆ -O ₅	125.6(5)
C ₂₆ -O ₄	1.263(6)		
C ₂₆ -O ₅	1.240(6)		

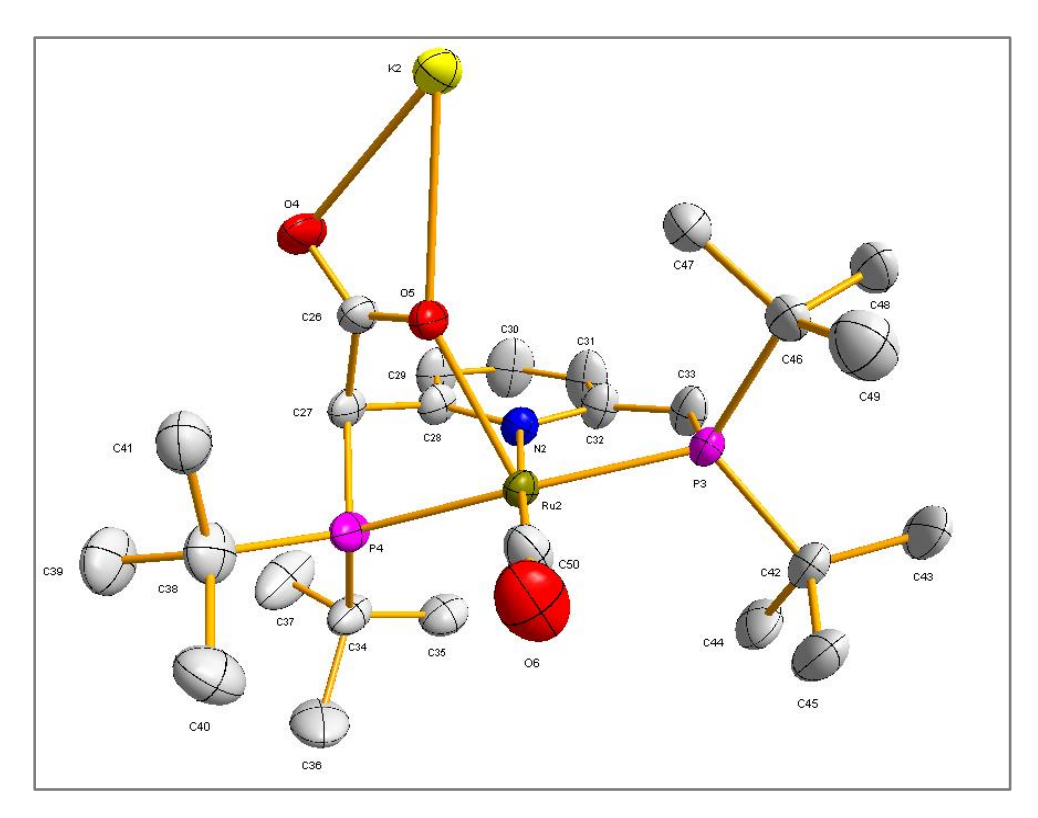


Figure S8: Thermal ellipsoid plot (50%) of one half **[K][(*PNP)Ru-CO₂]**. The K and solvent are removed for clarity.

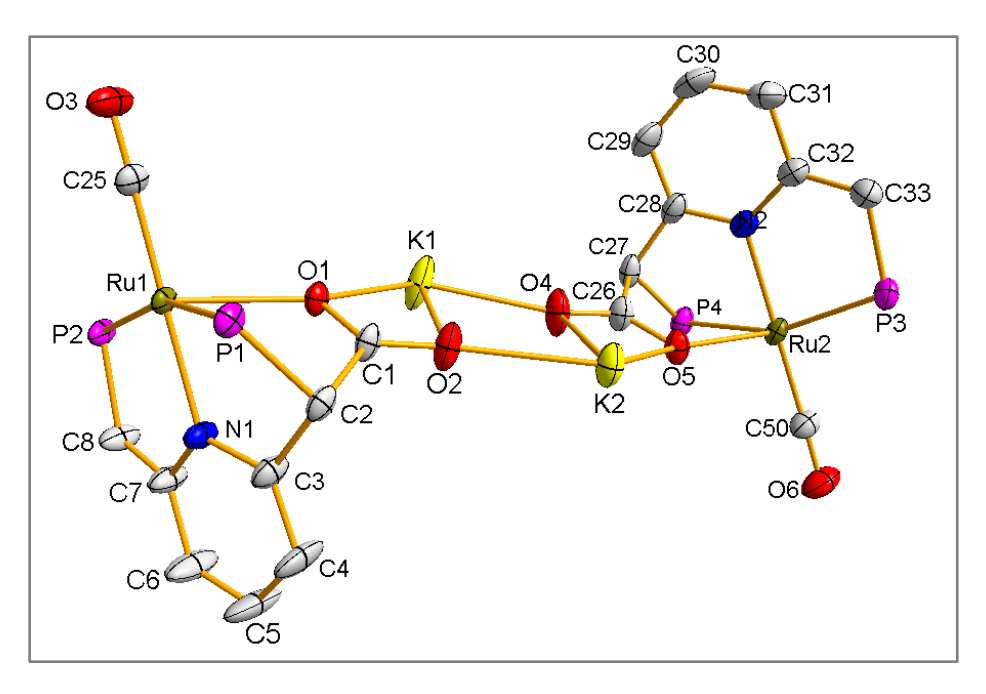
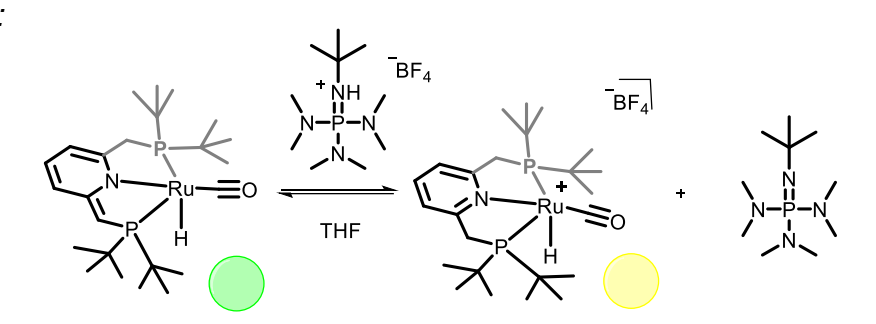


Figure S9: Thermal ellipsoid plot of **[K][(*PNP)Ru-CO₂]**, showing the diamond core. For clarity, t Bu groups, and solvent molecules are omitted. Each K is coordinated to one Et₂O and one THF molecule.

Section 3: pK_a Determinations

<u>pK_a Determination of (PNP)Ru⁺ (K₃)</u>. A 0.69 mM THF solution of (PNP)Ru⁺ was added to a septum-sealed quartz cuvette (Starna Cells, 170-2700 nm range) equipped with a septum cap. The UV-vis spectrometer was zeroed using THF from the same source as the sample, and an initial spectrum of the complex recorded. Using a micro-syringe, 13 μL (0.000137 mmol, 0.5 equivalents) of a 0.0107 M solution of t-Butylimino-tri(pyrrolidino)phosphorene · tetrafluoroboric acid (BTPP-HBF₄) was added to (PNP)Ru⁺ and allowed to stir at 1200 rpm. Additions were found to equilibrate quickly and were measured 30 seconds after introduction of the acid solution. The diagnostic absorbance of the product, (*PNP)Ru, at 595 nm was used to monitor reaction progress. Using the mass balance equations below, 14 K_a was determined graphically by plotting the equilibrium [(PNP)Ru⁺][BTPP]/[(*PNP)Ru] against [BTPP-HBF₄], yielding an average pK_a of 20.7 ± 0.2. This value is determined from the average of two trials.

Mass Balance:



Using the Beer-Lambert's Law (Eq. 1) and known molar extinction coefficients (ϵ) at 595 nm for the clean reaction of Ru* to RuH, we can use a ratio of absorbances to determine the relative concentrations of each species as follows:

$$A = \epsilon lc$$
 Eq. 1

At time 0, the absorbance at 595 nm is completely derived from Ru^* ($Ru^* = (*PNP)Ru$) (Eq. 2):

$$A_o = \epsilon_{Ru*} \cdot [Ru^*]_o$$
 Eq. 2

The absorbance at any time, x, can be attributed to the combined absorbances of both species, Ru^* and RuH ($RuH = (PNP)Ru^*$):

$$A_x = (\epsilon_{Ru} \cdot [Ru^*]_x) + (\epsilon_{RuH} \cdot [RuH]_x)$$
 Eq. 3

Similarly, when all of Ru* has been transformed into RuH, the final absorbance is completely derived from RuH (Eq. 4):

$$A_f = \epsilon_{Ru} \cdot [RuH]_f$$
 Eq. 4

Knowing that the cuvette is a closed system, we can also assume that the initial concentration of Ru* is equivalent to the final concentration of RuH, and by extension, the mixture of the two species at any time in between, x (Eq. 5):

$$[RuH]_f = [Ru^*]_o = [RuH]_x + [Ru^*]_x$$
 Eq. 5

Measuring the UV-Vis absorbance allows us to determine a ratio of [RuH]:[Ru*] at any time, x (Eq. 6):

$$\frac{[RuH]_x}{[Ru^*]_x} = \frac{(A_x - A_o)}{(A_f - A_x)}$$
 Eq. 6

This ratio can be leveraged to yield the concentration of RuH as a variable, B (Eq. 7):

$$[RuH]_x = \frac{(A_x - A_0)}{(A_f - A_x)} \cdot [Ru^*]_x = B$$
 Eq. 7

By substitution of $[Ru^*]_x$ with a form of Equation 5, we arrive at Eq. 8:

$$[RuH]_x = B \cdot ([Ru^*]_o - [RuH]_x)$$
 Eq. 8

Equation 8 can be separated into two terms, and resolved for $[RuH]_x$ to give Eq. 9:

$$[RuH]_x = \frac{B \cdot [Ru^*]_0}{1+R} \qquad \text{Eq. 9}$$

For pK_a determination, we want to create a relationship between the acid or base added and the ruthenium complex in question. Because we start with a sample of pure Ru*, the loss of signal can be related to formation of the conjugate acid or base. An example is provided in the case of an added acid (HB), where we can infer that protonated [RuH]_x must equal the resulting conjugate base, [B]_x in Eq. 10 and 11:

$$[HB]_x = [HB]_{tot} - [B]_x$$
 Eq. 10

$$[HB]_x = [HB]_{tot} - [RuH]_x$$
Eq. 11

Using an equilibrium expression, and knowing the [B]x and [HB]x, we can apply Eq 12:

$$K = \frac{[Products]}{[Reactants]} = \frac{[RuH]_x \cdot [B]_x}{[Ru^*]_x \cdot [HB]_x}$$
 Eq. 12

A plot of $([RuH]_x[B]_x)/[Ru^*]_x$ vs. $[BH]_x$ yields a linear system with a slope of K, and finally the pK_a of RuH is determined using the known pK_a of the added acid in THF (Eq. 13):

$$pK_{a, RuH} = pK_{a, HB} - log(K_a)$$
 Eq. 13

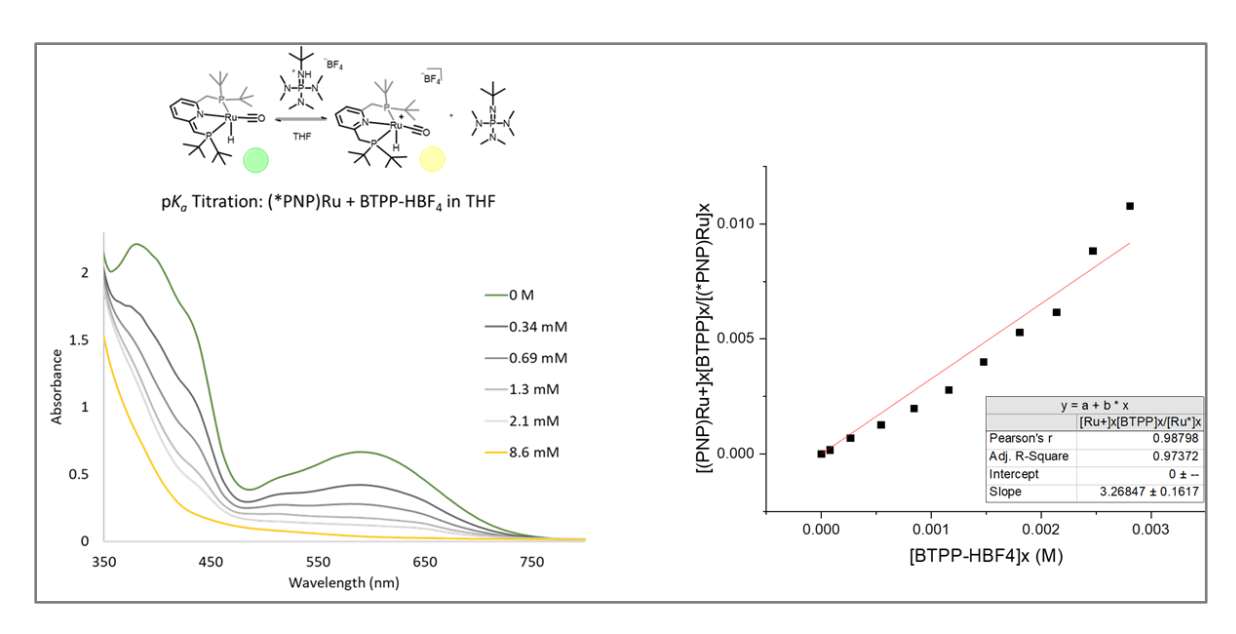


Figure S10: (left): Stacked UV-vis spectra for the titration of (*PNP)Ru with BTTP-HBF₄ to give (PNP)Ru⁺. (right): Plot of [(PNP)Ru⁺($^{+}$ BF₄)] x [BTPP]/ [(*PNP)Ru)] vs [BTPP-HBF₄]. Each point corresponds to the addition of $\frac{1}{2}$ equivalents respective to (*PNP)Ru.

<u>pK_a Determination of (PNP)Ru-CO₂ (K₄)</u>. Unlike the straightforward pK_a determination for (PNP)Ru⁺, the titrations of (*PNP)Ru-CO₂ suffered from even minor air exposure and as stated in Section 2, is also unstable at room temperature in THF. Below is a comparison of two methods to determine the pK_a for (PNP)Ru-CO₂: one which uses crystalline material dissolved in THF and immediately titrated, and a second which makes (*PNP)Ru-CO₂ in situ and is immediately titrated.

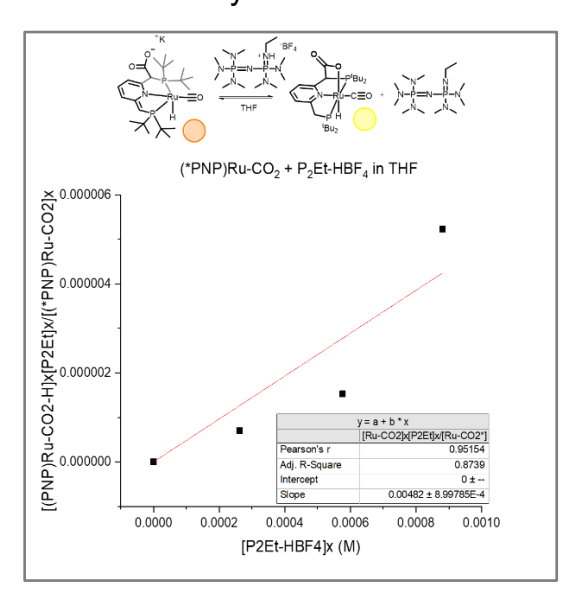


Figure S11: pK_a titration of **[K]**[(*PNP)Ru-CO₂] with $P_2Et \cdot HBF_4$ in THF. The instability of **[K]**[(*PNP)Ru-CO₂] in THF presented challenges for pK_a determination in THF – initial work utilized prefabricated **[K]**[(*PNP)Ru-CO₂] crystals and titrated in the acid, $P_2Et \cdot BF_4$. However, even after replication in triplicate, error was significant: 26.4 ± 1.7.

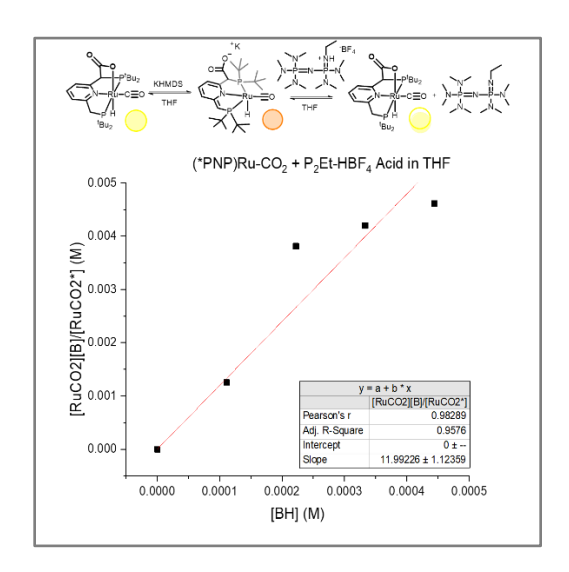


Figure S12: In situ p K_a titration of **[K][(*PNP)Ru-CO₂]** with P₂Et·HBF₄ in THF. **[K][(*PNP)Ru-CO₂]** is first generated in the cuvette with the addition of 1 Equiv. KHMDS. The solution is immediately titrated with P₂Et·HBF₄ to return to **(PNP)Ru-CO₂** (Figure S13). Using this method, the p K_a is 24.6 ± 0.4.

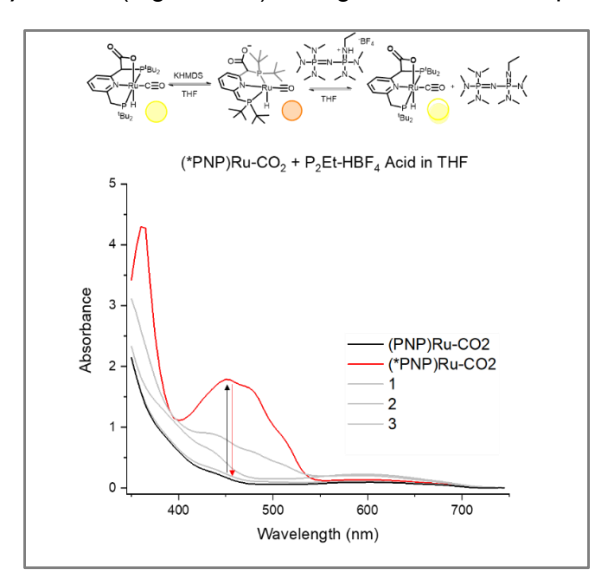


Figure S13: In situ p K_a titration of [K][(*PNP)Ru-CO₂] with P₂Et·HBF₄ in THF corresponding to Figure S12. The black trace corresponds to (PNP)Ru-CO₂, which upon treatment with KHMDS forms the red trace, [K][(*PNP)Ru-CO₂]. Titration with P₂Et-HBF₄ acid returns all the [K][(*PNP)Ru-CO₂] fully to (PNP)Ru-CO₂.

<u>pK_a Determination of (PNP)</u>: Titration of the ligand proceeded analogously to that of the various ruthenium complexes. A 0.32 mM solution of the ligand in THF (4 mL) was loaded into a quartz cuvette with a septum cap. A 14 mM solution of (Ph)₃P=CH(CH₃)₂ was added via micro syringe in 10 μ L increments, corresponding to ~ 1 equivalent per addition. The clear colorless ligand transformed into a vibrant yellow upon treatment with the base, and reaction progress was monitored using the change in absorbance at 380 nm. The

absorption that corresponds to (Li)(PNP) was determined by treatment of the ligand with 1 equiv of ⁿBuLi.

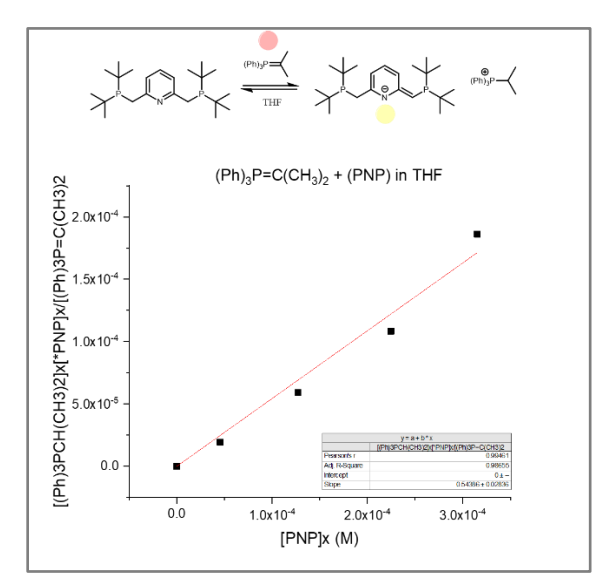


Figure S14: Titration of (PNP) with Ph₃P=CH(Me)₂ in THF.

pK_a **Determination for atypical cases involving ligand dissociation (K**_{5,X}): For the pK_a of **(PNP)Ru-X**, where X = Cl, DMC, OCHO, the equilibrium is technically a proton transfer followed by ligand loss and can't give a 'true' pK_a. By combining the titration equilibrium constant ($K_{8,X}$) with an estimating the equilibrium for the loss of X⁻, we can assign a lower-limit to the pK_a of **(PNP)Ru-X** to be obtained as outlined in the main text. We assume a lower-limit K_{7x} value of 100.

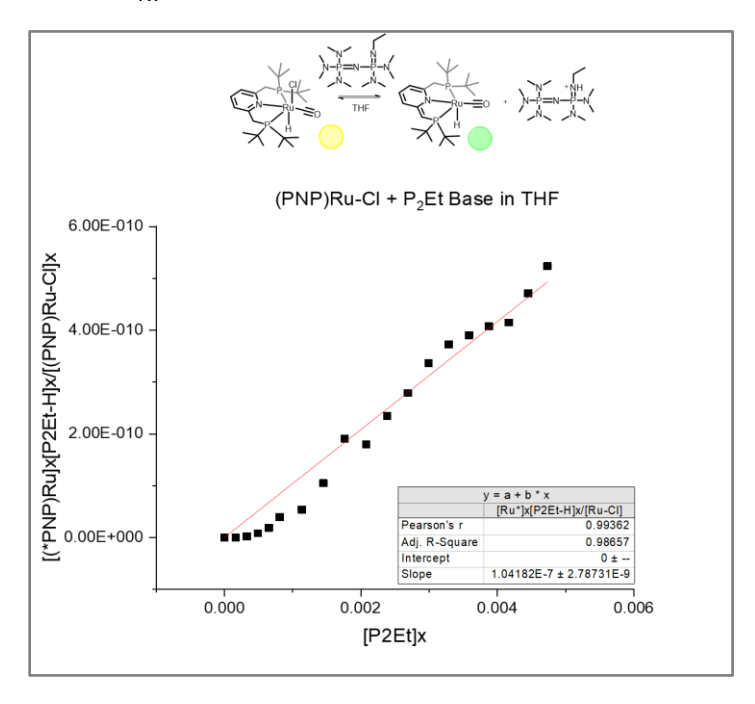


Figure S15: Equilibria of **(PNP)Ru-CI** with P₂Et in THF ($K_{8,CI}$).

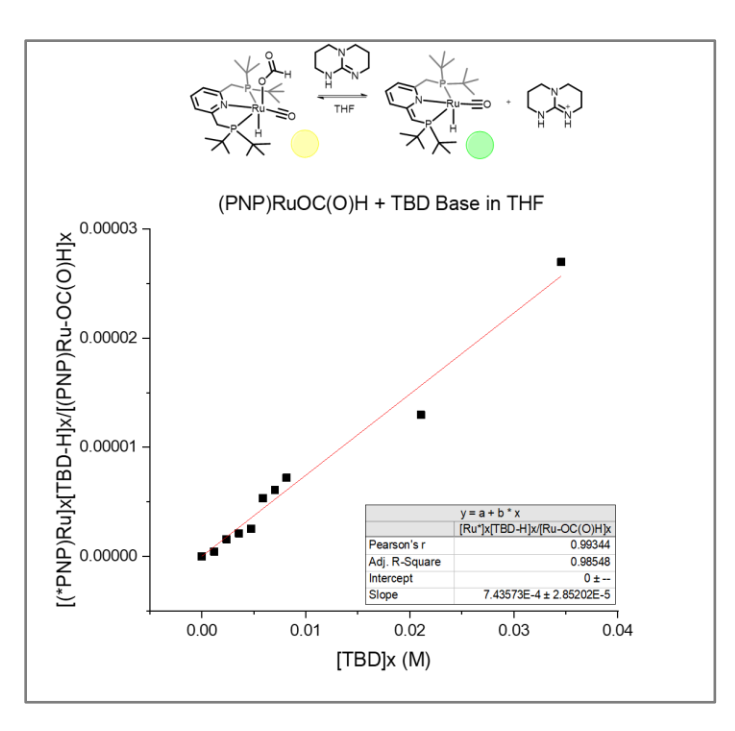


Figure S16: Equilibria of **(PNP)Ru-OCHO** with TBD in THF ($K_{8,OCHO}$).

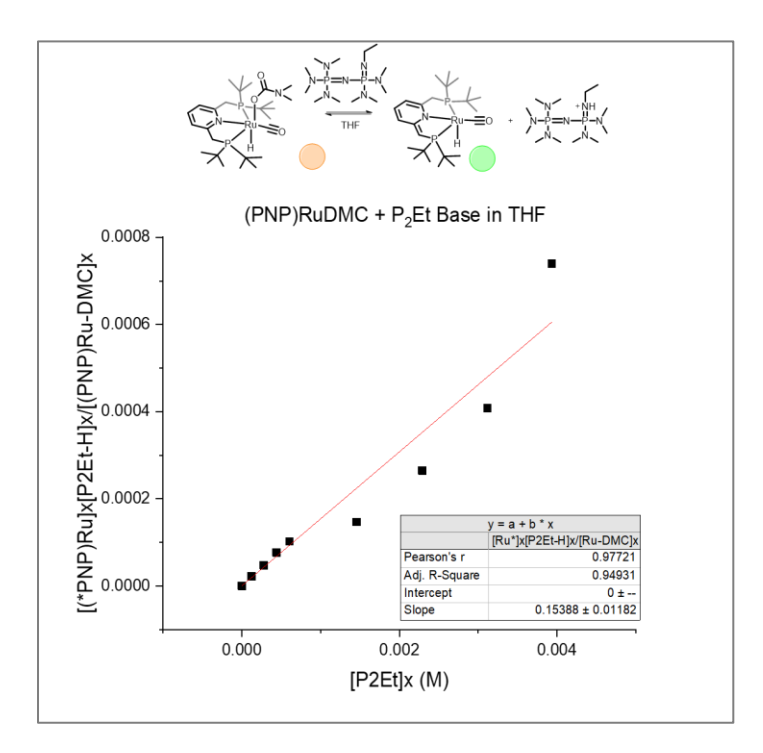


Figure S17: Equilibria of (PNP)Ru-DMC with P_2Et in THF ($K_{8,DMC}$).

Table S3: Summary of pK_a values. Errors are from duplicate runs.

Ru Identity	Titrant Identity (pK _a of conjugate acid, THF)	Ru pKa, THF
(PNP)Ru-CI	P ₂ Et (25.3) ¹⁵	> 33.9 ± 0.4
(PNP)Ru⁺	BTPP·HBF ₄ (20.2) ¹⁵	20.7 ± 0.2
(PNP)Ru-OCHO	TBD (21.0) ¹⁶	> 25.4 ± 0.5
(PNP)Ru-CO ₂	P ₂ Et (25.3)	24.6 ± 0.4
(PNP)Ru-DMC	P ₂ Et (25.3)	> 32.7 ± 0.5
PNP Ligand	Ph ₃ P=CH(CH ₃) ₂ (28.9) ¹⁷	28.6 ± 0.1

Section 4: Equilibria with H-X and CO₂

Equilibrium of (*PNP)Ru with formic acid (К1,осно). 4 mL of 0.68 mM solution of **(*PNP)Ru** in THF were added to five identical teflon cuvettes or oven-dried scintillation vials inside of the glovebox. The first sample is untouched as a reference; to the remaining samples was added increasing concentrations of anhydrous formic acid (final concentrations: 0.32 mM, 0.68 mM, 1.2 mM, and 2.4 mM). These samples were capped and allowed to stir at room temperature for 12 hours before collecting a UV-vis spectrum to ensure that equilibrium is achieved. As for pK_a measurements, the absorbance at 595 nm was used to monitor progress. Error corresponds to the standard deviation from multiple trials which is then propagated.

Samples used for van't Hoff analysis were heated or cooled to provide VT equilibrium speciation data in Teflon sealed quartz cuvettes; samples were allowed to temperature equilibrate for one hour prior to data collection at every temperature point.

Concentration dependence was anticipated based on the K_{eq} expressions for MeOH, H₂O, and formic acid having units of M⁻¹. Using the experimentally derived equilibrium constant, samples were diluted to decrease the substrate concentration and correspondingly shift the ratio of ruthenium species. An example, formic acid, is detailed below:

$$K = \frac{[Products]}{[Reactants]} = \frac{[RuOCHO]_x}{[Ru^*]_x \cdot [Formic\ Acid]_x}$$

If K_{eq} (Formic Acid) is 354.8 and the desired ratio of [RuOCHO] to [Ru*] is 2:1 for a 0.0025 M sample, we can determine the amount of formic acid needed for this transformation by rearrangement:

$$[Formic\ Acid]_x = \frac{[RuOCHO]_x}{[Ru^*]_x} \cdot K$$

In this first case, $[FA]_x$ should equal 0.0056 M. To invert the ratio of $[RuOCHO]_x:[Ru^*]_x$ to 1:2, we dilute the sample in agreement with $M_1V_1 = M_2V_2$ to yield a final $[FA]_x$ of 0.0014 M.

In contrast, the K_{eq} expression for the reaction of (*PNP)Ru with DMC does not suggest concentration dependence, and this is reflected in the absence of change after dilution as shown below.

Equilibrium of (*PNP)Ru with (DMA-H)(DMC) (K_{1,DMC}). This equilibrium was determined analogously as that described above, using different concentrations of substrate to correspond to the different equilibrium constant.

Equilibrium of (*PNP)Ru with MeOH (K1,0Me). This equilibrium was determined analogously as that described above, using different concentrations of substrate to correspond to the different equilibrium constant.

Equilibrium of (*PNP)Ru with H₂O (K_{1,OH}). This equilibrium was determined analogously as that described above, using different concentrations of substrate to correspond to the different equilibrium constant.

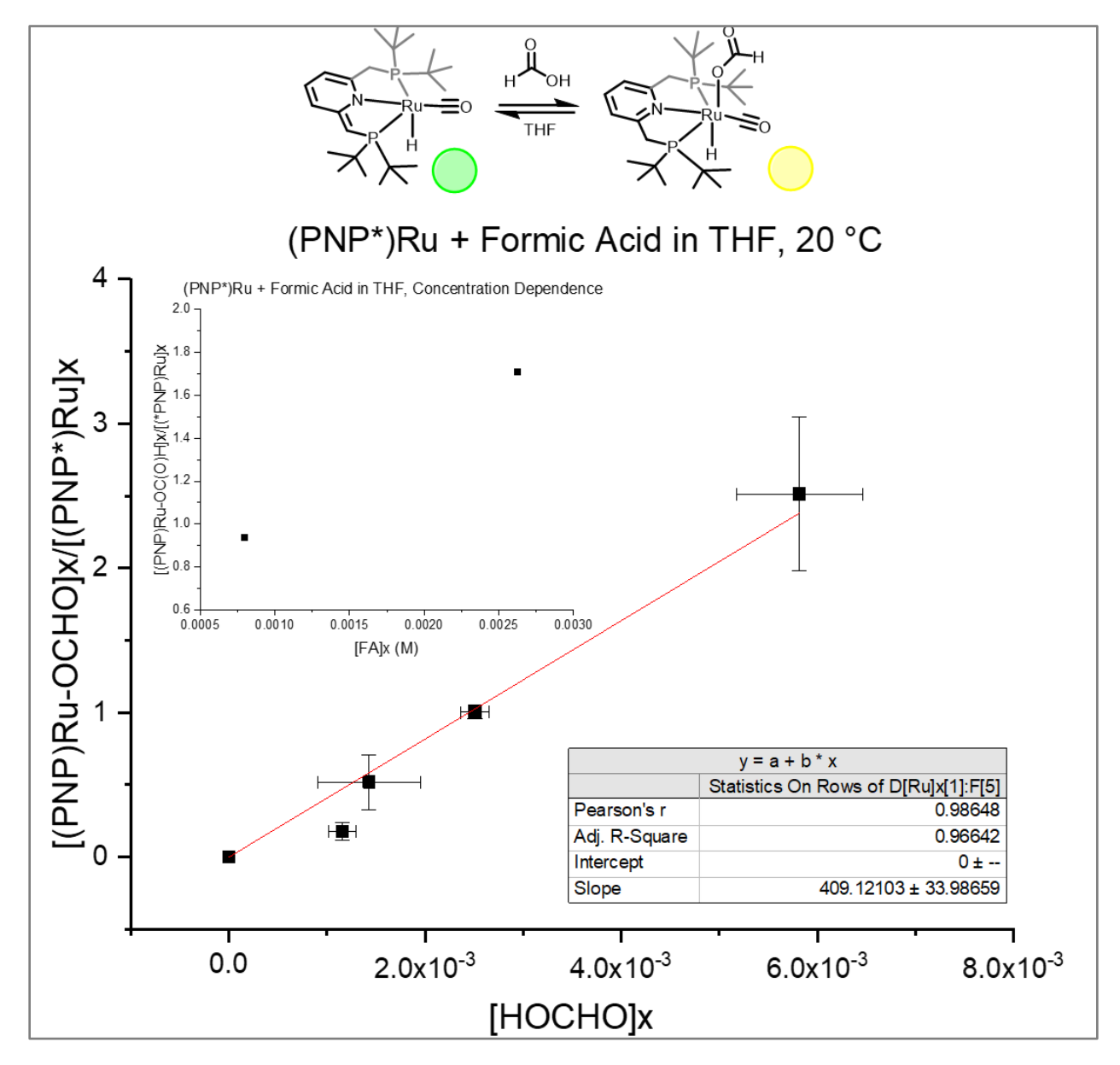


Figure S18: Plot of [(PNP)Ru-OCHO)]/[(*PNP)Ru] versus [formic acid] from multiple trials. Concentrations are derived from initial concentrations and the absorbance at 595 nm, and represent equilibrium concentrations. Data collected at 293 K in THF. **Inset:** Shift in [(PNP)Ru-OCHO)]/[(*PNP)Ru] upon diluting a sample.

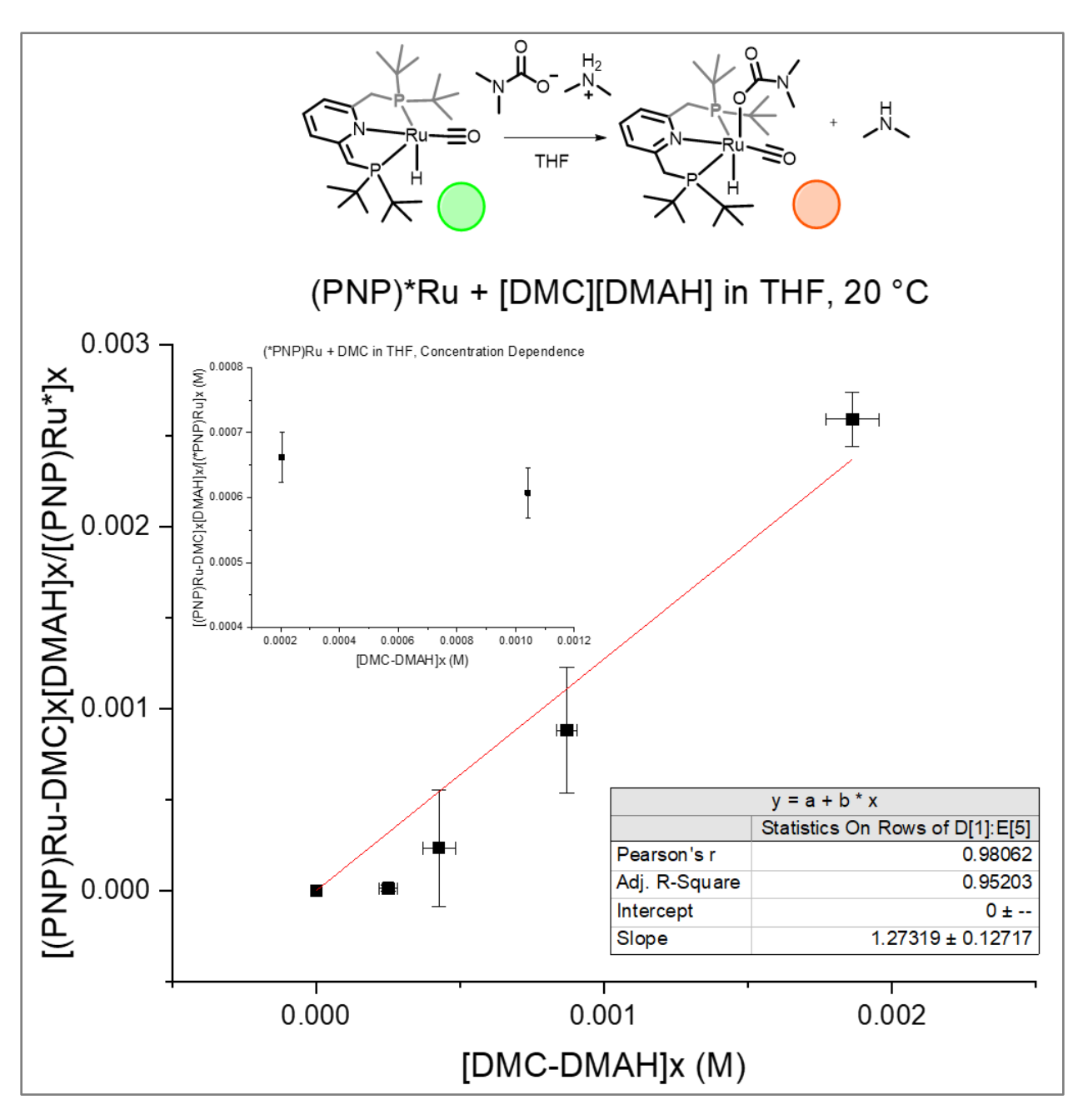


Figure S19: Plot of [(PNP)Ru-DMC)][(DMA)]/[(*PNP)Ru] versus [(DMA-H)(DMC)]. Errors correspond to the standard deviation from two trials. Concentrations are derived from initial concentrations and the absorbance at 595 nm, and represent equilibrium concentrations. Data collected at 293 K in THF. **Inset:** Diluting a sample does not result in a shift in equilibrium.

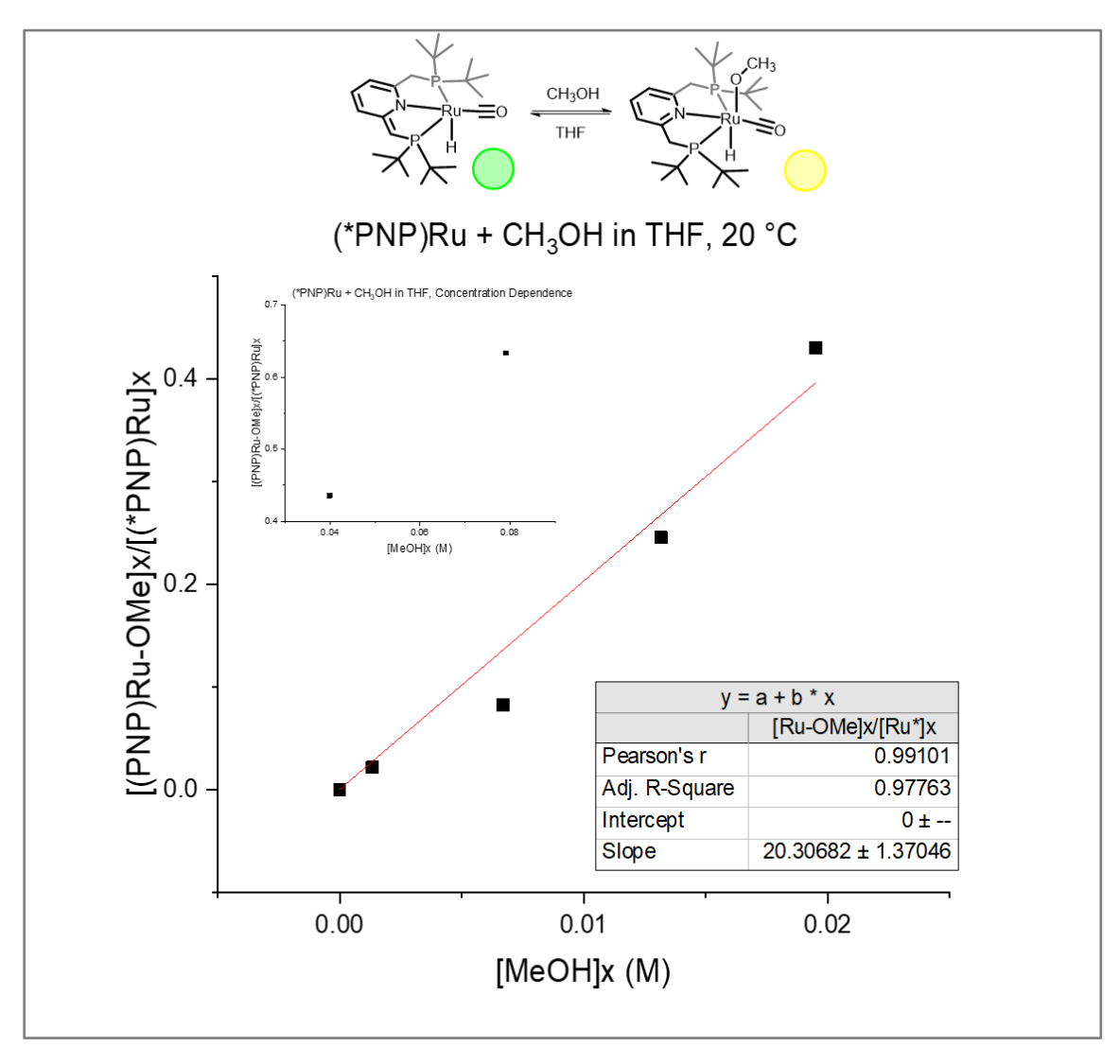


Figure S20: Exemplary plot of [(PNP)Ru-OMe)]/[(*PNP)Ru] versus [MeOH]. Concentrations are derived from initial concentrations and the absorbance at 595 nm, and represent equilibrium concentrations. Data collected at 293 K in THF. **Inset:** Shift in [(PNP)Ru-OMe)]/[(*PNP)Ru] upon diluting a sample.

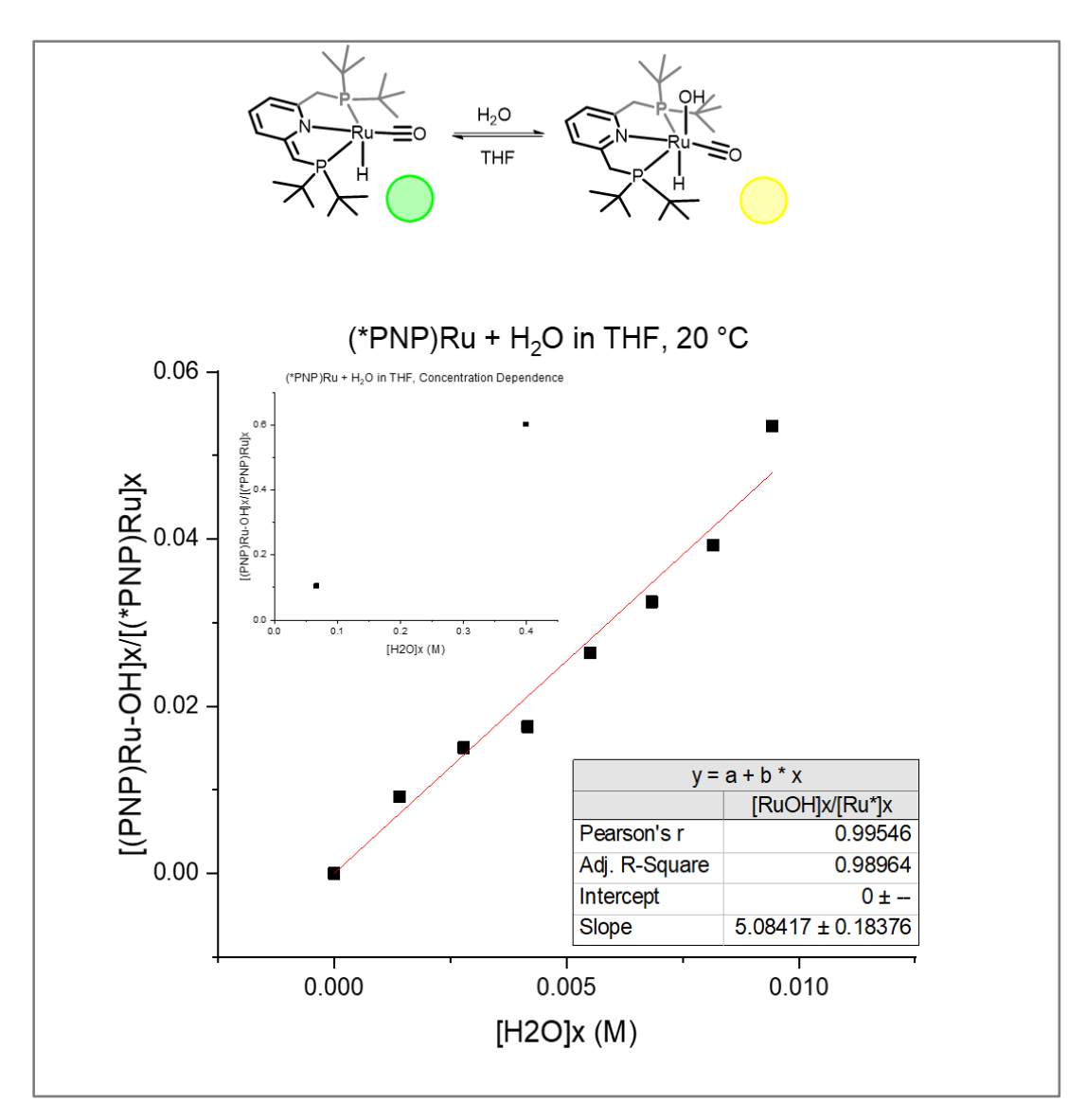


Figure S21: Exemplary plot of [(PNP)Ru-OH)]/[(*PNP)Ru] versus [H₂O]. Concentrations are derived from initial concentrations and the absorbance at 595 nm, and represent equilibrium concentrations. Data collected at 293 K in THF. **Inset:** Shift in [(PNP)Ru-OH)]/[(*PNP)Ru] upon diluting a sample.

Equilibrium of (*PNP)Ru with H₂ and CO₂ (K₁, μ and K₂). Samples of 0.62 mM (*PNP)Ru were subjected to three freeze-pump-thaw cycles inside of the round bottom of the dual stage cuvette shown in Figure S22. Following degassing, the samples were then directly transferred to the cuvette for an initial reference spectrum. The Teflon seal to the round bottom was closed to minimize pressure decreases upon opening to the gas. A calibrated gas addition bulb (260 cm³) was previously sealed under vacuum during the FPT cycle and the bulb was subsequently filled with gas using the Schlenk line and a mercury manometer to note pressure changes. Samples were then opened to the gas substrate and monitored for changes in UV-vis absorbance. This method allows us to accurately add known amounts of gas without worrying about the THF partial pressure, and we account for the pressure drop corresponding to the increase in volume upon opening the gas bulb to the cuvette (cuvette, bulb, and joint volumes were measured by massing before/after addition of water). Given the large headspace, and the solubility of CO218 and H219 in THF, the drop in pressure due to dissolution of the gas was less than 1% for all trials.

Figure S22:
Cuvette with RB
bulb attached,
allowing for freezepump-thawing. A
large, calibrated
bulb is attached to
the cuvette.

The UV-vis was set to cycle, monitoring the reaction's progress hourly until complete. When no further changes were detected, the samples were used for subsequent variable temperature measurements. Initial trials kept the sample open to the bulb, but this resulted in significant

concentration of the sample due to the large headspace volume allowing for much THF vapor to accumulate at high temperatures. To circumvent this, after equilibration occurred at room temperature, the cuvette was isolated from the bulb and allowed to temperature equilibrate with stirring for two hours before collecting each VT UV-vis spectrum between 20 and 70 °C.

Importantly, because the pressure loading and volume of the bulb must ensure excess gas relative to Ru, $K_{eq, 20C}$ was difficult to distinguish spectroscopically. Therefore $K_{eq, 20C}$ were determined by extrapolation from the linear fit of the van't Hoff plot. Only pressures that allowed us to accurately measure the ratio of Ru species were used, using a threshold of 20.

Error is from duplicate or triplicate runs (standard deviation).

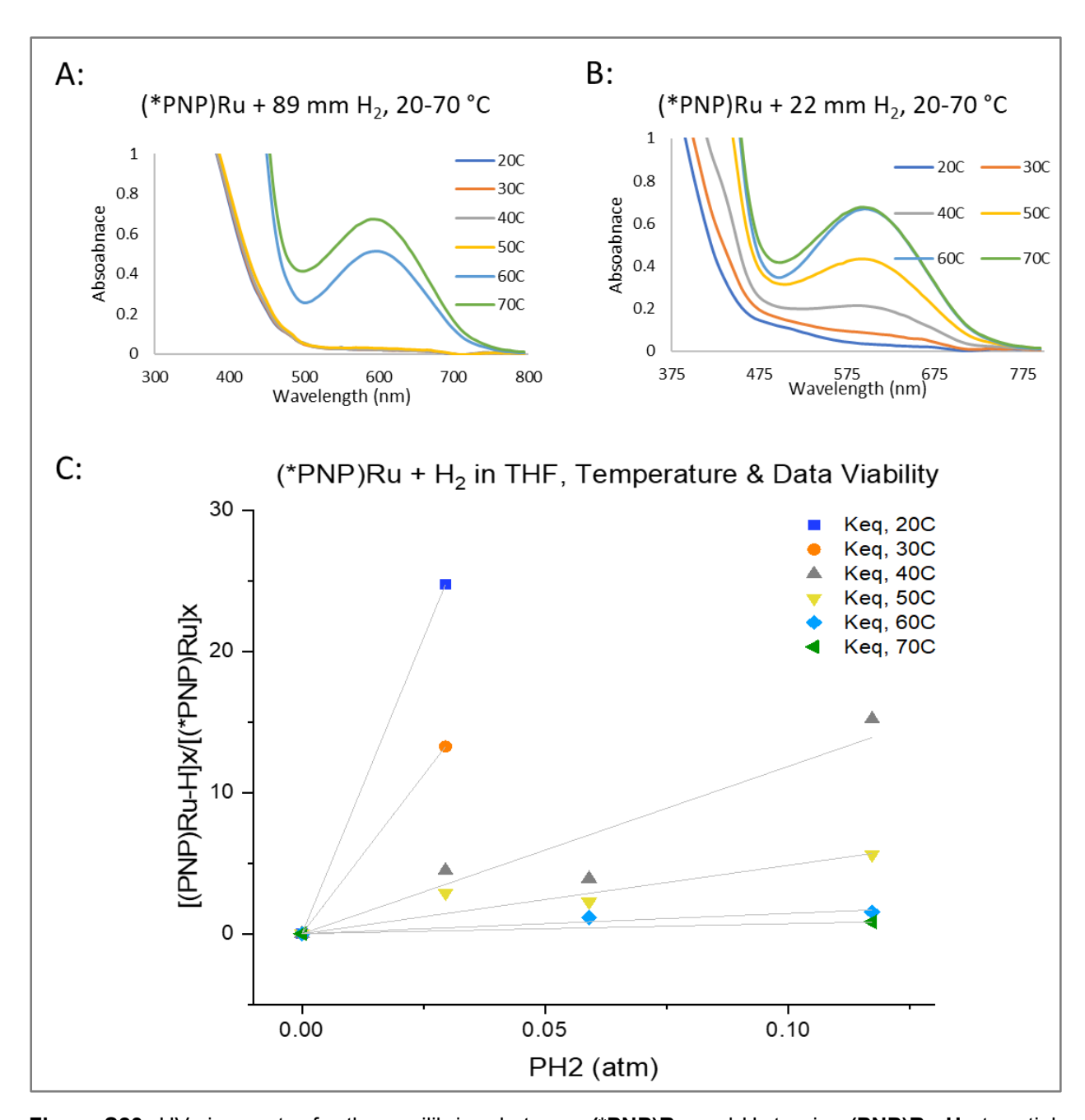


Figure S23: UV-vis spectra for the equilibrium between **(*PNP)Ru** and H₂ to give **(PNP)Ru-H** at partial pressures of 89 mmHg **(a)** and 22 mmHg **(b)**. A plot of **[(PNP)Ru-H]/[(*PNP)Ru]** vs. H₂ partial pressure is shown below **(c)** at different temperatures.

Equilibrium of (PNP)Ru-H with CO₂ (K₉). Given the similarities in the UV-vis spectra of **(PNP)Ru-H** and **(PNP)Ru-CO₂**, it was not possible to accurately determine the relative amounts of the two species using this method. An estimate for the K_9 was determined via NMR spectroscopy as follows. A solution of **(PNP)Ru-H** (20 mM, 0.5 mL) in THF was prepared in situ by addition of 1 atm of H₂ to a solution of **(*PNP)Ru**. ¹H NMR spectroscopy confirmed clean and complete conversion. The sample was then attached to the Schlenk line via a calibrated bulb and the sample freeze-pump-thawed. CO₂ (0.044 mmol) was added to the calibrated bulb, which was then closed. The sample was opened to the bulb and the CO₂ was condensed with IN₂. The sample was warmed to room temperature and the NMR spectrum recorded. No further changes occurred upon prolonged rocking of the sample. Full conversion was observed, and assuming a detection limit of **(PNP)Ru-OCHO:(PNP)Ru-H** is 100:1 then:

$$K_9 = \frac{[Products]}{[Reactants]} = \frac{[RuOCHO]_x}{[Ru-H]_x \cdot P_{CO2}} = \frac{[0.0198]_x}{[0.0002]_x \cdot 0.19 \ atm} = 521 atm^{-1}$$

The partial pressure of CO₂ was determined from knowing the headspace volume of the J.Young NMR tube, and that 1 equivalent reacted with the Ru.

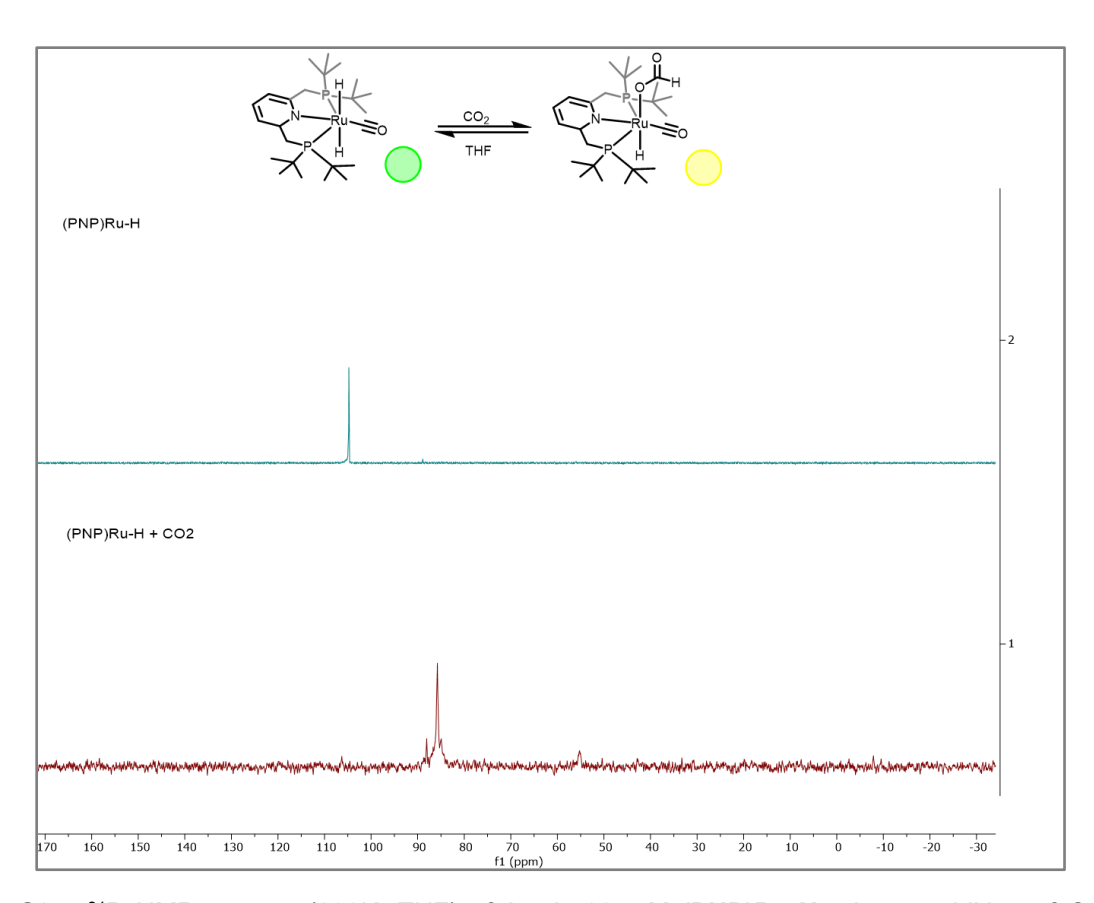


Figure S24: ³¹P NMR spectra (298K, THF) of **(top):** 20 mM **(PNP)Ru-H** prior to addition of CO₂ and **(bottom):** upon addition of CO₂, showing complete conversion to **(PNP)Ru-OCHO**.

Variable Temperature Measurements

The samples prepared for room temperature measurements were used for variable temperature measurements. Samples were placed in quartz cuvettes with Teflon seals, removed from the glovebox, and loaded into a Quantum Northwest Q6 sample changer. A script for the T-App temperature control panel was designed to increase the cell holder temperature every two hours; samples were allowed to temperature equilibrate during this time before spectra were collected. The temperature dependence of K_{eq} was assessed via van't Hoff plots. Some substrates (CO₂, H₂, (DMA-H)(DMC), and formic acid) gave clean and reversible reactions between the temperature range of 20-70 °C, as ascertained by identical UV-vis spectra at 20 °C before and after heating. In contrast, samples with methanol and water were not perfectly reversible, and appear to be unstable at elevated temperatures. These substrates were analyzed between 0-40 °C unless otherwise stated. NMR stability tests showed that in this temperature range, no degradation is observed for several hours. Van't Hoff data from at least two separate runs are shown below.

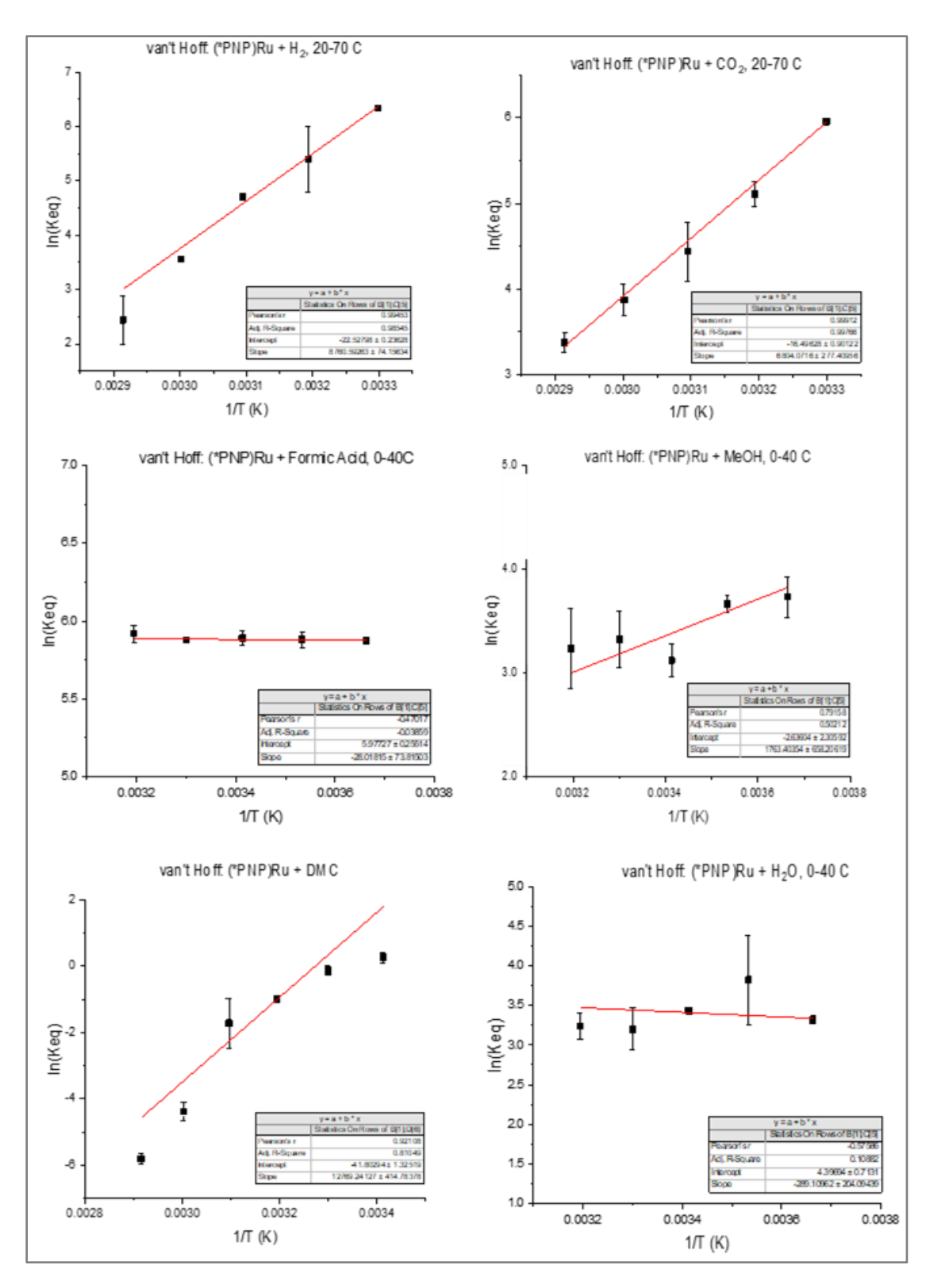


Figure S25: van't Hoff plots for the equilibria of (*PNP)Ru with H-X or CO₂ in THF. Error bars correspond to the standard deviation from multiple runs. The plot that corresponds to the equilibrium of (*PNP)Ru with (DMA-H)(DMC) is not linear, with curvature at high temperatures. We know that at elevated temperatures (PNP)Ru-DMC can be converted to (PNP)Ru-CO₂ (See Figure S26), indicative of more complex equilibria.

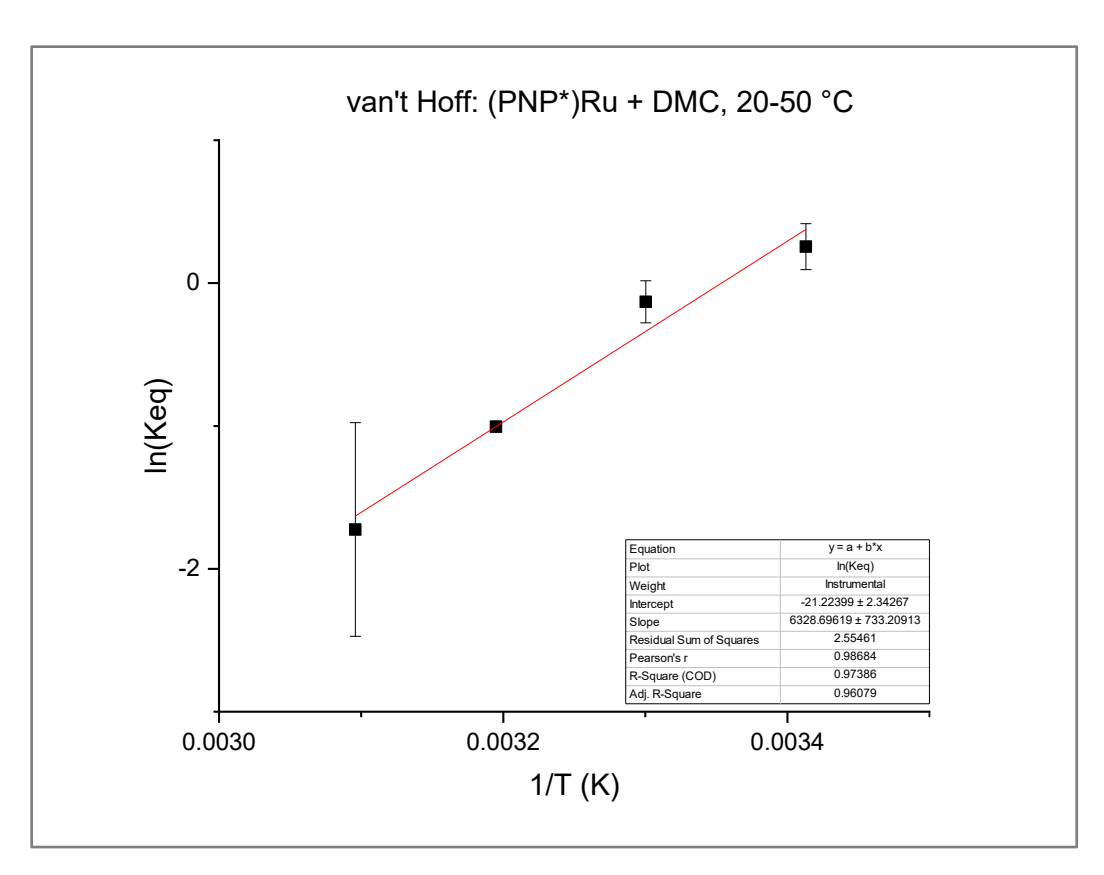


Figure S26. Fitting of the van't Hoff plot for the equilibrium between **(*PNP)Ru** and (DMA-H)(DMC), using only the linear, low-temperature region.

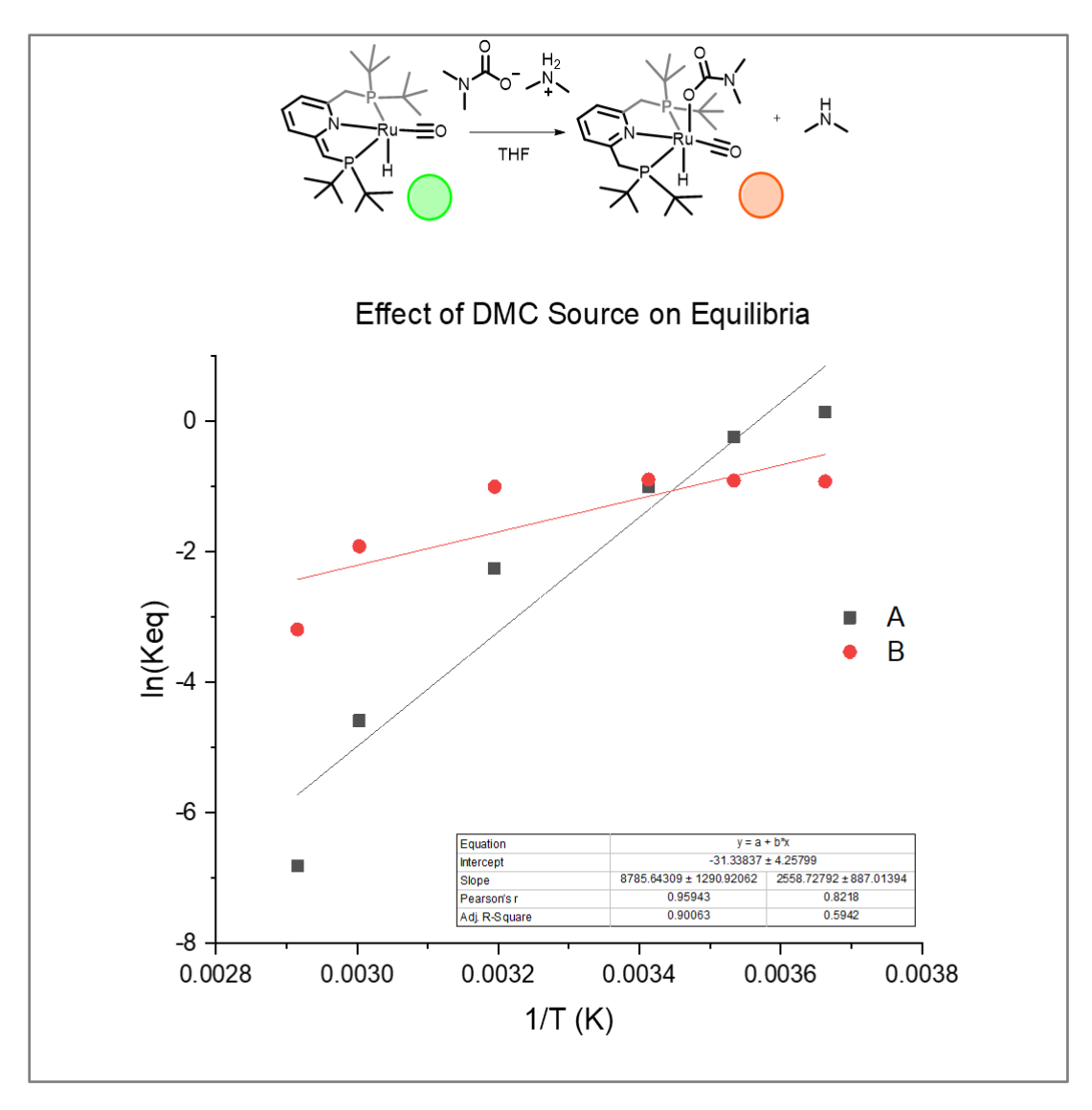


Figure S27: Effect of (DMA-H)(DMC) source on the equilibrium with **(*PNP)Ru**. Sample A is from a new container of DMC (Sigma-Aldrich) with a K_{eq} (20 °C) of 1.1, and Sample B from a one year old container. Sample B gave a lower K_{eq} (20 °C) of 0.4. This may suggest a relevant Me_2NCO_2 \rightleftharpoons CO_2 + HNMe₂ dynamic over time that affects equilibria and catalysis.

Section 5: Hydrogenations

All high pressure/ high temperature reactions were carried out using a Parr Model 5000 multichannel reactor outfitted with six 75 mL HASTC alloy vessels with stirring, pressurized gas inlet valves, and pressure / temperature monitoring. The system is controlled using a model 4871 process controller and SpecView version 2.5 software. Each vessel is loaded inside of the glovebox (using only new dimethylammonium dimethyl carbamate - see Figure S27), sealed, and transferred to the reactor. For a standard experiment, 0.1 mL of a 0.005 M (PNP)Ru-CI solution was added to a vessel containing ^tBuOK (0.0028 g, 50 equiv) and 0.1 mL of a 0.46 M dimethylammonium dimethylcarbamate solution (92 equiv). To the solution was added THF until the volume reached 10 mL total, and a stir bar was added. While related studies typically use smaller volumes, we found 10 mL provided more straightforward handling and reproducibility as any solvent vapors lost during workup represented a less significant portion of the reaction mixture. Once the thermocouple, pressure sensor, and gas inlet are attached. the gas line is evacuated for 5 minutes, refilled with pressurized H₂, and purged to minimize air contamination. Each vessel is then pressurized to 50 bar H₂ at room temperature, sealed, and heated to 155 °C for 18 hours with stirring at 1500 rpm, then allowed to cool to room temperature. The room temperature vessels are placed in a dry ice-acetone cooling bath for 10 minutes before venting through a metering valve. Production of formate was quantified using a Thermo Scientific Integrion Dionex HPIC and referenced to a formate calibration curve with a method detection limit of 1 x 10⁻⁵ M; samples were made using 1.98 mL 18 MΩ H₂O, 20 μL reaction aliquot, and ground NaOH until the pH of the sample reaches 8, as determined by Hydrion pH paper. Production of methanol was quantified using an Agilent 5890B GC and 5975C MS and referenced to methanol and DMF calibration curves with a method detection limit of 3 x 10⁻⁵ M for methanol and 1 x 10⁻³ for DMF; samples were made using 2 mL of the reaction mixture and acidified with 1 µL 12M HCl, or until pH = 6, as determined by Hydrion pH paper.

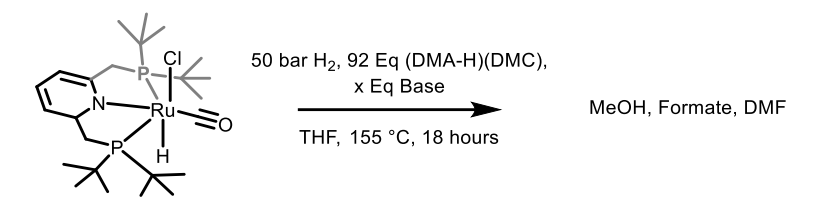


Table S4: Effect of Base: (DMA-H)(DMC) Ratio on Product TON and Selectivity.

Catalyst Concentration and Loading (mol %)	^t BuOK (Eq)	(DMA- H)(DMC) (Eq)	TON MeOH (M)	TON Formate (M)	TON DMF (M)
0.05 mM (1 %)	50	92	3.9 ± 0.3 (2.1 x 10 ⁻⁴)	$3.3 \pm 0.2 (1.7 \times 10^{-4})$	19.8 ± 5.4 (4.1 x 10 ⁻³)
0.05 mM (1 %)	100	100	3.4 ± 2.6 (1.4 x 10 ⁻⁵)	6.7 ± 2.3 (7.4 x 10-5)	Not Detected
0.05 mM (0.5 %)	50	184	2.0 ± 0.6 (1.2 x 10 ⁻⁴)	$0.7 \pm 0.1 (3.5 \times 10^{-5})$	22.3 ± 7.2 (5.7 x 10 ⁻³)

0.05 mM	200	184	0.8 ± 0.1 (3.9	0.6 ± 0.2 (3.2 x 10 ⁻⁵)	20.9 ± 6.9 (1.7
(0.5 %)			x 10 ⁻⁵)		x 10 ⁻³)

Table S5: Controls.

Catalyst Concentration and Loading (mol %)	Base Eq	(DMA-H)(DMC) (Eq)	TON MeOH (M)	TON Formate (M)	TON DMF (M)
0.05 mM (100 %)	^t BuOK 50		Not detected	3.8 ± 1.3 (1.9 x 10 ⁻⁴)	Not detected
0.05 mM (1 %)		92	Not detected	0.6 ± 0.3 (3.5 x 10 ⁻⁵)	Not detected
	^t BuOK 50	92	Not detected	Not detected	Not detected

Table S6: Comparison with RuMACHO-BH.

Catalyst Concentration and Loading (mol %)	Base	TON MeOH	TON Formate	TON DMF (M)
0.05 mM	^t BuOK	1.9 ± 2.3 (9.7 x 10 ⁻⁵	0.6 ± 0.4 (2.9x 10 ⁻⁵	Not detected
(1 %)		M)	M)	
0.05 mM	K ₃ PO ₄	1.7 ± 0.8 (8.5 x 10 ⁻⁵	0.4 ± 0.2 (2.2 x 10 ⁻⁵	Not detected
(1 %)		M)	M)	

Notes: Data in table S6 was rationalized based on previous work by Sanford and coworkers in which K_3PO_4 was used as the base. In their report, TON for CH₃OH was $20;^{20}$ we were able to replicate this data but with greater variability (TON = 60 ± 50) when using similar conditions to theirs: 0.2 mL of a 0.0245 M **RuMACHO-BH** stock solution, 61 Equiv. K_3PO_4 , 92 Equiv. DMC, and 2 mL total volume THF. It should be noted that the concentration of the experiments above (0.05 μ M), are significantly more dilute compared to the work by Sanford (3.3 μ M), which may contribute to the discrepancy between these reports.

Table S7: Effect of Dilution on TON

Catalyst Concentration and Loading	Base (Eq)	TON MeOH (M)	TON Formate (M)	TON DMF (M)
(mol %)				
0.05 mM (1 %)	(Me) ₂ NCO ₂ - Li ⁺ , (100)	$39.4 \pm 0.4 (2.0 \times 10^{-3} \text{ M})$	6.3 ± 5.7 (3.2 x 10 ⁻⁴ M)	Not detected
0.025 mM (1 %) ^{a,}	(Me) ₂ NCO ₂ - Li ⁺ , (100)	$17.0 \pm 5.6 (4.6 \times 10^{-5} \mathrm{M})$	$6.7 \pm 2.3 (7.4 \times 10^{-5})$	Not detected

^aReaction is run in double (20 mL) the normal solvent to observe if concentration dependence on methanol can be overcome. **Notes:** We find that the catalyst is extremely sensitive to impurities and hence the lower concentration observed upon dilution may be due to partial catalyst de-activation from THF impurities. As now all reagents are at a lower concentration, this may impact related equilibria, such as that between DMA and CO₂. We did not increase the time of the catalytic run which may also contribute to the lower TON.

Analysis of Speciation after Catalysis.

A solution of 0.0096 g (0.017 mmol) (PNP)Ru, 0.1088 g (0.97 mmol) ^fBuOK, and 2.3 μL (1.8 mmol) dimethylammonium dimethylcarbamate and 10 mL THF was prepared in the glovebox and loaded into a Parr vessel. The vessel was sealed, pressurized to 50 bar with H₂ and heated for 18 hours at 155 °C. The reaction was allowed to cool to room temperature, then was further cooled in a dry ice-acetone cold bath for 15 minutes. A mineral oil bubbler was attached to the metered pressure release valve, and the vessel was allowed to depressurize, then was taken into the glovebox. The reaction solution was decanted, concentrated *in vacuo*, redissolved in 2 mL Benzene, filtered over celite, and washed twice with 1 mL benzene. The total filtrate was concentrated in vacuo, redissolved in 0.5 mL THF-d₈, and analyzed by ¹H, ¹H{³¹P}, ³¹P NMR and IR spectroscopy (THF solution) revealing a mixture of products. *IR (THF solution):* 1907 cm⁻¹(ν_{CO}), 1938 cm⁻¹(ν_{CO}); 1560 cm⁻¹ (ν_{COO}), 1652 cm⁻¹ (ν_{COO}).

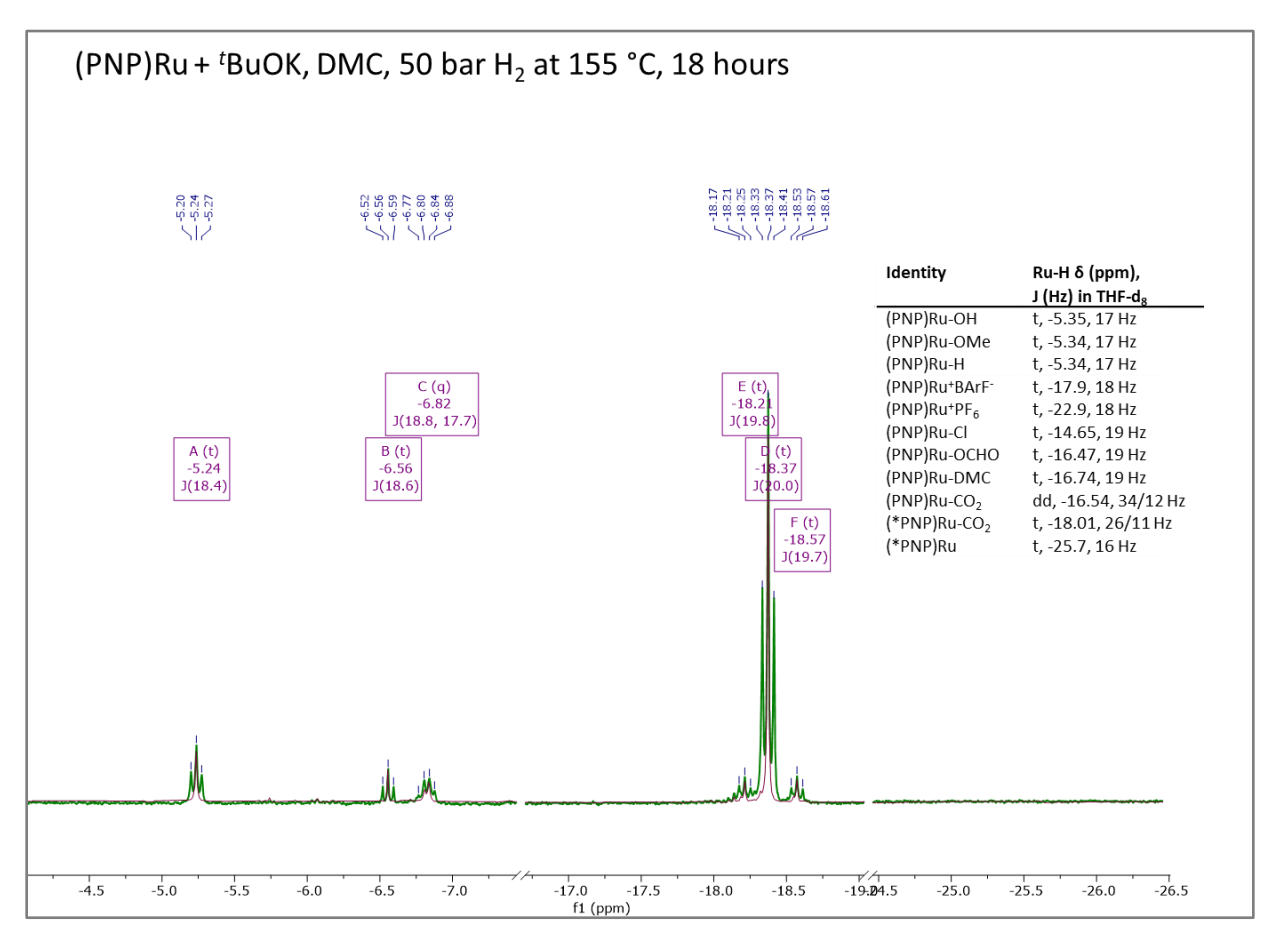


Figure S28: ¹H NMR spectra (500 MHz, 293 K, THF-*d*₈) of **(PNP)Ru-CI** Parr Reaction (3.4 mM) with (red) and without (green) phosphorous decoupling. The peak at -5.2 ppm is consistent with **(PNP)Ru-H** by chemical shift and J coupling constant (see insert). The major product at -18.4 ppm is most consistent with

 $(PNP)Ru^+$ - two analogues of which are known: $(PNP)Ru^+(PF_6)$ and $(PNP)Ru^+(BAr_F)$ observed in THF at - 22.9 (t, J = 18 Hz) and -17.9 ppm (t, J = 18 Hz), respectively.

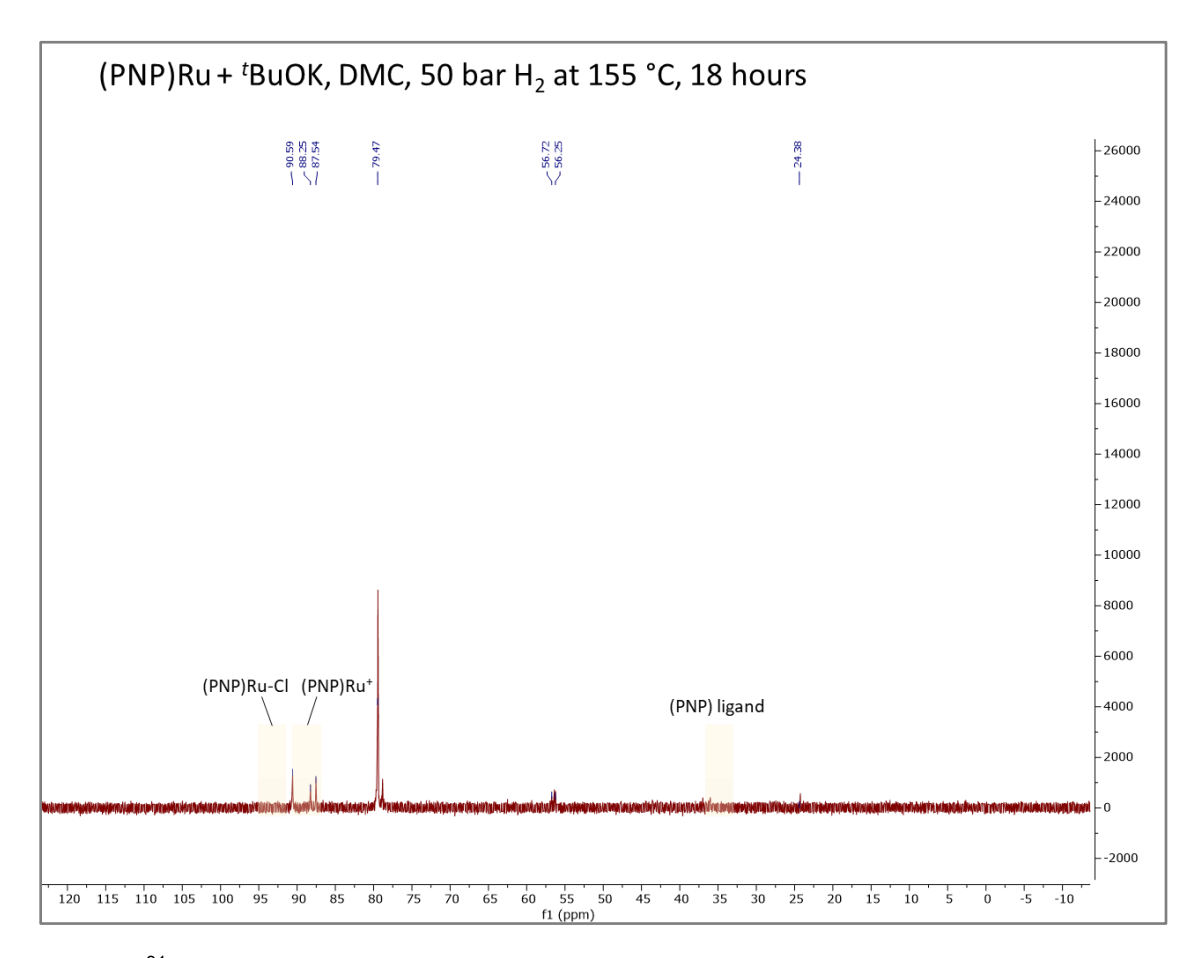


Figure S29: ³¹P NMR spectra (293 K, THF-*d*₈) of **(PNP)Ru-CI** Parr Reaction (3.4 mM). The peaks between 85 and 90 ppm are consistent with the 1H data, suggesting a cationic species may be formed: **(PNP)Ru⁺(PF₆)** and **(PNP)Ru⁺(BAr_F)** observed in THF at 86.0 (singlet) and 90.0 ppm (singlet), respectively.

Section 6: NMR Reactions

NMR reactions were setup inside of the glovebox using J. Young valved NMR tubes for gas reactions, and standard tubes for all other purposes. Reactions forming (PNP)Ru-H, (PNP)Ru-OCHO, and (PNP)Ru-CO₂ were made by subjecting a sample of (*PNP)Ru to three freeze pump thaw cycles and backfilling with the appropriate gas/ gas sequence.

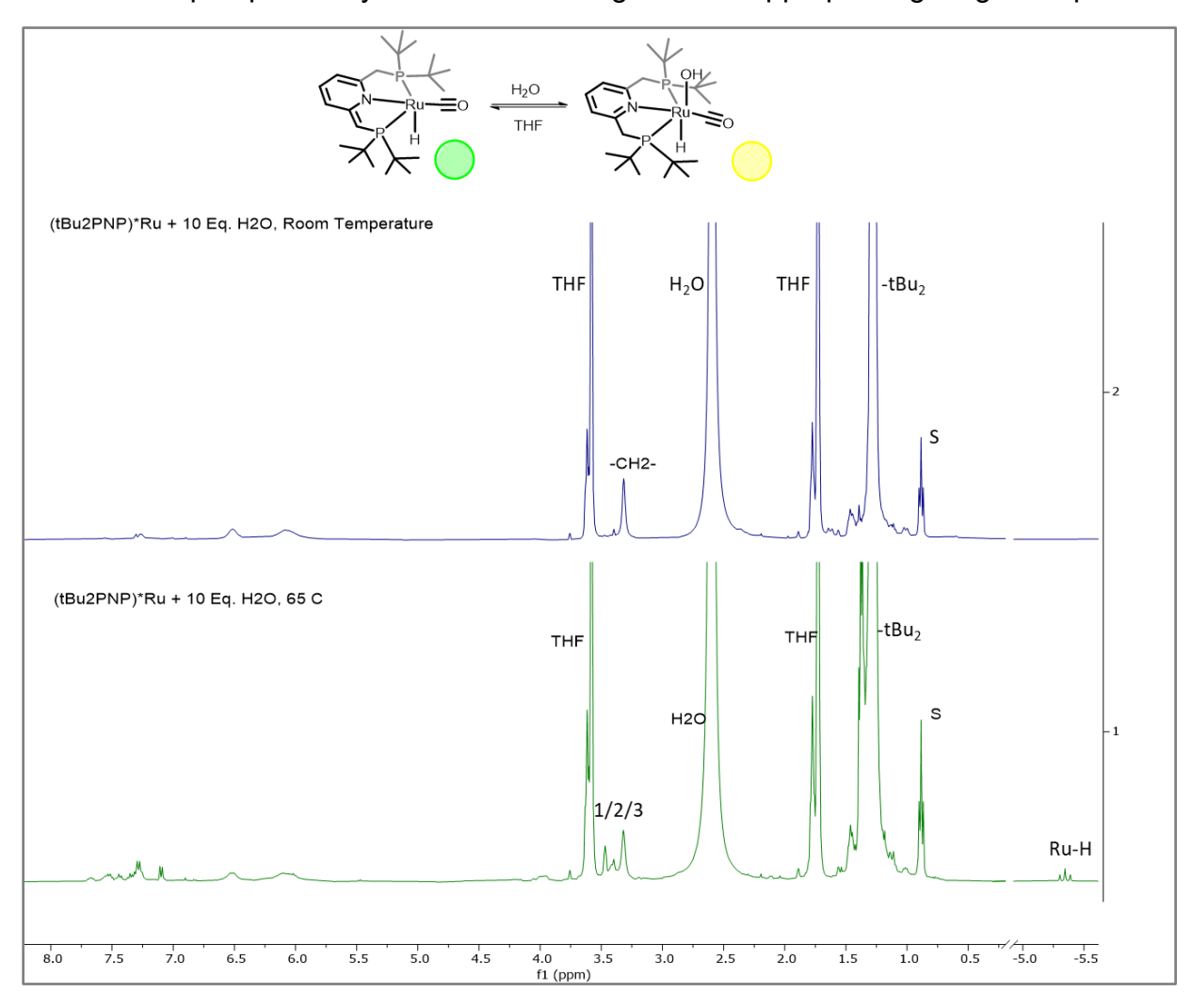


Figure S30: 1 H NMR spectra (400 MHz, THF- d_{8}) of (*PNP)Ru (10 mM) with H₂O (100 mM). (top): Data collected at 293 K. (bottom): Data at 358 K. Upon cooling, the spectrum remains unchanged. New peaks for the backbone methylene (1,2, & 3) and t Bu₂ suggest formation of another species Solvent impurities 'S' are from pentanes.

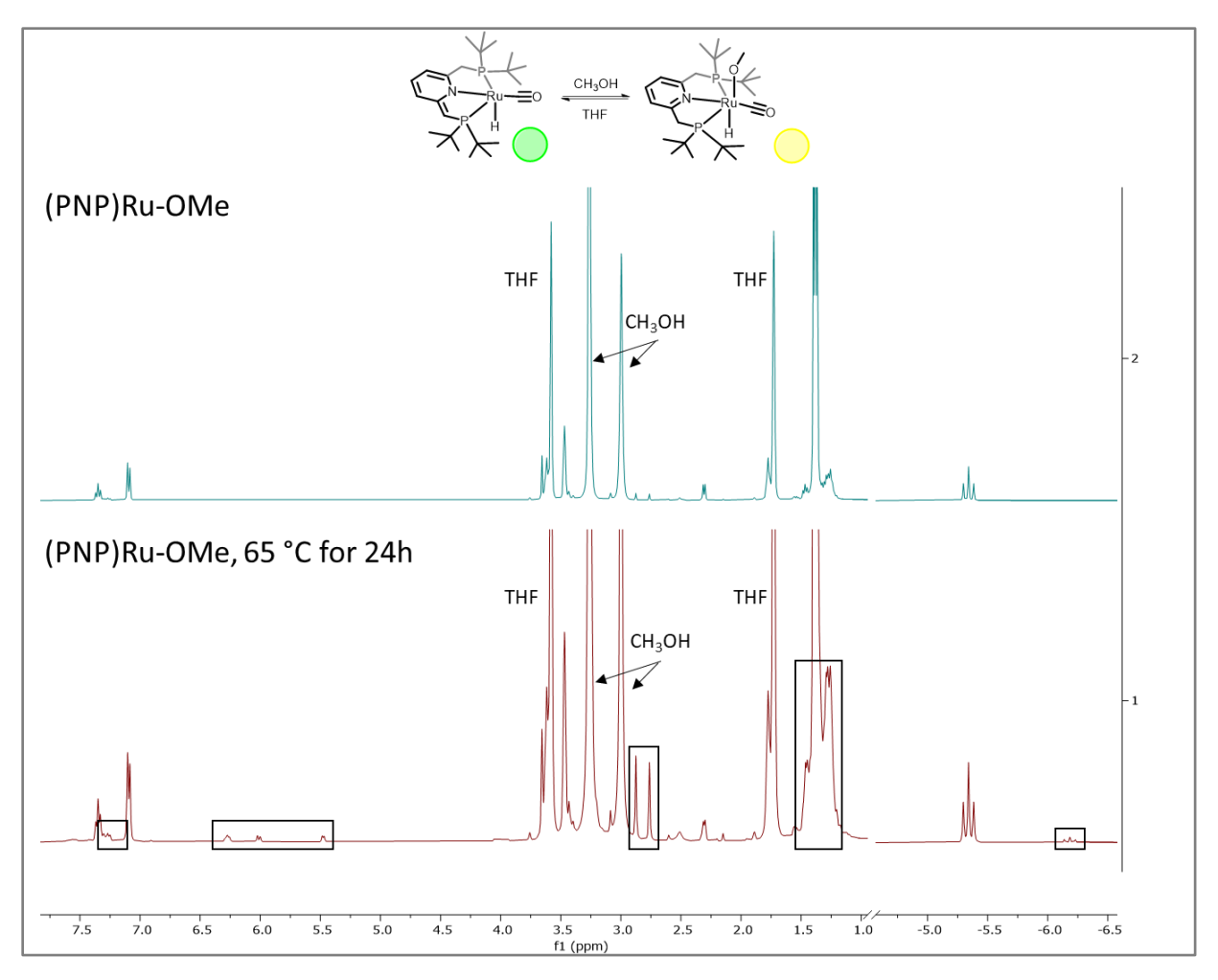


Figure S31. ¹H NMR spectra (400 MHz, THF-*d*₈, 293 K) of (*PNP)Ru (38 mM) with MeOH (99 mM). (top): Data collected prior to heating the sample showing full conversion to (PNP)Ru-OMe. (bottom): Data collected after heating the sample to 65 °C for 24 h and allowing to temperature equilibrate at room temperature. Resonances between 5.5 and 6.5 ppm (boxed) correspond to (*PNP)Ru. A new unidentified hydride species forms, as evident from the hydride resonance at -6.18 ppm (boxed). Other resonances correspond to (PNP)Ru-OMe.

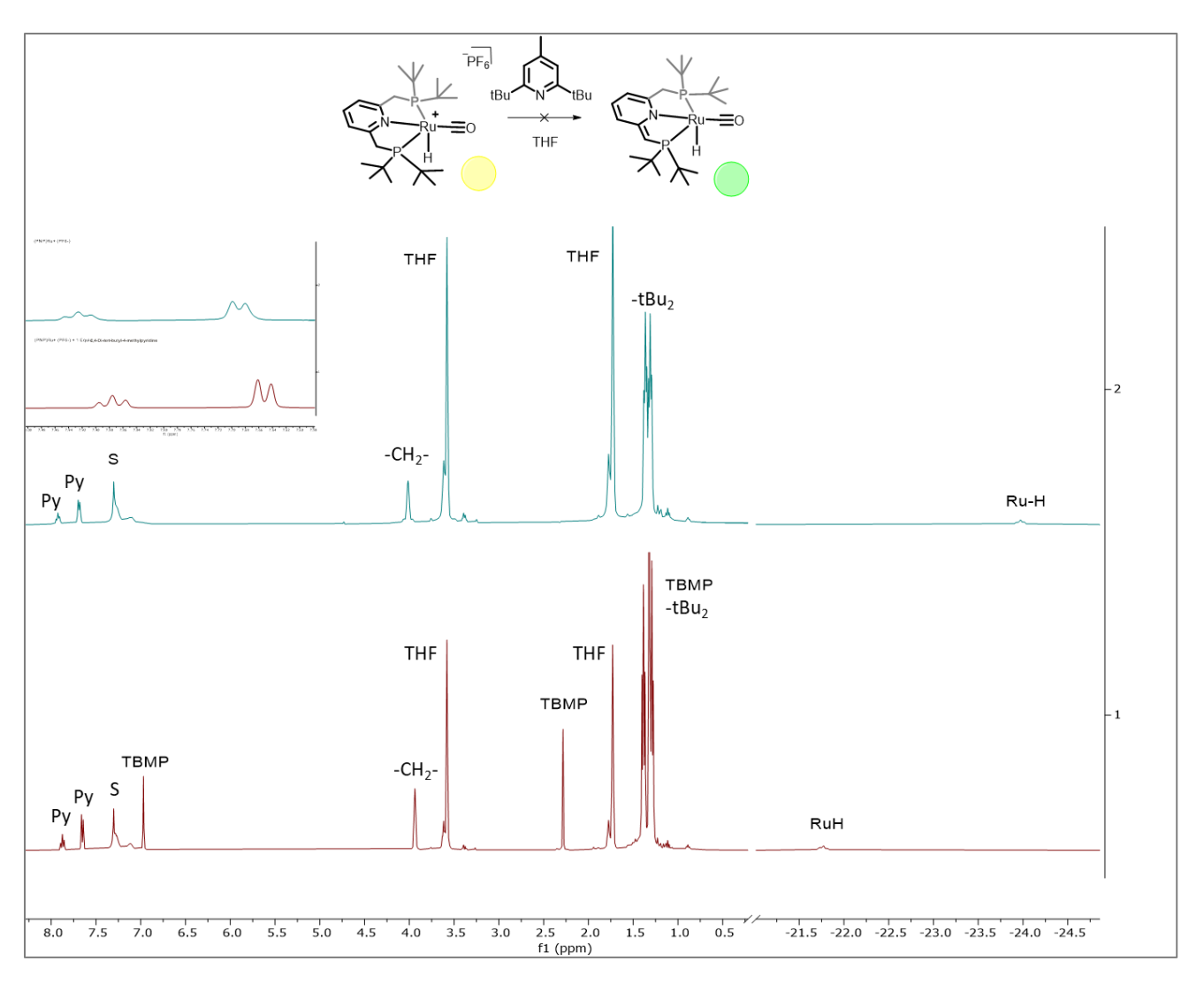


Figure S32: ¹H NMR spectra (400 MHz, 293 K, THF- d_8) of **(PNP)Ru**⁺ (130 mM) prior to **(bottom)** and after **(top)** addition of 1 equiv. 2,4-Di-*tert*-butyl-4-methylpyridine. Movement in the sensitive hydride region is possibly due to base coordination to the open site of **(PNP)Ru**⁺. Solvent impurities 'S' are from benzene. **Inset:** Zoom in on aromatic region to demonstrate shifting resonances.

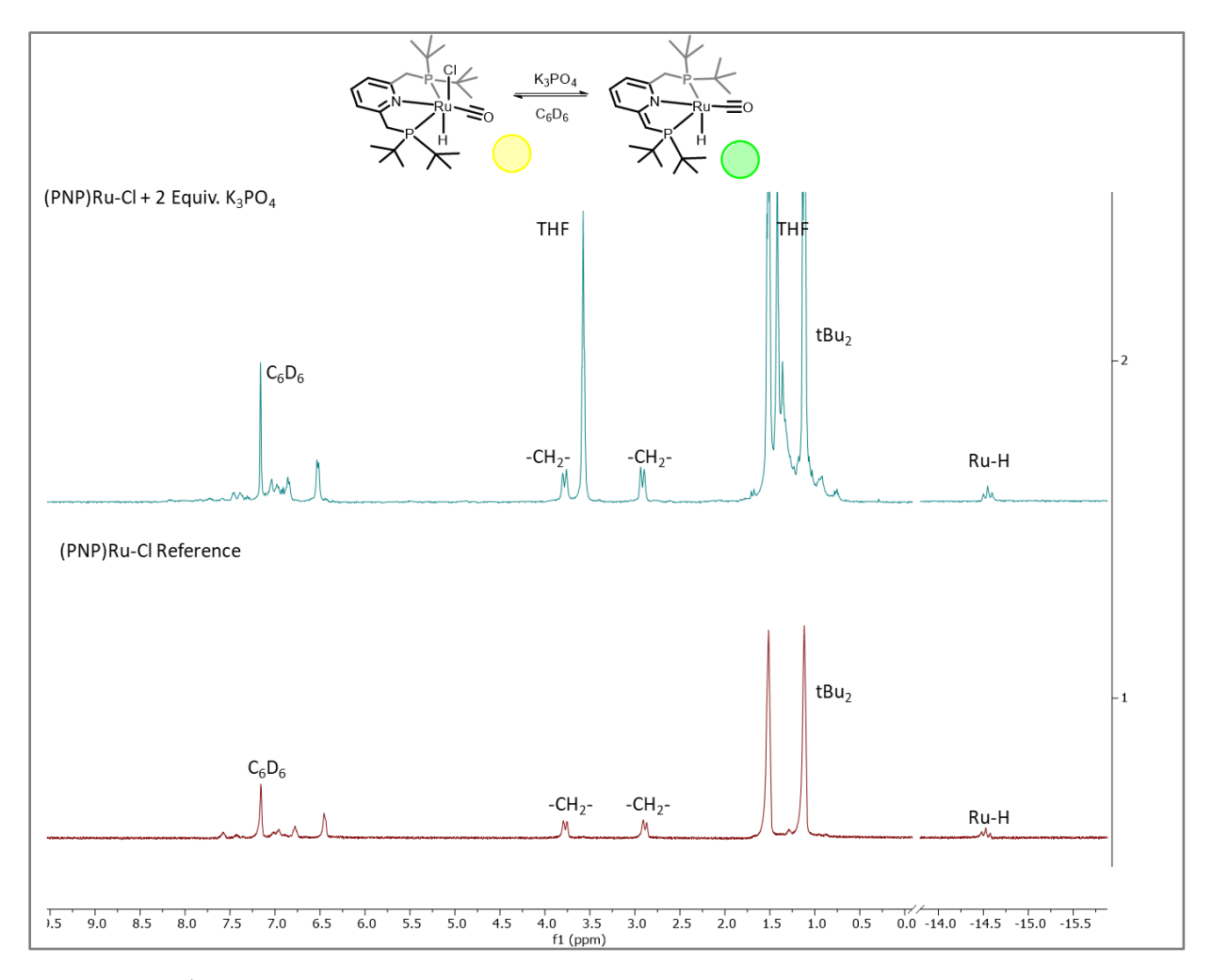


Figure S33: ¹H NMR spectra (400 MHz, 293 K, C_6D_6) of **(PNP)Ru-CI** (54 mM) prior to **(bottom)** and after **(top)** addition of 2 equiv. K₃PO₄ and heating to 120 °C. Both spectra were collected at room temperature. Note while the sample was at 120 °C, the solution turned green from yellow, suggestive of deprotonation.

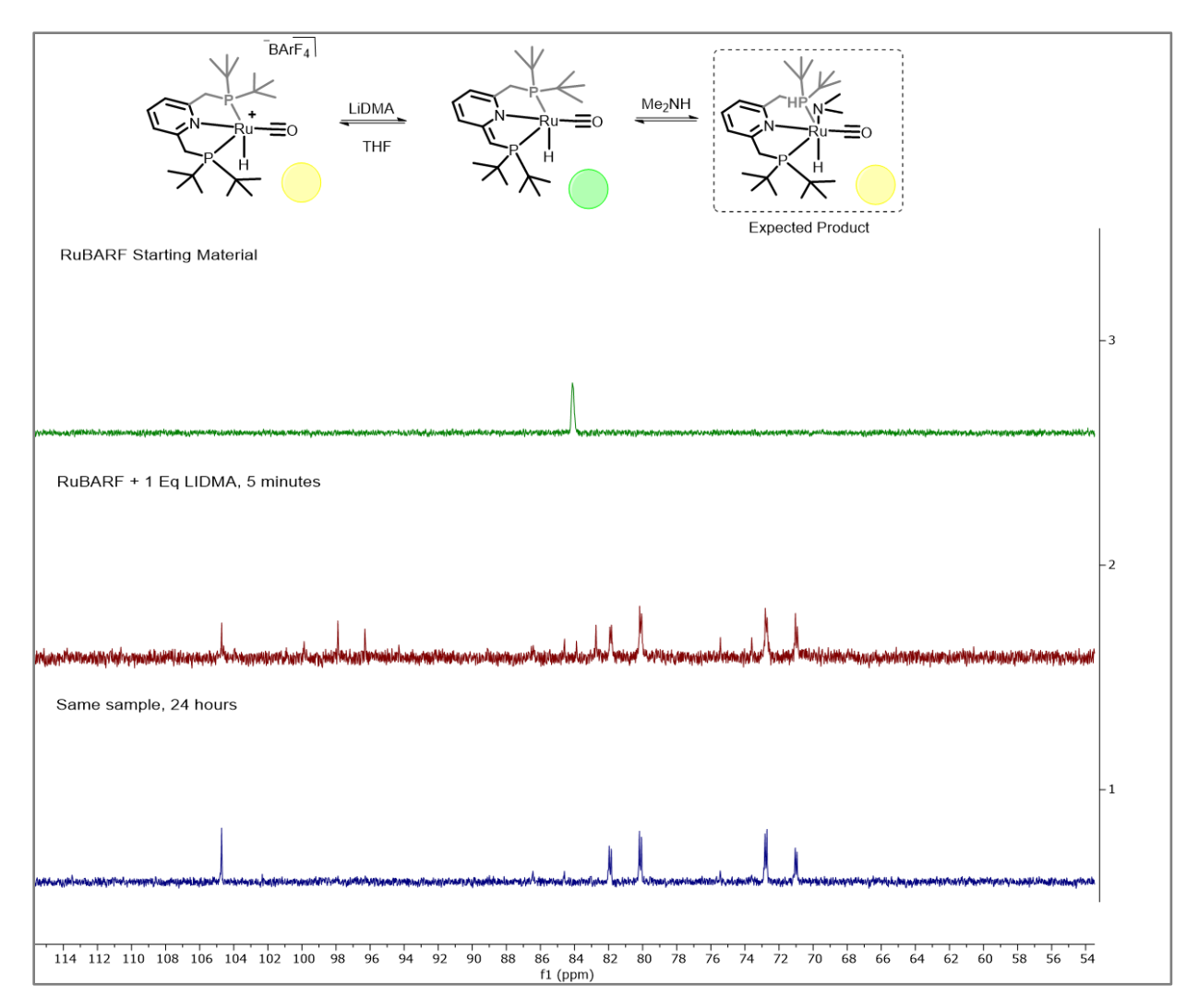


Figure S34: ³¹P NMR spectra of **(PNP)Ru⁺ BArF**⁻ (10 mM) **(top), (PNP)Ru⁺** treated with 1 equiv. (Li)(DMA) at 5 minutes **(middle)**, and an additional time point at 24 hours **(bottom)** showing a mixture of a new species and **(*PNP)Ru** centered at ~ 76 ppm.

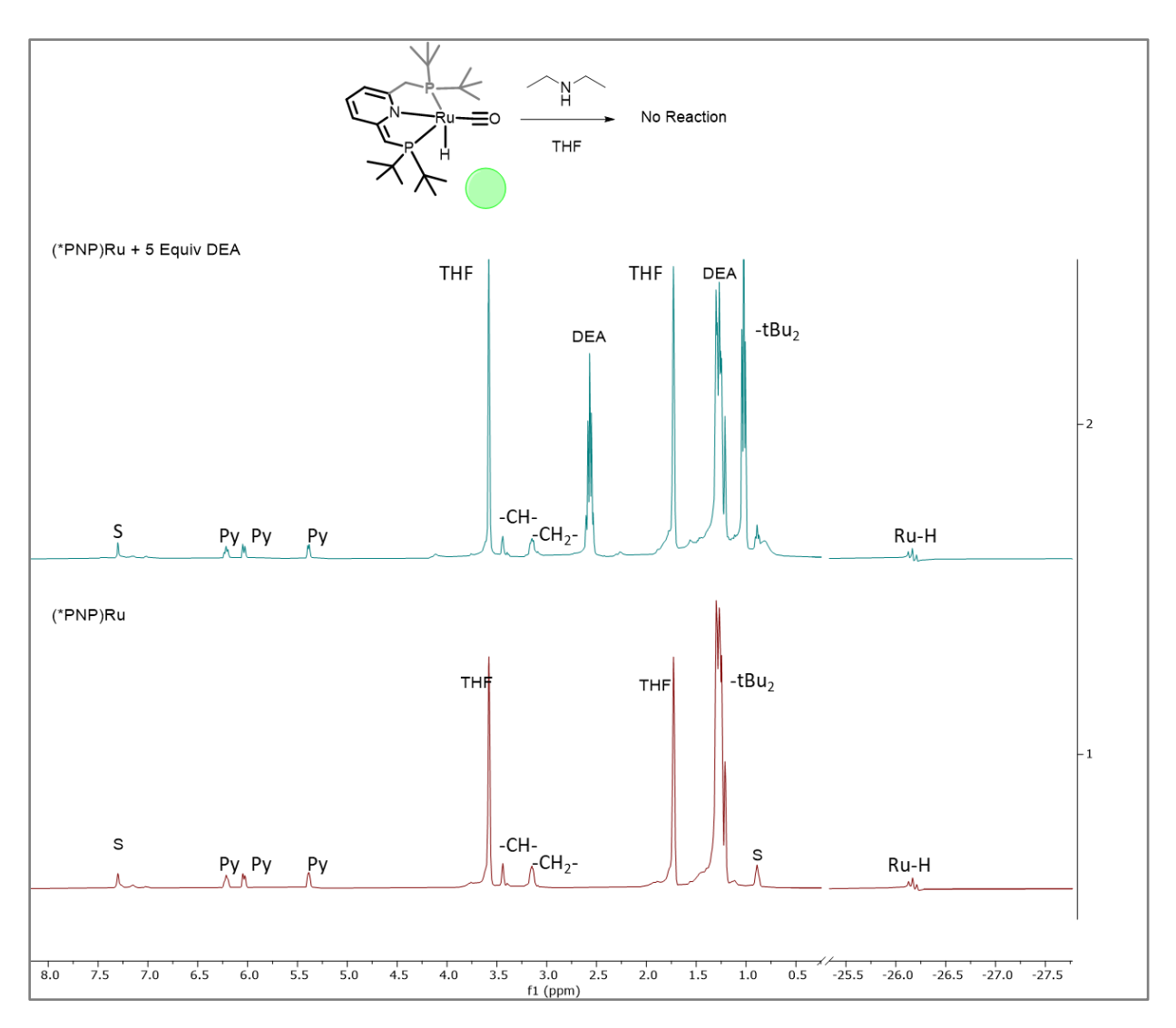


Figure S35: ¹H NMR (400 MHz, 293 K, THF- d_8) spectra of **(*PNP)Ru** (11 mM) before **(bottom)** and after addition of 5 equiv diethylamine **(top)**.

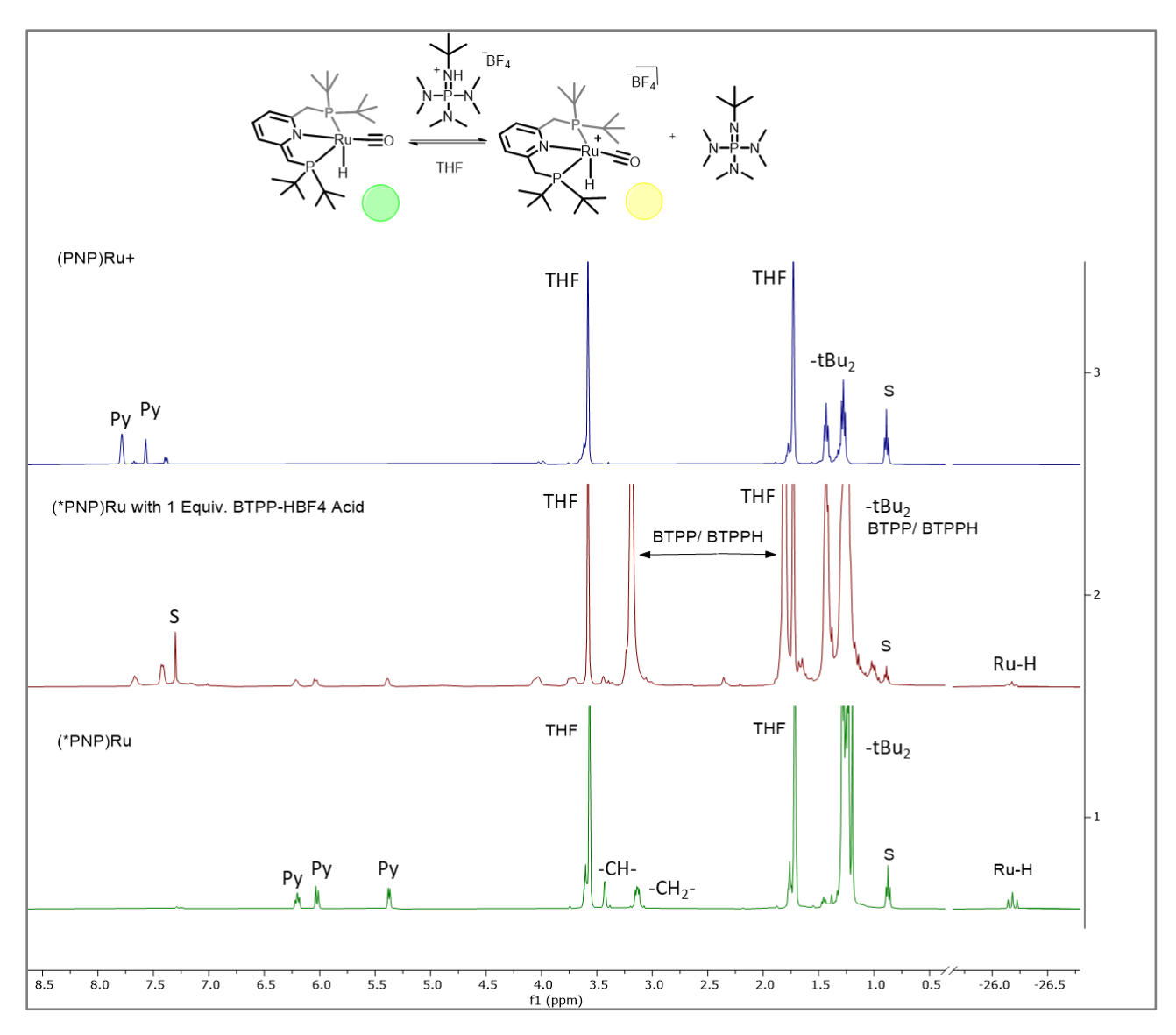


Figure S36: ¹H NMR spectra (400 MHz, 293 K, THF-*d*₈) of **(top): (PNP)Ru**⁺; **(middle): (*PNP)Ru** (8 mM) + 1 equiv BTPP-HBF₄; **(bottom): (*PNP)Ru**. Solvent impurities 'S' are from pentanes. 400 MHz, 293 K.

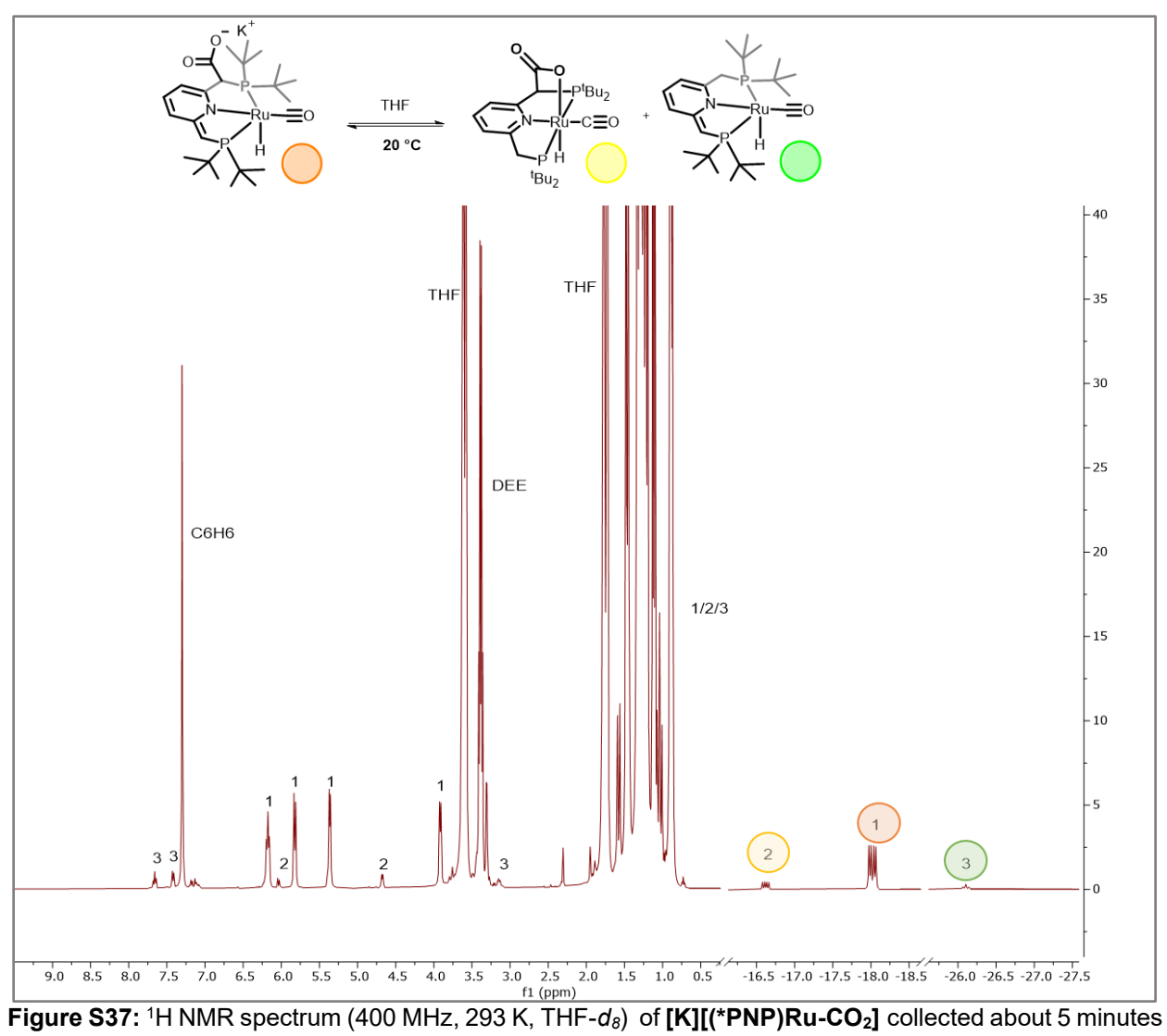


Figure S37: ¹H NMR spectrum (400 MHz, 293 K, THF-*d*₈) of **[K][(*PNP)Ru-CO₂]** collected about 5 minutes after it's preparation. Peaks labelled "1" correspond to the product; "2" corresponds to **(PNP)Ru-CO₂** "3" corresponds to **(*PNP)Ru**. Solvent contaminants: diethyl ether and benzene.

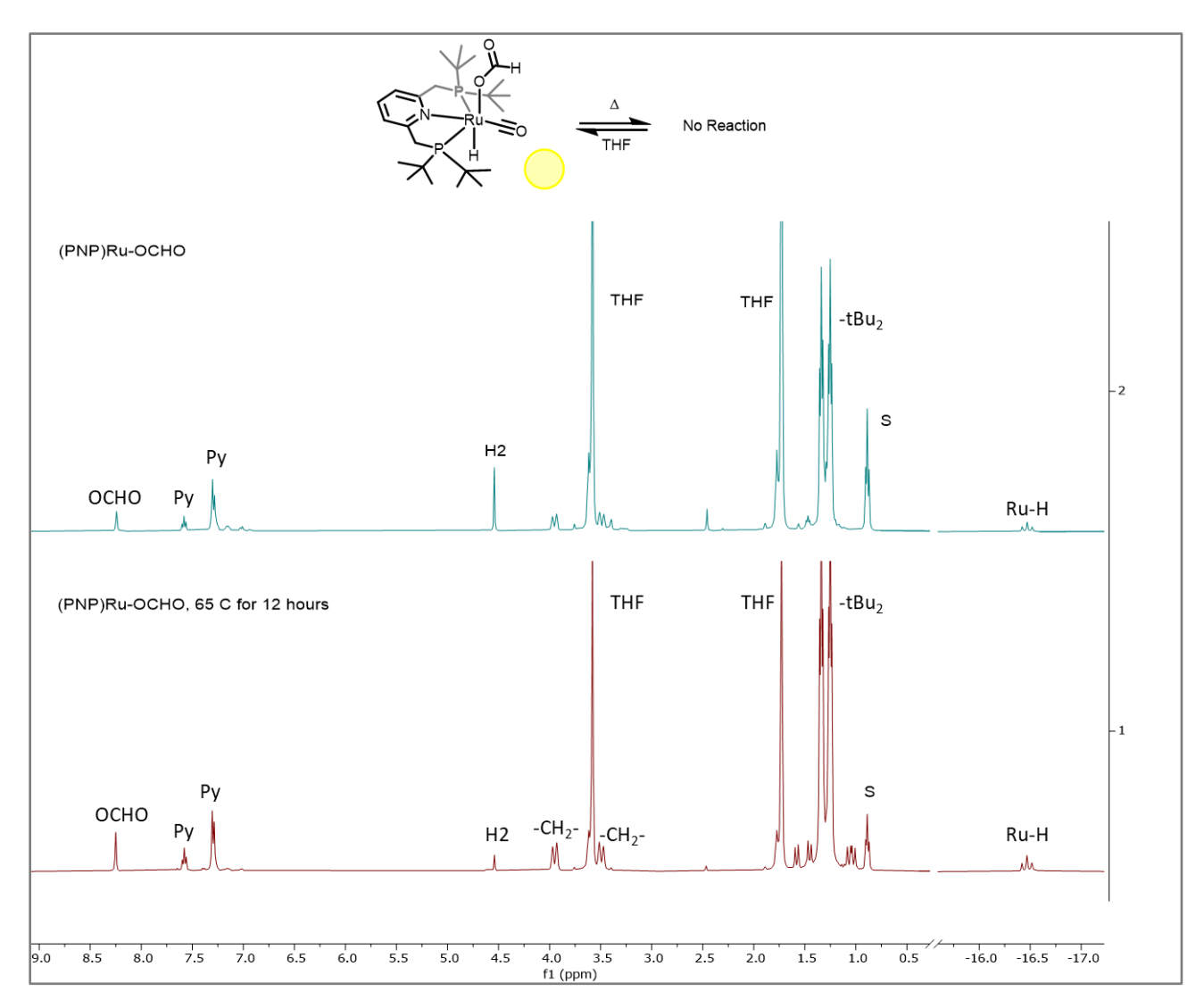


Figure S38: ¹H NMR spectra (400 MHz, 293 K, THF- d_8) of **(PNP)Ru-OCHO** prior to **(top)** and after heating in an aluminum block to 65 °C for 12 h **(bottom)**. Additionally, no color change from yellow (RT) to green at 65 °C (characteristic of **(PNP)Ru-OCHO** \rightarrow **(*PNP)Ru)** was observed at either temperature. Solvent impurities 'S' are from pentanes.

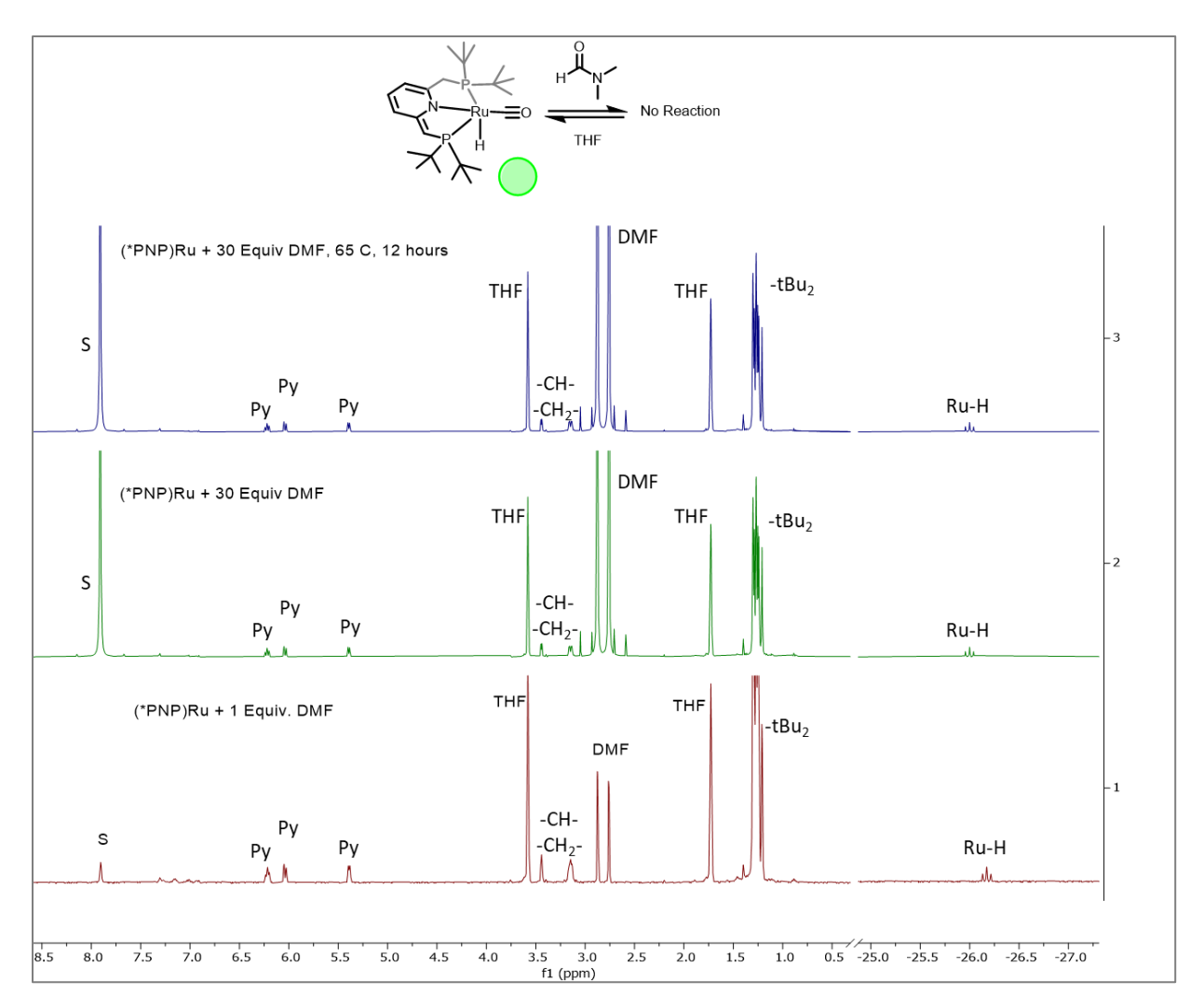


Figure S39: ¹H NMR spectra (400 MHz, 293 K, THF-*d*₈) of 9 mM (*PNP)Ru with (bottom): 1 equiv DMF; (middle): 30 equiv DMF; (top): same as middle but after heating to 65 °C overnight. Solvent impurities 'S' are from benzene.

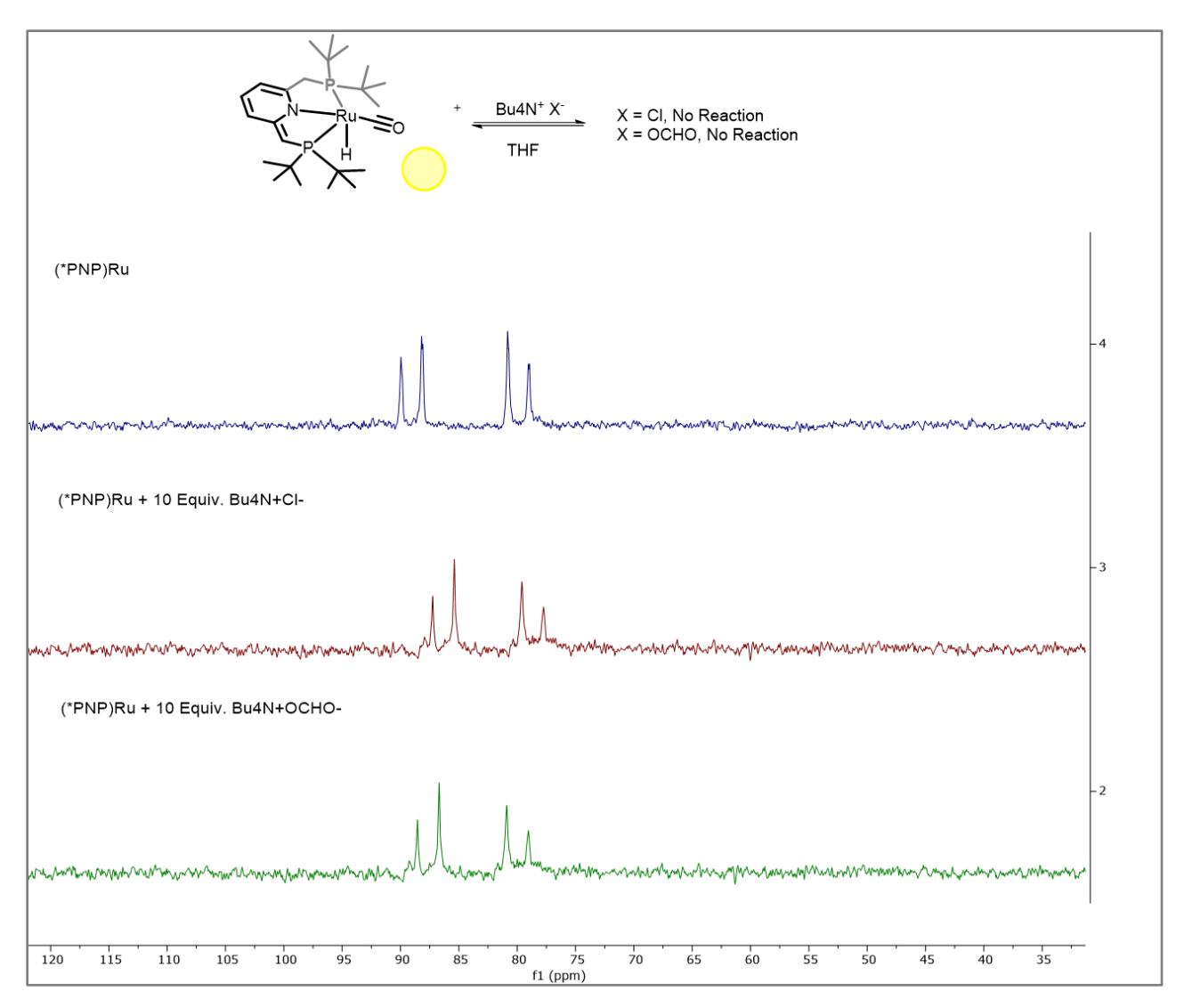


Figure S40: ^{31}P NMR spectra (293 K, THF) of (top): 8 mM (*PNP)Ru; (middle): treated with 10 equiv $Bu_4N^+Cl^-$; (bottom): treated with 10 equiv $Bu_4N^+OCHO^-$.

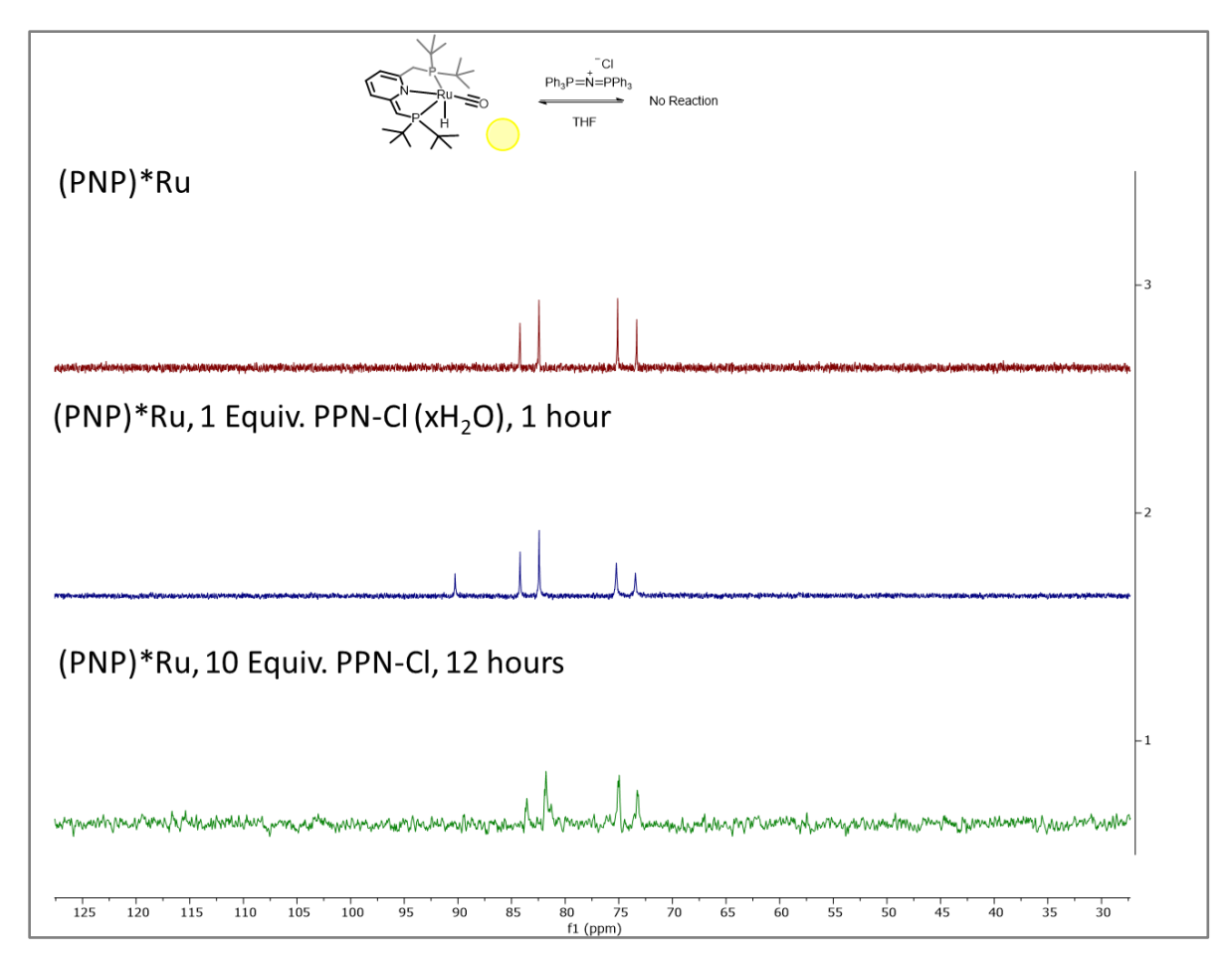


Figure S41: ³¹P NMR spectra (293 K, THF) of the reaction of **(*PNN)Ru** with [(Ph₃P)₂N][Cl] **(top):** 23 mM **(*PNP)Ru. (middle):** Spectrum obtained after treatment of 23 mM **(*PNN)Ru** with 1 equiv [(Ph₃P)₂N][Cl] for 1 h. The salt was not dried, and shows formation of a new species. The singlet suggests a 6-coordinate species of the type **(PNN)Ru-X**. The chemical shift does not correspond to that of **(PNN)Ru-CI** or **(PNN)Ru-OH. (bottom):** Spectrum obtained after treatment of 19 mM **(*PNN)Ru** with 10 equiv *dried* [(Ph₃P)₂N][Cl] for 12 h, indicating no reaction. The salt was dried by heating under vacuum at 100 °C for 12 hours. The spectrum was obtained after filtering through celite to remove the insoluble [(Ph₃P)₂N][Cl].

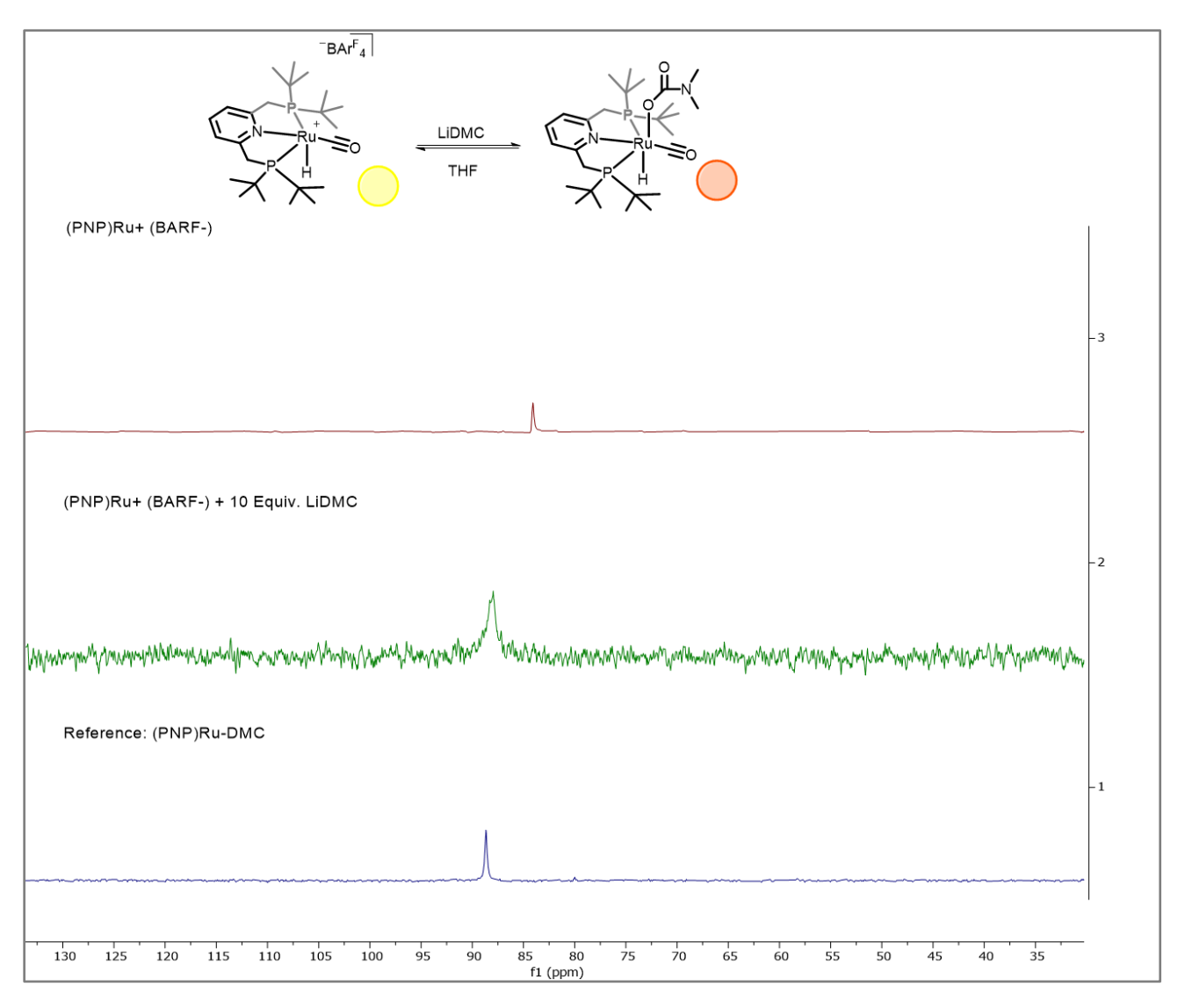


Figure S42: ^{31}P NMR (293K, THF) of (top): 4 mM (PNP)Ru+(BArF-); (middle): upon addition of 10 equiv (Li)(DMC); (bottom): (PNP)Ru-DMC.

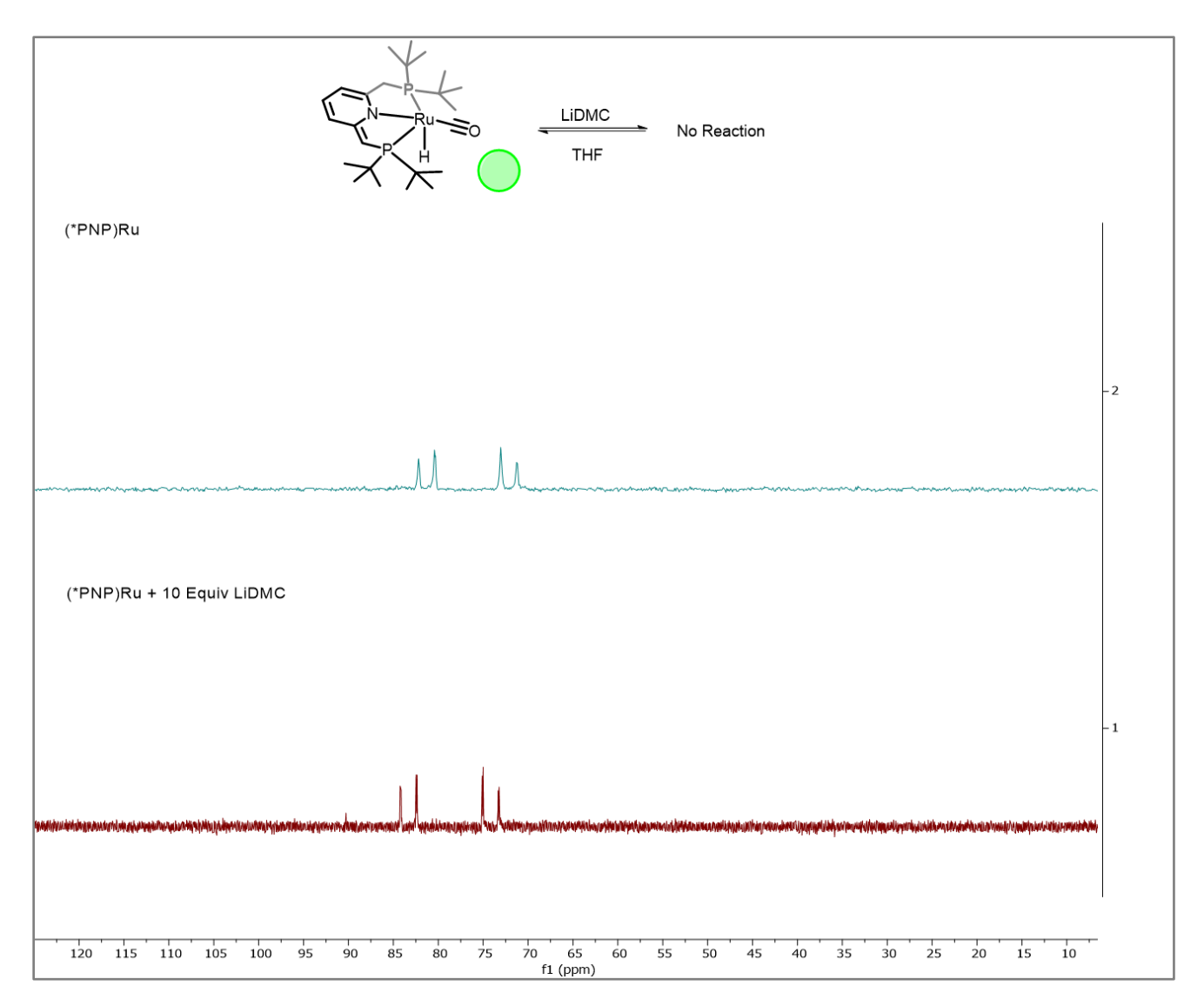


Figure S43: ^{31}P NMR (293K, THF) of **(top):** 8 mM **(*PNP)Ru***; **(bottom):** upon addition of 10 equiv (Li)(DMC).

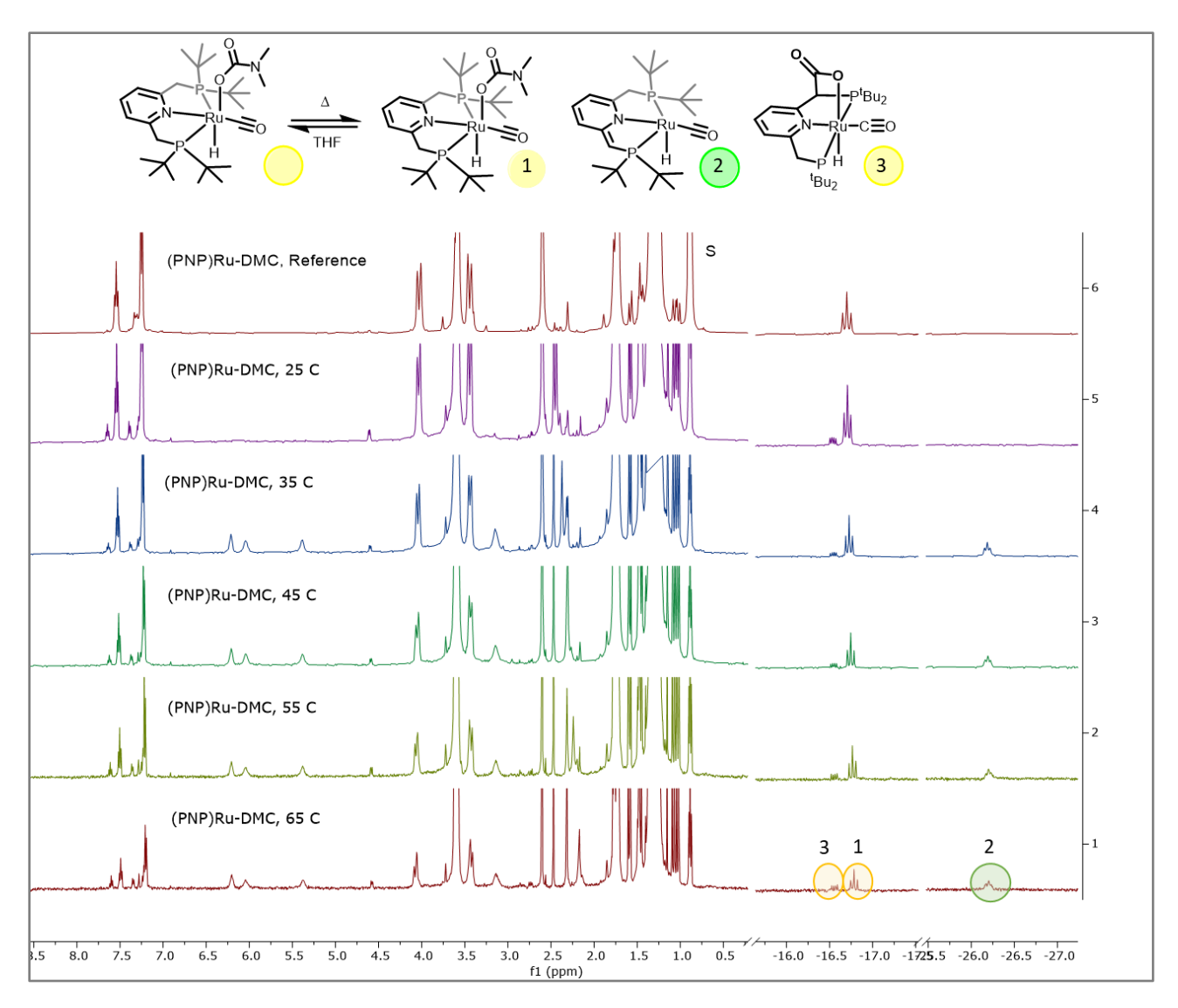


Figure S44: Stacked ¹H NMR spectra (500 MHz, THF-*d*₈) of 80 mM **(PNP)Ru-DMC** recorded at 65 (bottom), 55, 45, 35, and 25 °C (purple). The top spectrum is a reference prior to heating. Species "2" is **(*PNP)Ru**, and "3" is **(PNP)Ru-CO**₂. Solvent impurities 'S' are from pentanes. At elevated temperatures, the released DMC-H decomposes to give DMA and CO₂, which then coordinates the Ru.

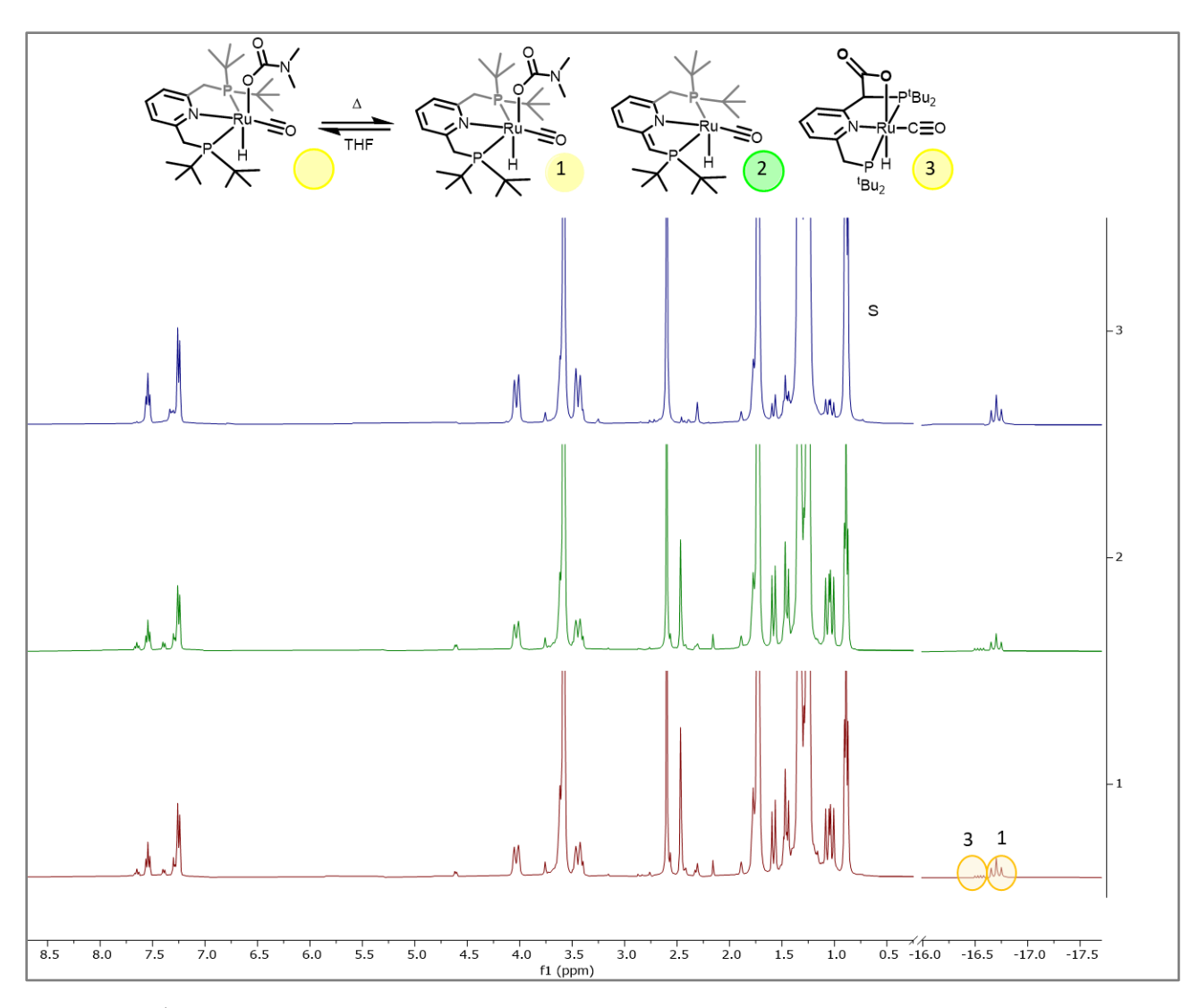


Figure S45: ¹H NMR spectra (400 MHz, 293 K, THF-*d*₈) of **(top):** 9.2 mM **(PNP)Ru-DMC**; **(middle):** same sample after heating to 65 °C for 2 h; **(bottom):** after heating to 65 °C for 48 h. Solvent impurities 'S' are from pentanes.

Section 7: References

- (1) Gnanaprakasam, B.; Zhang, J.; Milstein, D. Direct Synthesis of Imines from Alcohols and Amines with Liberation of H₂ Angew. Chem. Int. Ed. **2010**, 49, 1468.
- (2) Bauer, J. O.; Leitus, G.; Ben-David, Y.; Milstein, D. Direct Synthesis of Symmetrical Azines from Alcohols and Hydrazine Catalyzed by a Ruthenium Pincer Complex: Effect of Hydrogen Bonding *ACS Catal.* **2016**, *6*, 8415.
- (3) Vogt, M.; Gargir, M.; Iron, M. A.; Diskin-Posner, Y.; Ben-David, Y.; Milstein, D. A New Mode of Activation of CO₂ by Metal–Ligand Cooperation with Reversible C-C and M-O Bond Formation at Ambient Temperature *Chem. Eur. J.* **2012**, *18*, 9194.
- (4) Anaby, A.; Butschke, B.; Ben-David, Y.; Shimon, L. J. W.; Leitus, G.; Feller, M.; Milstein, D. B–H Bond Cleavage via Metal–Ligand Cooperation by Dearomatized Ruthenium Pincer Complexes *Organometallics* **2014**, *33*, 3716.
- (5) Ahmad, N.; Levison, J. J.; Robinson, S. D.; Uttley, M. F.; Wonchoba, E. R.; Parshall, G. W. In *Inorg. Synth.* 1974; Vol. 15, p 45.
- (6) Swarnakar, A. K.; McDonald, S. M.; Deutsch, K. C.; Choi, P.; Ferguson, M. J.; McDonald, R.; Rivard, E. Application of the Donor–Acceptor Concept to Intercept Low Oxidation State Group 14 Element Hydrides using a Wittig Reagent as a Lewis Base *Inorg. Chem.* **2014**, *53*, 8662.
- (7) Rodima, T.; Maemets, V.; Koppel, I. Synthesis of N-aryl-substituted iminophosphoranes and NMR spectroscopic investigation of their acid-base properties in acetonitrile *J. Chem. Soc., Perkin Trans.* 1 **2000**, 2637.
- (8) Armarego, W. L. F.; Chai, C. L. L. *Purification of Laboratory Chemicals*; 5 ed.; Butterworth-Heinmann: London, 2002.
- (9) Krause, L.; Herbst-Irmer, R.; Sheldrick, G. M.; Stalke, D. *J. Appl. Cryst.* **2015**, *48*, 3.
- (10) Sheldrick, G. M. SHELXT Integrated space-group and crystal-structure determination *Acta Cryst. A* **2015**, *71*, 3.
- (11) Sheldrick, G. M. Crystal structure refinement with SHELXL *Acta Cryst. C* **2015**, 71, 3.
- (12) Spek, A. L. Single-crystal structure validation with the program PLATON *J. Appl. Cryst.* **2003**, *36*, 7-13.
- (13) Filonenko, G. A.; Conley, M. P.; Cop ret, C.; Lutz, M.; Hensen, E. J. M.; Pidko, E. A. The impact of Metal–Ligand Cooperation in Hydrogenation of Carbon Dioxide Catalyzed by Ruthenium PNP Pincer *ACS Catal.* **2013**, *3*, 2522.
- (14) Saouma, C. T.; Kaminsky, W.; Mayer, J. M. Protonation and Concerted Proton–Electron Transfer Reactivity of a Bis-Benzimidazolate Ligated [2Fe–2S] Model for Rieske Clusters *J. Am. Chem. Soc.* **2012**, *134*, 7293.
- (15) Kaljurand, I.; Saame, J.; Rodima, T.; Koppel, I.; Koppel, I. A.; Kögel, J. F.; Sundermeyer, J.; Köhn, U.; Coles, M. P.; Leito, I. Experimental Basicities of Phosphazene, Guanidinophosphazene, and Proton Sponge Superbases in the Gas Phase and Solution *J. Phys. Chem. A* **2016**, *120*, 2591.
- (16) Vazdar, K.; Kunetskiy, R.; Saame, J.; Kaupmees, K.; Leito, I.; Jahn, U. Very Strong Organosuperbases Formed by Combining Imidazole and Guanidine Bases: Synthesis, Structure, and Basicity *Angew. Chem. Int. Ed.* **2014**, *53*, 1435.

- (17) Saame, J.; Rodima, T.; Tshepelevitsh, S.; Kütt, A.; Kaljurand, I.; Haljasorg, T.; Koppel, I. A.; Leito, I. Experimental Basicities of Superbasic Phosphonium Ylides and Phosphazenes *J. Org. Chem.* **2016**, *81*, 7349.
- (18) Gennaro, A.; Isse, A. A.; Vianello, E. Solubility and electrochemical determination of CO₂ in some dipolar aprotic solvents *J. Electroanal. Chem. Interfac.* **1990**, *289*, 203.
- (19) Brunner, E. Solubility of hydrogen in 10 organic solvents at 298.15, 323.15, and 373.15 K *J. Chem. Eng. Data* **1985**, *30*, 269.
- (20) Rezayee, N. M.; Huff, C. A.; Sanford, M. S. Tandem Amine and Ruthenium-Catalyzed Hydrogenation of CO₂ to Methanol *J. Am. Chem. Soc.* **2015**, *137*, 1028.